nanoenergy advances

MDPI

Review

Borocarbonitrides for Decarbonization: From CO_2 Utilization to Renewable Fuel Synthesis

Carlos A. Castilla-Martinez [1,*], Perla C. Meléndez-González [2,3] and Umit B. Demirci [1]

[1] Institut Européen des Membranes, IEM–UMR 5635, Univ Montpellier, CNRS, ENCSCM, 34095 Montpellier, France; umit.demirci@umontpellier.fr
[2] Department Interface Design, Helmholtz-Zentrum Berlin für Materialien und Energie GmbH (HZB), Albert-Einstein-Straße 15, 12489 Berlin, Germany; perla.melendez_gonzalez@helmholtz-berlin.de
[3] Tecnológico Nacional de México, Instituto Tecnológico Del Valle de Etla, Abasolo S/N, Barrio Del Agua Buena, Santiago Suchilquitongo, Oaxaca 68230, Mexico
* Correspondence: carlos.castilla-martinez@umontpellier.fr or ccastilla90@gmail.com

Abstract: Borocarbonitrides (BCNs), a new class of ternary materials combining boron, carbon, and nitrogen atoms, have emerged as promising candidates in decarbonization technologies due to their unique physicochemical properties. BCNs offer an adjustable atom composition and electronic structure, thermal stability, and potentially a large specific surface area, which are attractive features for efficient interactions with carbon dioxide. These make BCNs suitable for carbon dioxide capture, storage, and catalytic conversion applications. Furthermore, BCNs have the potential to (electro)catalyze the synthesis of green fuels, such as hydrogen, as well as that of other hydrogen carriers such as ammonia. With this review, we examine the recent advances in BCN synthesis methods, characterization, and functional applications while focusing on their role in the decarbonization technologies mentioned above. We aim to highlight the potential of BCNs to drive innovation in sustainable carbon management. Additionally, in the last section of this paper, we discuss the challenges and prospects of BCNs in decarbonization and beyond.

Keywords: borocarbonitride; decarbonization; boron; carbon; nitride; carbon dioxide; hydrogen; ammonia; catalysis; gas adsorption

Academic Editors: Ya Yang, Joao Ventura, Elby Titus and Carmen M. Rangel

Received: 16 January 2025
Revised: 5 March 2025
Accepted: 20 March 2025
Published: 9 April 2025

Citation: Castilla-Martinez, C.A.; Meléndez-González, P.C.; Demirci, U.B. Borocarbonitrides for Decarbonization: From CO_2 Utilization to Renewable Fuel Synthesis. *Nanoenergy Adv.* **2025**, *5*, 6. https://doi.org/10.3390/nanoenergyadv5020006

1. Introduction

Economic development and societal well-being depend significantly on energy. However, the methods we use to produce, convert, and consume energy are the largest sources of greenhouse gas emissions, particularly carbon dioxide (CO_2), making them primary contributors to climate change. The electric power and transportation sectors alone account for more than 50% of greenhouse gas emissions released into the atmosphere [1].

The primary aim of decarbonization technologies is to reduce greenhouse gas emissions by 80–100% by 2050 [2]. These technologies encompass a broad range of approaches, including CO_2 capture, transformation, and storage, as well as alternative energy sources that do not emit CO_2 during use, such as hydrogen. Hydrogen (H_2) is a zero-emission fuel and energy carrier with considerable potential to contribute to decarbonization [3]. Hydrogen can be used in its pure form or within other carriers, such as ammonia (NH_3) or liquid organic compounds [4,5]. However, current H_2 production relies heavily on fossil fuels, creating a feedback loop between CO_2 emissions and energy demand. To break this cycle, it is essential to develop greener methods to produce H_2 and its carriers, such as electrolysis, photolysis, or the use of biomass [6]. A wide range of materials has been

investigated for CO_2 capture and conversion and for H_2 production, including zeolites, carbon-based materials, metal-organic frameworks (MOFs), and both metal-based and metal-free semiconductors and catalysts [7,8]. Among these, borocarbonitrides (BCNs) have recently garnered attention for their potential applications in decarbonization and related fields.

Figure 1 shows the ternary phase diagram for boron, carbon, and nitrogen, with each triangle vertex representing a single element [9]. The carbon vertex includes various allotropes, such as graphene and fullerene. At the boron vertex, materials like boron clusters and borophene are represented. The nitrogen vertex features nitrogen-based structures, such as cubic gauche nitrogen, which has been experimentally investigated under extreme conditions (over 2273 °C and 110 GPa) [10]. Binary materials—such as boron carbide, carbon nitride, and boron nitride—can be found along the edges of the triangle. BCNs are located at the center of the triangle and have a general stoichiometry of $B_xC_yN_z$.

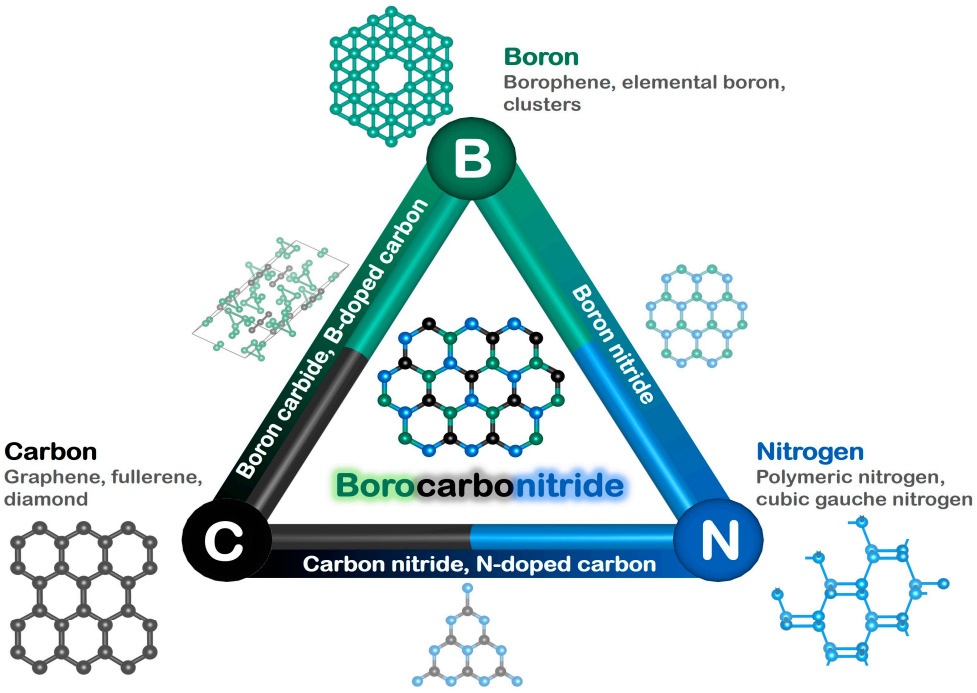

Figure 1. Ternary boron–carbon–nitrogen diagram. Adapted from Ref. [9].

Graphene, the first two-dimensional (2D) material reported in the literature, consists of a single layer of sp^2-hybridized carbon atoms arranged hexagonally and bonded covalently (Figure 2a) [11]. Boron nitride (BN) is composed of a network of alternating boron and nitrogen atoms. Four types of BN are known: one is amorphous BN, and three are crystalline. The crystalline forms are as follows: cubic BN, which resembles diamond; wurtzite BN, a metastable phase that forms under high pressure; and hexagonal BN (h-BN) [12]. h-BN consists of a layered structure reminiscent of graphene (Figure 2b), whose layers are composed of boron and nitrogen atoms linked by strong, polarized covalent bonds and held together by van der Waals forces.

Borocarbonitrides are characterized by a hexagonal network of covalent bonds, including C–C, C–N, C–B, and B–N. While some authors have stated that there are no B–B or N–N bonds in these structures, experimental studies have detected the presence of homopolar B–B bonds [13]. Even if the term "borocarbonitride" is often used broadly in the literature, a clear distinction should be made: phase-separated BCNs, which consist of distinct, segregated regions of graphene and boron nitride (Figure 2c), and homogeneous BCNs, where the B, C, and N atoms are uniformly mixed (Figure 2d). Sometimes, the

borocarbonitride term has been used for B-doped graphitic carbon nitride, C-doped h-BN, or B- and N-doped carbon. For the purpose of this study, we have considered all of these materials for the selected applications. However, we suggest that a clear classification should be considered, which will be further developed in Section 4.

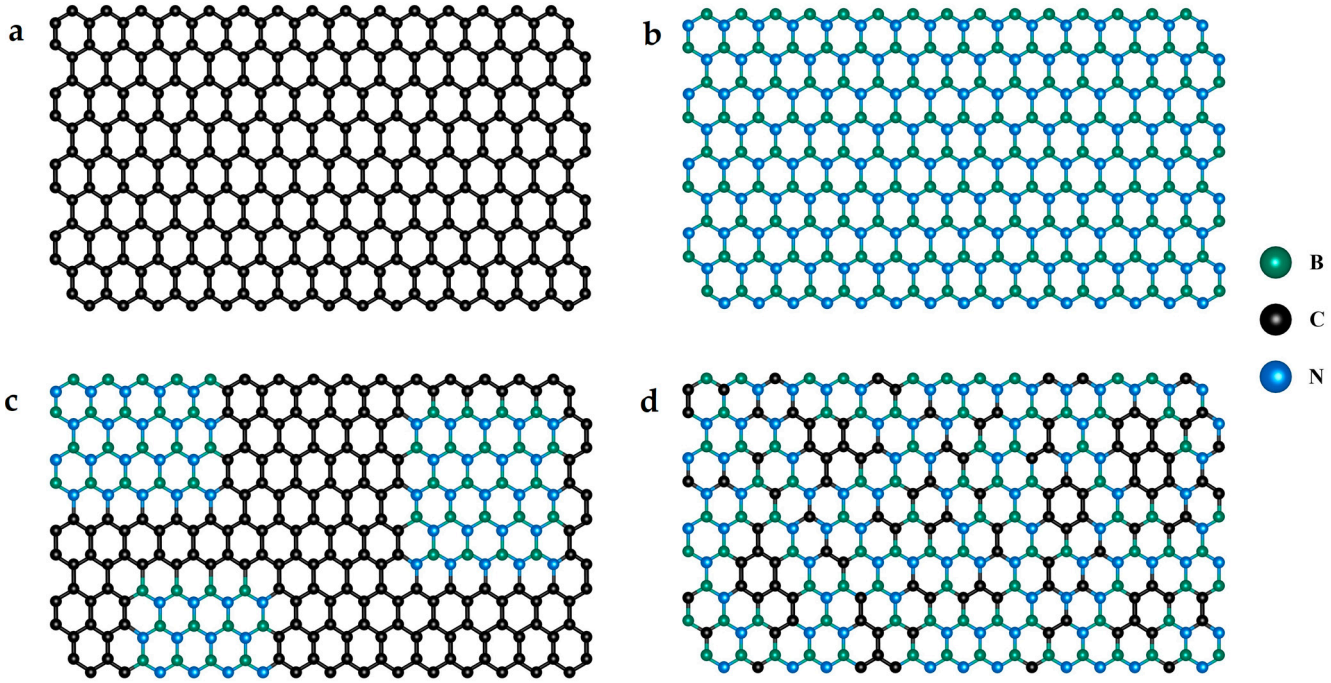

Figure 2. Schematic illustration of (**a**) graphene; (**b**) hexagonal boron nitride; (**c**) phase-separated borocarbonitride; and (**d**) homogeneous borocarbonitride.

BCNs have properties that fall between those of graphene and BN. For example, graphene is a conductor with zero bandgap, and BN is an insulator with a bandgap of about 6 eV [14]. The bandgap of BCNs can be tuned within this range, based on the carbon content in the structure, but it is not the only property that can be modified. Other properties of BCNs, such as optical, thermal, and chemical characteristics, can also be tuned by adjusting the content of carbon, boron, and nitrogen atoms within their structure. Although most BCNs reported (see Section 2.2.2) present an amorphous structure, theoretical calculations have predicted several crystal structures that are dynamically stable under ambient conditions [15–20]: hexagonal (and trigonal), cubic, orthorhombic, and monoclinic. Experimentally, a cubic phase of BC_2N was obtained under extreme conditions (2150 °C and 7.7 GPa) [21].

Due to their unique tunable physicochemical properties, experimental and theoretical studies have investigated the properties of BCNs for different applications, including electrochemical energy storage [22–24], sensors [25], the detection/adsorption of gas molecules [26–32], catalysis [33–35], optoelectronic devices [36–39], hydrogen peroxide H_2O_2 production [40–42], the selective oxidation of hydrogen sulfide [43], Knoevenagel condensation reactions [44–46], the Groebke–Blackburn–Bienayme reaction [47], wastewater treatment [48–58], super-wear-resistant coatings [59], thermal interface devices [60], solar cells [61], low-dissipation high-speed nanoelectronics [62], high-temperature lubricants [63–65], and as sorbents for paraben compounds [66].

In particular, and this is the focus of this review article, BCNs exhibit promising features for decarbonization technologies, such as gas adsorption and serving as metal-free catalysts in different reactions for both CO_2 utilization and renewable fuel synthesis. Accordingly, we aim to assess recent advances in the performance of BCNs in decarbonization

alternatives, with particular emphasis on CO_2 conversion processes, and in the synthesis of value-added fuels, described in Section 3 (including gas adsorption, metal-free catalysis, photocatalysis, and electrocatalysis). We also analyze some innovative approaches for the synthesis and fabrication of BCN materials, highlighting the use of different chemical precursors, and offer a short, comprehensible characterization guide for BCNs with the most used techniques, as reported in the related literature. Finally, we explore future perspectives and challenges for advancing BCN applications.

2. Synthesis and Characterization of Borocarbonitrides

2.1. Synthesis

Various methods have been explored for synthesizing BCNs, each employing distinct precursors. The syntheses can be categorized based on the types of precursors selected to provide the boron, carbon, and nitrogen elements. Thus, this section presents a classification of the main types of precursors used in BCN synthesis instead of classifying the synthesis approach by method. The selection of precursors plays an important role in determining the properties of BCNs. For instance, the elemental composition of the precursors—specifically the proportions of boron, carbon, and nitrogen—influences the properties of the final BCN. Additionally, certain precursors can result in distinct morphological variations, further impacting the material's characteristics. These will be discussed in the following paragraphs.

h-BN and graphite have been used as precursors and targets for fabricating BCN thin films using physical vapor deposition (PVD) techniques, such as radio frequency magnetron sputtering or a combination of vacuum arc deposition and magnetron sputtering [59,67]. Otherwise, these precursors can react at high temperatures (annealed between 600 and 1000 °C) to produce oxygen-free BCN nanosheets with varying carbon content [39]. Boron carbide (B_4C) was also explored in one study as a potential carbon source for BCN thin-film growth by PVD, and it allowed for the tuning of the carbon content in the BCN films produced [68].

Combining three precursors, each one for one element (boron, carbon, and nitrogen), is one of the most used methods for producing BCN. The most commonly reported carbon sources include activated carbon [69], dextrose $C_6H_{12}O_6$ [70,71], and glucose [72]. Coconut shells or orange peel extracts have been used as precursors for producing activated carbon, before its use as a source of BCN [73,74]. To provide the boron and nitrogen atoms, boric acid ($B(OH)_3$) and urea ($(NH_2)_2CO$) are widely used. BCN production typically involves mixing the three precursors (either in the solid state using a mortar or in water assisted by sonication), followed by heating the homogeneous mixture at temperatures of 900–1350 °C under a nitrogen (N_2) atmosphere or NH_3 for 1 to 10 h. For example, an exfoliating process between h-BN and graphene followed by a heat treatment at 850 °C introduces carbon atoms into the BN lattice (carbon doping), leading to the formation of B–C, N–C, and C–C bonds, which confirms the successful production of BCN nanosheets [75]. BCN powders can be obtained by using exfoliated graphene, $B(OH)_3$, and $(NH_2)_2CO$ as the carbon, boron, and nitrogen precursors, respectively [76]. A BCN powder synthesized using this method was subsequently used to deposit thin films onto sapphire substrates kept at 800 °C, using pulsed laser deposition [77].

Additional precursors can be added to the $B(OH)_3$, $(NH_2)_2CO$, and carbon source mixture, for example, melamine ($C_3H_6N_6$) and sodium hydroxide NaOH (2–3 wt%) [78]. While melamine serves as an additional source of carbon and nitrogen, NaOH has a dual role, as it catalyzes the decomposition of the precursors to allow the homogeneous dispersion of carbon, and it acts as a crystallization promoter. Instead of using three precursors, melamine can be used solely with the boron source $B(OH)_3$. BCN thin films can

then be prepared by using one equivalent of melamine and two equivalents of $B(OH)_3$ upon heating at 300 °C for 30 min and then 550 °C for 4 h under a nitrogen atmosphere; it is worth mentioning that mixing the two precursors in water at 100 °C, in a preliminary step, results in a cocrystal—where all of the elements are thus homogeneously distributed—which has a monoclinic structure with a *P*21/*c* space group [79].

In many cases, the mixture of melamine and boric acid as precursors is used to obtain boron-doped graphitic carbon nitride (g-C_3N_4) [80–82]. Alternatively, a melamine–boric acid adduct has been proposed as a precursor, and its thermal decomposition products at 550 °C can be used to fabricate BCN thin films by chemical vapor deposition (CVD) [83]. The as-produced BCN films showed increased crystallinity and stability to oxidation with the increase in boron content in the films. Moreover, a melamine phosphate borate adduct was prepared by mixing melamine, boric acid, and phosphoric acid, which were pyrolyzed together with glucose and urea, obtaining a BCN with large specific surface area (SSA) [84].

An alternative source of carbon and nitrogen is glycine, NH_2CH_2COOH; when mixed with $B(OH)_3$, it produces BCN nanotubes upon heating at 900–1000 °C in a nitrogen atmosphere, with a yield of 75% [85]. Other nitrogen-based compounds have been tested as sources of this element, such as casein, aminoguanidine, dicyandiamide, ammonium chloride, or ammonia borane (AB, NH_3BH_3) [86,87]. Ammonia borane is also a boron source. One study used the gaseous products released by AB at 160 °C to further make them react with melamine to produce BCN thin films on a sapphire substrate at 650 °C [88]. AB has also been used together with methane (CH_4) and nitrogen to produce BCN nanosheets using radio frequency Inductively Coupled Plasma [89].

AB is a well-known precursor of boron nitride and the simplest representative of amineboranes, a family of compounds composed of boron, nitrogen, and carbon [90,91]. Using a single amineborane precursor is a promising approach to obtain BCNs. Methylamine borane ($CH_3NH_2BH_3$) is a typical example, containing one atom of each element (excluding hydrogen). Its melting point of 55 °C and decomposition temperature above 100 °C make it a suitable single precursor of BCN thin-film production by CVD and microwave-assisted plasma-enhanced chemical vapor deposition [92,93].

An alternative to methylamine borane with the same B:C:N atomic ratio is ethane 1,2-diamine borane ($BH_3NH_2CH_2CH_2NH_2BH_3$), containing two atoms of each element [94–96]. The synthesis of BCN thin films on a copper foil has been successfully demonstrated from dimethylamine borane ($(CH_3)_2NH_2BH_3$) [97] and trimethylamine borane ($(CH_3)_3NH_2BH_3$) [98]. A promising amine borane with a cyclic structure is bis-BN cyclohexane ($C_2N_2B_2H_6$). BCN films grown by CVD using this precursor showed covalent $B_2C_2N_2$ rings, indicating that the precursor molecule remained intact on the substrate surface [99].

This paves the way for synthesizing structure-controlled BCN materials using specifically designed cyclic precursors. Alternatively, a single organic-inorganic precursor was produced by mixing boric acid and ethylenediamine in water, which was further treated under an ammonia atmosphere at 1200 °C to yield a homogeneous BCN (Figure 3a) [100].

Also interesting is the utilization of alternative precursors such as an ionic liquid, a MOF, and elemental boron. Ionic liquids can be used as a single precursor for BCN production. One example is 1-ethyl-3-methylimidazolium-tetracyanoborate $[CH_3(N_2C_3H_3)C_2H_5^+][B(CN)_4^-]$, which produces a BCN with the composition $BC_{3.1}N_{0.96}$ when heated at 1400 °C under a nitrogen atmosphere [101]. Ionic liquids can also be employed to incorporate boron atoms into a carbon structure: 1-butyl-3-methylimidazolium tetrafluoroborate ($BmimBF_4$) was mixed with melamine in water, and through further pyrolysis at 500 °C, B-doped g-C_3N_4 was obtained [102]. A boron-based MOF, $[Zn_4(1,4\text{-ndc})_3(bim)_2]\cdot 2H_2O$ (with bim = tetrakis(1-imidazolyl)borate, and 1,4-ndc = napthalenedi-

carboxylate), was used as a single precursor to obtain a BCN after pyrolysis at 450 °C under a nitrogen atmosphere [103]. Elemental boron has also been used as a target material, combined with a mixture of argon, N_2, and CH_4 gases. BCN films were grown on WC-Co substrates using a sputtering–PBII hybrid system, a combination of sputtering and pulsed laser deposition [65].

Original synthesis approaches have been explored to obtain BCNs presenting unique morphologies. Two-dimensional structures can be obtained through the molten salt method, which involves adding an ionic salt (sodium or potassium chloride NaCl/KCl or a mixture of both) to the BCN precursor mixture, which is then annealed under an inert atmosphere [104]. This has been proved successful, as ultrathin BCN nanosheets have been obtained through this approach [72,105]. Two-dimensional BCN nanosheets were also obtained by pyrolyzing a precursor mixture made of formamide CH_3NO and boric acid [106]. A highly mesoporous BCN was obtained through the infiltration of a mixture of AB and sucrose into a structured template (silica SBA-15) and its further pyrolysis and template removal (Figure 3b) [107]. A mixture of glucose, boric acid, and melamine was freeze-dried at −53 °C and 0.4 mbar and further pyrolyzed at 1000 °C for 2 h under a nitrogen atmosphere to obtain BCN aerogels [108].

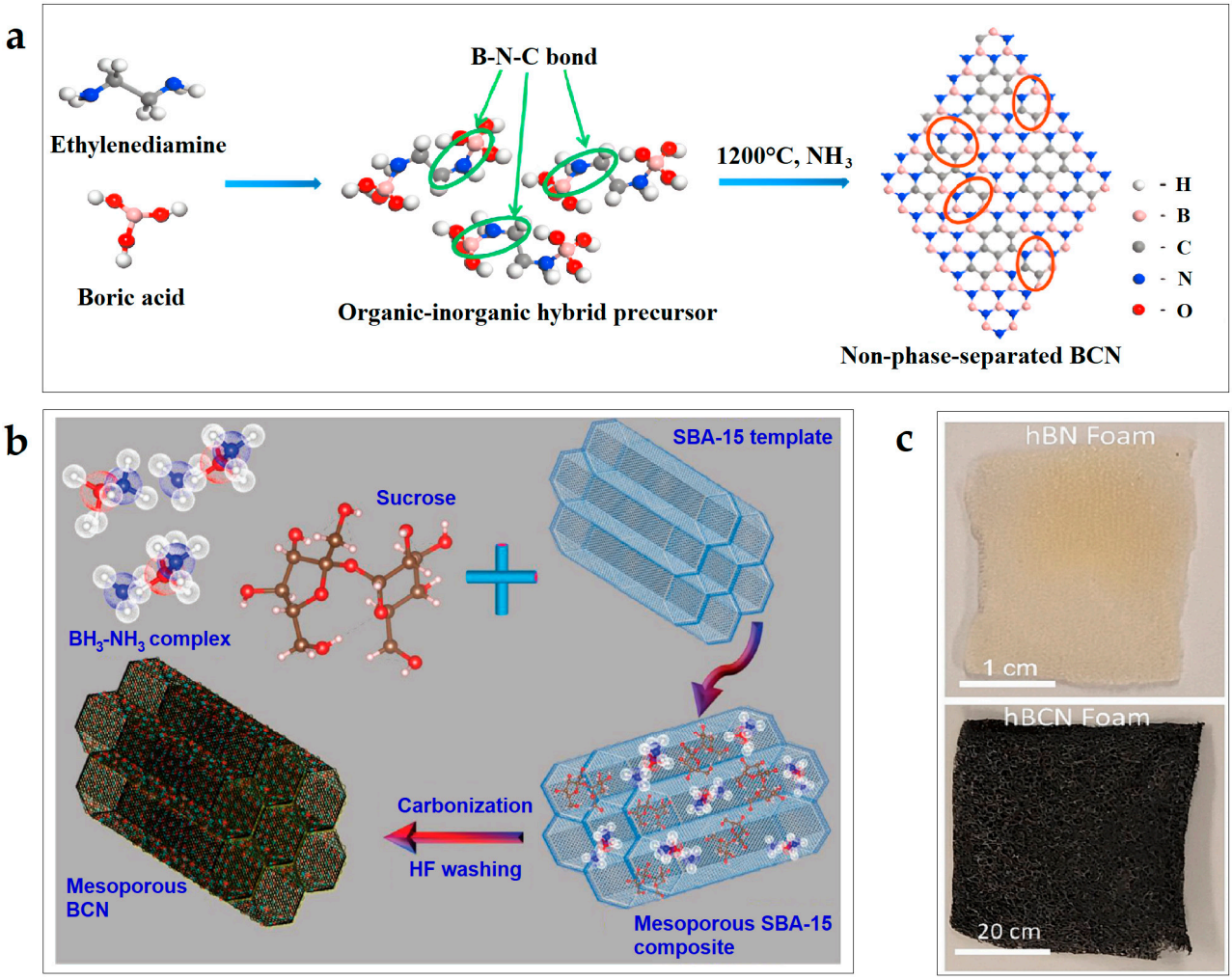

Figure 3. (**a**) Schematic representation of the synthesis of a homogeneous BCN through the formation of an organic-inorganic hybrid precursor (reprinted with permission from Ref. [100]. Copyright 2022, Elsevier). (**b**) schematic representation of the synthesis of a mesoporous BCN obtained by a hard-template approach [107] (**c**) comparison of a foam made of BN and BCN (reprinted with permission from Ref. [109]. Copyright 2024, Elsevier).

Single aminoborane precursors were used to produce porous BCN foams (Figure 3c) by CVD using nickel foam as a hard template [109]. A BCN with a coral-like morphology was obtained through the pyrolysis of a boron-imidazolate MOF (Figure 4a) [103]. A BCN with a rice-grain morphology was obtained through the pyrolysis of a boric acid and hexamine mixture (Figure 4b) [110]. Nanostructured BCN spheres were produced by a reverse micelle approach, in a system using AB and hexadecylamineborane as precursors, and acetonitrile and cyclohexane were used as the solvent and counter solvent, respectively. The reverse micelles were further polymerized and pyrolyzed to obtain BCN nanospheres (Figure 4c) [111]. A BCN obtained by using $NaBH_4$, NaN_3, and alcohol resulted in nanoplates with a triangle shape (Figure 4d) [112]. From a composite obtained by confining AB molecules inside the porosity of a ZIF-8 MOF, which was further pyrolyzed at 800 °C under a nitrogen atmosphere, a BCN keeping the hexagonal crystal morphology of the parent ZIF-8 was produced (Figure 4e) [113]. BCNs with an octahedral morphology were obtained using a boron-imidazolate framework (BIF-20) as a precursor (Figure 4f) [114].

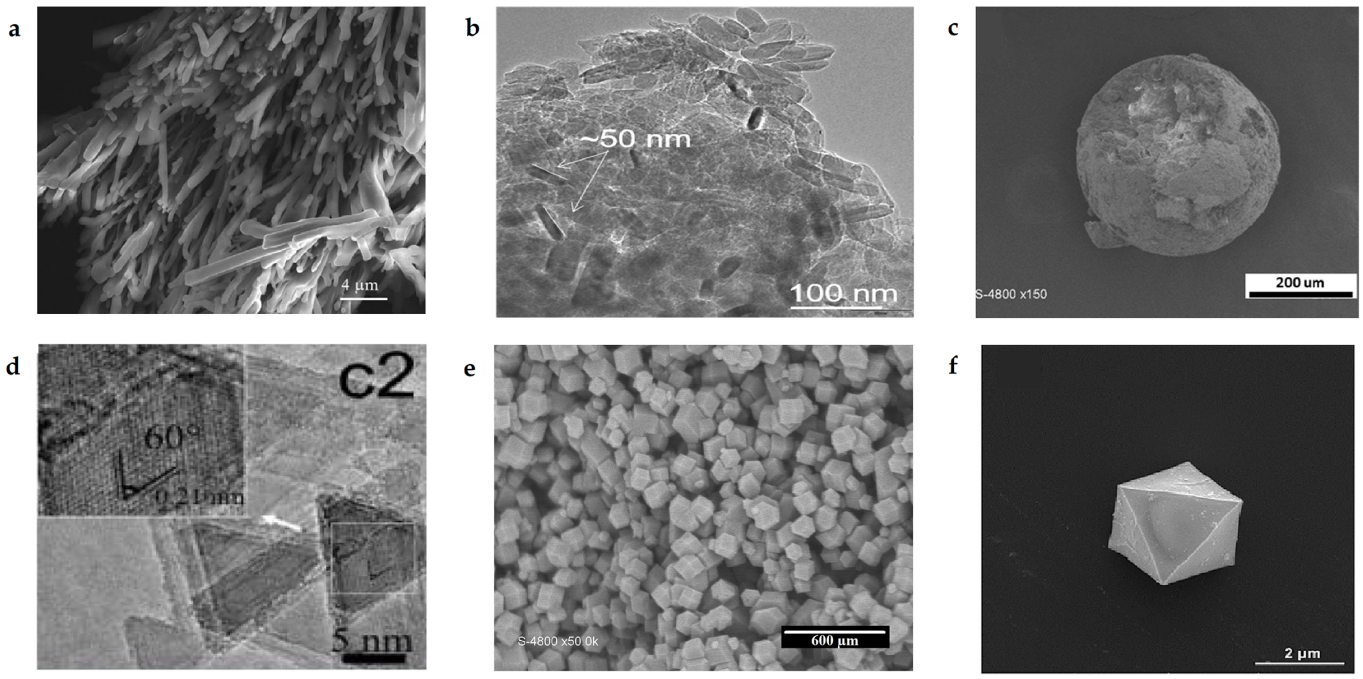

Figure 4. Borocarbonitrides with (**a**) coral-like (reprinted with permission from Ref. [103]. Copyright 2013, Wiley); (**b**) rice-grain (reprinted with permission from Ref. [110]. Copyright 2018, American Chemical Society); (**c**) spherical (reprinted with permission from Ref. [111]. Copyright 2023, MDPI); (**d**) triangular (reprinted with permission from Ref. [112]. Copyright 2017, Elsevier); (**e**) hexagonal crystal [113]; and (**f**) octahedral morphology (reprinted with permission from Ref. [114]. Copyright 2023, Elsevier).

This section has reviewed the use of different precursors to synthesize BCNs through various approaches. A wide variety of precursors have been explored, such as melamine, boric acid, MOFs, and ionic liquids. Notably, single-source precursors like amine boranes offer a promising route for simplified BCN synthesis. Additionally, precursor choice can influence BCN morphology, with techniques like molten salt methods, reverse micelles, or hard templating enabling the creation of 2D structures and nano- and porous structures. This diverse range of choices emphasizes the potential for tuning BCN materials to meet specific applications.

2.2. Characterization

2.2.1. Elemental Analysis

The elemental composition of BCNs can be determined using Energy-Dispersive X-ray (EDX) spectroscopy. For BCNs produced from h-BN and graphite at temperatures ranging from 600 to 1000 °C, EDX spectra have revealed that the carbon content in the BCNs increases as the heating temperature increases [39]. For example, the BCN obtained at 800 °C contained approximately 23% of carbon, while the amount of carbon in the BCN produced at 1000 °C was approximately 45%. In a BCN whose crystallinity was promoted by NaOH, the EDX spectrum did not show the presence of sodium, confirming that this element was not integrated in the BCN structure [78]. EDX analysis is also a preliminary method for checking the presence or absence of oxygen, which may be due to the oxidation of the BCN [39,70]. The elemental composition of BCNs can also be determined by Inductively Coupled Plasma Mass Spectrometry (ICP-MS) or Optical Emission Spectroscopy (ICP-OES) [96,115] and by CHN elemental analysis.

X-ray Photoelectron Spectroscopy (XPS) is a relevant surface technique for analyzing BCNs, especially those presented in the form of thin films. For example, a BCN thin film produced from ethane 1,2-diamine borane at 1000 °C was found to have a carbon-rich composition with a B:C:N atomic ratio of 0.11:0.76:0.13 [95]. In a BCN produced by the dual-target sputtering of B_4C and BN, 2–6% of oxygen was detected. The oxygen was bonded to all of the B, C, and N atoms in the material [68].

Other characterization techniques include Electron Energy Loss Spectroscopy (EELS) and Thermogravimetric Analysis (TGA). EELS allows for the identification of elements through the observation of their spectral bands: boron (B) K-edges at approximately 194 eV, carbon (C) K-edges at approximately 286 eV, nitrogen (N) K-edges at approximately 400 eV, and oxygen (O) K-edges at approximately 535 eV [83]. TGA performed in an oxygen atmosphere allows for the quantification of carbon content (based on the weight loss associated with the release of carbon dioxide) and provides an insight into the material's composition, such as $(BN)_{0.7}C_{0.3}$, which was further confirmed by XPS and EDX analyses [69].

2.2.2. Structural Analyses

The X-ray Diffraction (XRD) pattern of BCN typically shows two broad peaks (Figure 5a). The first peak appears at 24°–26° and is assigned to the (002) reflection plane, which is typical of the interlayer spacing in graphite-like domains [116]. For example, the d-spacing calculated for the (002) peak of a BCN produced from a mixture of dextrose, boric acid, and urea was found to be 0.339 nm, which is slightly higher than the 0.334 nm for h-BN, which suggests the successful incorporation of carbon atoms into the BN structure [71]. Indeed, the broadening and shift of the (002) peak to slightly lower angles, compared to the peak for BN, indicate that carbon atoms have been introduced into the boron nitride lattice, resulting in a BCN [75]. A similar shift is observed with a higher carbon content in BCNs due to an increase in structural defects [73]. The second diffraction peak is centered at 42°–43° and is assigned to the (100) reflection plane. It is characteristic of the in-plane lattice parameter of the six-membered ring [117].

Disordered nanosized domains and crystallite sizes of 9–10 nm have been reported accordingly [69–71]. Additional diffraction peaks at higher 2θ angles, such as the (101), (004), and (110) reflection planes, can be observed for a NaOH-promoted highly crystallized BCN [78]. Similar observations were reported with Wide-Angle X-ray Scattering analysis, revealing the (002) and (100) reflection planes, as well as the (110) planes, whose presence indicates high conjugation on the analyzed BCN [101]. Concerning the (002) reflection plane, a broadening and shifting to lower angles indicated a larger interlayer distance (0.364 nm) than that of both h-BN (0.333 nm) and graphite (0.335 nm).

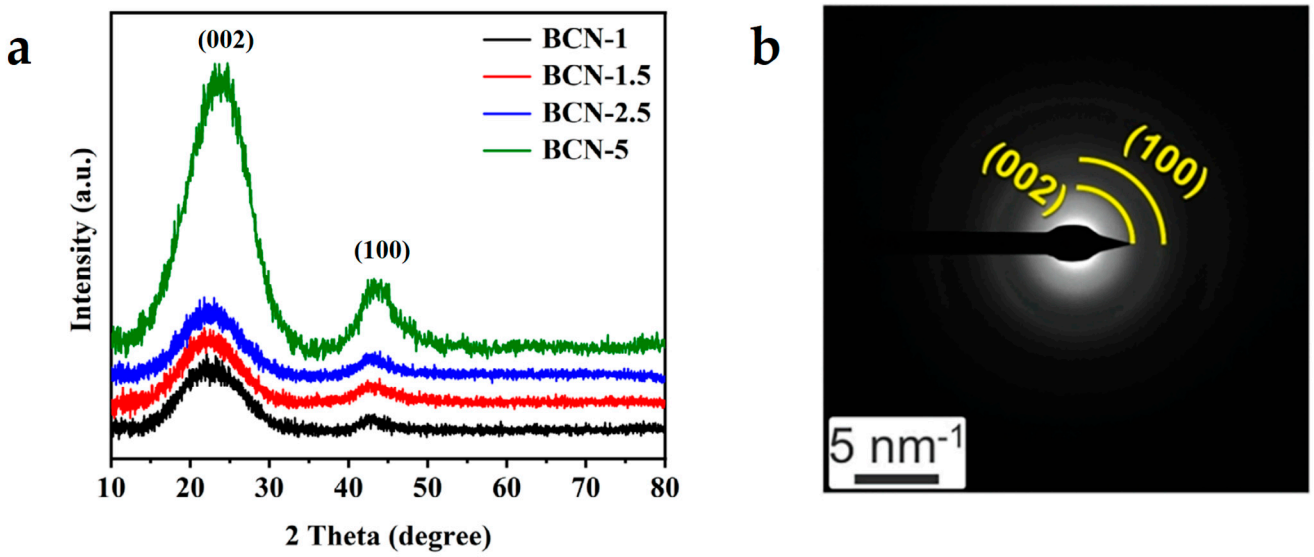

Figure 5. (**a**) Typical XRD (reprinted with permission from Ref. [73]. Copyright 2022, Elsevier); and (**b**) SAED patterns of BCN materials displaying the (002) and (100) reflection planes (reprinted with permission from Ref. [108]. Copyright 2021, Wiley).

High-Resolution (HR) Transmission Electron Microscopy (TEM) images and Selected-Area Electron Diffraction (SAED) patterns can also be used to assess the amorphous state or the low or high crystallinity of a BCN sample (Figure 5b). The hexagonal symmetry of a BCN is generally evidenced by SAED, with diffraction rings corresponding to the (002), (100), and (110) reflection planes, which have interplanar distances of 0.34, 0.22, and 0.12 nm, respectively [73,75,92,93]. In a few cases, the polycrystalline nature of a BCN has also been concluded based on the presence of continuous diffraction rings [92,93]. Additional diffraction rings due to the (101) and (004) reflection planes of a BCN were also reported [89].

The spectral bands observed on EELS spectra often corroborate the hexagonal structure. BCNs generally show sharp and intense π^* resonances due to sp^2 conjugation that is achieved through the sample [69,79,89,92,93].

2.2.3. Spectroscopic Analyses

Almost all BCNs reported so far have been systematically analyzed using IR, Raman, and XP spectroscopies to confirm the formation of a BCN through the observation of C–B and C–N bonds, in addition to the C–C and B–N bonds that are characteristic of graphite and h-BN, respectively. In a few cases, Magic-Angle Spinning Nuclear Magnetic Resonance (MAS NMR) has been used to characterize BCN materials.

The IR spectrum of BCNs is generally scrutinized at two different ranges of wavenumbers. Between 2500 and 500 cm^{-1}, the vibration modes of the aforementioned bonds can be visualized: at approximately 760 cm^{-1}, the out-of-plane B–N–B; at 1380 cm^{-1}, the in-plane B–N; at 1600 and 1020 cm^{-1}, the sp^2 C–N bond; at 2170 cm^{-1}, C≡N; and at 661 and 1080 cm^{-1}, the sp^2 B–C bonds [118,119]. The second wavenumber range is between 3600 and 3000 cm^{-1} and is typical of vibrations due to N–H and O–H bonds. Their presence can be attributed to adsorbed water (H–O–H), the formation of borates (B–O–H bonds), and terminal bonds (e.g., for N–H) [80,103]. The presence of B–O–H bonds is generally corroborated by a vibration due to B–O at approximately 1440 cm^{-1} [59].

Raman spectroscopy is a useful technique to determine if the atoms of BCNs are well mixed (homogeneous BCNs) or if they are arranged in big, separate domains of graphene

and h-BN (phase-separated BCNs). Different studies suggest that these different types of BCNs present different Raman spectra.

On the one hand, the Raman spectrum of phase-separated BCNs shows the typical D and G bands of graphitic sp^2 materials, located at 1340–1360 cm^{-1} and 1570–1605 cm^{-1}, respectively [95,97] (Figure 6a). The D band is attributed to in-plane B–N vibrations [120], while the G band is suggested to arise from the E_{2g} band of graphene-like domains [121]. The spectrum shows additional bands at higher wavenumbers due to combination modes, such as the 2D band at 2710–2740 cm^{-1} and the D+G band at 2920–2950 cm^{-1}. Both bands are characteristic of sp^2 conjugation in graphitic materials like BCNs [93]. The D and G bands can be further analyzed in three ways. Compared to those of h-BN and graphite, they are generally broader. This broadening is explained by an increase in defect sites due to the incorporation of boron and nitrogen in the carbon network (or the incorporation of carbon in the BN network) [89]. In addition, both bands exhibit shifts in comparison with BN and graphite, suggesting the presence of different boron, carbon, and nitrogen bonds in the BCN structure [101]. This also indicates an increase in internal stresses induced by distortions in bond lengths and in defect sites and a decrease in the crystallinity of the material [89,93]. Finally, the intensity ratio of the D and G bands can be used to confirm an increase or decrease in defect sites. A higher D-to-G intensity ratio indicates a higher proportion of BN in BCN, corresponding to more defects and disorders [73,89]. On the other hand, absorption bands are absent in the Raman spectra of homogeneous separated BCNs (Figure 6b). This has been attributed to well-mixed boron, carbon, and nitrogen atoms in the hexagonal network, as this disrupts the symmetry of graphite and h-BN [122], which leads to the disappearance of the E_{2g} vibration and the G mode due to the in-plane atomic displacements [100,123]. This also means a lack of ordered graphene or h-BN domains with a specific size, which prevents their contribution to the Raman spectrum [124].

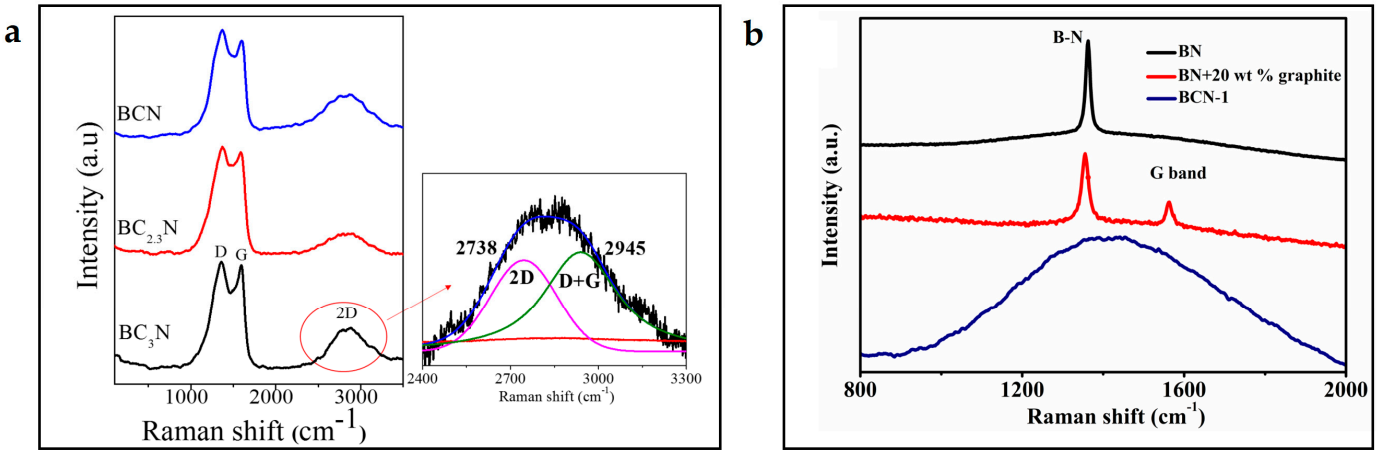

Figure 6. (**a**) Example of Raman spectra of phase-separated BCNs (reprinted with permission from Ref. [85]. Copyright 2020, Wiley); (**b**) Raman spectra of h-BN, a physical mixture of h-BN/graphite, and a homogeneous BCN (reprinted with permission from Ref. [100]. Copyright 2022, Elsevier).

XPS allows for a comprehensive analysis of BCN nanosheets (of several layers) and a surface analysis of bulkier BCNs (with thicknesses greater than a few nanometers). The B 1s spectrum, after deconvolution, should show the two signals due to B–N and B–C bonds. In references [75,78,95,97], these signals are reported to peak at 190.5 ± 0.5 eV and 189.6 ± 0.2 eV, respectively. Other studies have reported peak positions of approximately 191.5 and 190.5 eV [85,92]. Even higher binding energies (1 eV higher) have been proposed for both signals [69]. In all cases, the difference between the two signals is approximately 1 eV. For a BCN monolayer obtained from the single precursor bis-BN cyclohexane, the B

1s spectrum has shown two deconvoluted signals of equivalent intensity, at approximately 189.6 and 189 eV (Figure 7), which have been attributed to the BN_2C and BNC_2 binding motifs, respectively [99]. For the BC_3 binding motif, where boron does not bind nitrogen, the corresponding signal peaks at 189.8 eV [101]. With respect to the BN_3 binding motif, the corresponding binding energy has been reported as approximately 192 eV [79]. The surface of BCNs is often oxidized, as evidenced by a signal at a higher binding energy (192–193 eV) and of lower intensity attributed to B–O bonds [68,78,85,93,97,101]. Comparing the intensity of the signals due to the B–N and B–C bonds provides a qualitative approach to identifying the dominant bonds. For example, a BCN produced from an amine borane precursor generally shows a B–N signal of higher intensity, indicating that boron is primarily bonded to nitrogen [92,95].

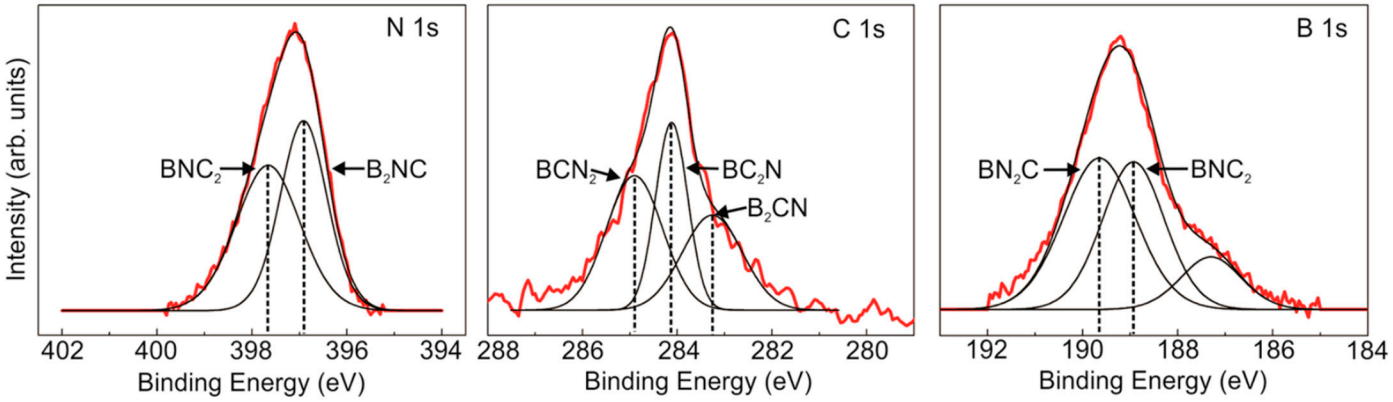

Figure 7. N 1s, C 1s, and B 1s XP spectra of a BCN monolayer obtained from the bis-BN cyclohexane single precursor [99].

The N 1s spectrum, after deconvolution, typically shows two main signals: 398.4 ± 0.5 eV for N–B and 399.8 ± 0.2 eV for N–C [75,89,92,93,97]. However, similar to the deconvoluted B 1s spectrum, there is some discrepancy in the reported binding energies. For example, the signal at 398.8–399 eV has also been ascribed to the N–C bond, while the signal related to the N–B bond has been reported to peak at lower binding energies (397.7 eV) [78,85]. A closer examination reveals other signals such as pyridinic nitrogen at 398.2 eV, pyrrolic nitrogen at 399.2 eV, and graphitic nitrogen at 400.8 eV [69,73,79]. The oxidation of nitrogen in a BCN leads to N–O bonds, which are observable at higher binding energies. Values between 400.5 and 405 eV have been reported [68,94]. Binding energies a few tenths above 400 eV have also been attributed to terminal N–H and pyridinic N–C bonds [79,85]. For a BCN monolayer directly obtained from bis-BN cyclohexane, the N 1s spectrum has shown two deconvoluted signals of roughly equivalent intensity, at approximately 397.7 and 397 eV (Figure 7), which are attributed to the BNC_2 and B_2NC binding motifs, respectively [99].

The deconvoluted C 1s spectrum usually shows signals corresponding to the C–B, C–N, and C–C bonds. The binding energies evidencing C–B bonds are observed at 283.7 ± 0.6 eV, while the C–N bond is observed at higher binding energies, typically around 285.7 ± 0.5 eV [68,85,92,93,95]. In some studies, the deconvolution has allowed for the distinction between sp^2 and sp^3 C–N bonds, with binding energies of 286.0 ± 0.5 and 287.7 ± 0.4 eV, respectively; additionally, the presence of sp^2 C–C bonds at 284.4 ± 0.4 eV and sp^3 C–C bonds at 285.2 eV has been detected. In the BCN monolayer directly obtained from bis-BN cyclohexane, the C 1s spectrum has shown three deconvoluted signals, at approximately 285, 284 (most intense), and 283.2 eV (less intense) (Figure 7), which are attributed to the BCN_2, BC_2N, and B_2NC binding motifs, respectively [99]. The partial oxidation of carbon (e.g., at defect sites) may occur during synthesis or post synthesis. The

C–O bonds have been associated with oxidation, with surface functional groups, or with adsorbed CO_2, and they are visible between 287 and 290.5 eV [69,78,89,92].

The O 1s spectrum is also useful for cross-checking the possible oxidation of BCN, as indicated by the spectra discussed above. The signals due to O–B and O–C bonds are, for example, visible at 532.5 eV and 531.4 eV, respectively, while the presence of O–H can be detected at higher binding energies [73].

MAS NMR has been employed to identify the chemical environments within BCN materials, using ^{11}B, ^{13}C, and ^{15}N nuclei to provide insights into their structural properties. Different environments have been identified for ^{11}B MAS spectra: between 20 and 30 ppm, trigonal planar BN_3 environments attributed to BN graphitic layers and terminal BN_2H are present; the signals between 0 and 15 ppm are associated with trigonal and tetragonal BO_x environments; and BC environments occur between −7 and 0 ppm [113,125,126]. These assignments were supported by Chen et al., by analyzing commercial h-BN, B_2O_3, and B_4C, which exhibited single peaks centered at 22 ppm, 12 ppm, and −5 ppm, respectively [127]. This same study employed Cross-Polarized ^{15}N MAS NMR to analyze the samples, identifying three distinct nitrogen environments: N–B_3 at −340 ppm, BNH_x at −308 ppm, and N–C at −275 ppm. ^{13}C MAS NMR spectra of BCNs have shown signals for C–C environments at 125 ppm, attributed to graphitic carbon as in graphene oxide or graphite, and C–N environments at 157 ppm, assigned to C_3N_3 rings [122,125]. Zeng et al. reported the synthesis of a homogeneous BCN that displayed a signal at 139 ppm, which was also assigned to sp^2-hybridized carbon atoms; however, in this case, it is likely that the well-mixed B, C, and N atoms in the sample shifted the signal towards a higher chemical shift [100].

Other techniques, though scarcely used, are X-ray Absorption Near-Edge Structure (XANES) and fluorescence spectroscopy. The C K-edge XANES spectrum shows a peak at 288.5 eV, which is characteristic of the chemical state of carbon atoms in BCNs [75]. In fluorescence spectroscopy, the BCN surface is first labeled with fluorescent molecules, which selectively attach to surface carbonyl, carboxyl, hydroxyl, and amine groups, and then analyzed. This approach allowed for the observation of all of these groups in BCNs prepared from exfoliated graphene boric acid and urea [76].

2.2.4. Optic Analyses

BCN thin films obtained by CVD using trimethylamine borane as a precursor absorbed UV-Vis radiation at about 201 and 205 nm [97]. The former absorption corresponds to h-BN, while the latter indicates bandgap narrowing due to substitutional doping, as expected for a BCN. This was further supported by computational prediction using the nearest-neighbor tight-binding model and quantum confinement [128]. The optical bandgap of BCNs can be modulated by changing the carbon content. For a BCN obtained by a solid-state reaction of graphene or charcoal, boric acid, and urea, the bandgap increased from 1.93 eV for the composition $(BN)_{0.28}(C)_{0.72}$ to 3.41 eV for $(BN)_{0.7}(C)_{0.2}$. The increase in the optical bandgap with a decreasing carbon content has been explained by a decrease in the π states from sp^2 carbon [77]. Similar trends in bandgap evolution have been reported elsewhere [39,89].

The target sputtering of B_4C and BN under ultra-high vacuum produced BCN films with different bandgaps, varying from 1.9 to 3.7 eV and depending on the compositions of the materials [68]. In this case, it was found that the increase in the optical bandgap was related to the increase in the nitrogen content in the structure. The modulation of the bandgap is also possible by changing the boron content in BCNs [83,88]. By analyzing g-C_3N_4 synthesized from melamine and a BCN obtained from a mixture of melamine and boric acid, the respective bandgaps were found to be 2.78 eV and 3.41 eV [79]. The introduction of boron into the structure increases the bandgap and reduces the conduction

band values compared to g-C_3N_4. This is explained by charge localization at the BN units of the BCN, resulting in a redistribution of the π-state charges in the lattice.

The UV-Vis spectrum can also be used to distinguish between phase-separated and homogeneous BCNs [93]. The graphitic nanodomains doped with nitrogen and boron absorb at 250 nm, and they present a blue shift of the π-band compared to graphite. The h-BN-rich region doped with carbon shows an absorption peak at 200 nm and a reduced bandgap compared to h-BN.

2.2.5. Quantification of Acidic and Basic Sites

Temperature-Programmed Desorption (TPD) is a valuable technique for assessing the acidity and basicity of materials. TPD with CO_2 as a probe molecule (CO_2-TPD) can be used to identify basic sites, while TPD with NH_3 as a probe molecule (NH_3-TPD) detects acidic sites. In both methods, a higher desorption temperature of the probe molecule correlates with stronger basic or acidic sites. For example, in CO_2-TPD, basic sites are classified based on desorption temperature: weak basic sites (30–350 °C), medium basic sites (350–600 °C), and strong basic sites (>600 °C). BCN materials synthesized using various precursors and methods display differing acidity and basic levels, influenced by specific B and C doping levels, functional group presence, and defect formation.

B doping in g-C_3N_4 increases both acidic and basic sites compared to undoped g-C_3N_4, with basic site density rising from 0.137 to 0.675 mmol g^{-1} and acidic site density from 0.057 to 0.173 mmol g^{-1} [129]. Similar findings from other studies confirm that boron incorporation into g-C_3N_4 enhances both types of active sites [80,130]. Wang et al. observed that increasing the pyrolysis temperature of a BCN derived from $NaBH_4$, NaN_3, and alcohol decreased the basicity of the material [112]. Additionally, Lei et al. noted an increase in the CO_2 desorption peak intensity with higher carbon content in h-BN [131]. A mesoporous BCN synthesized by Sathish et al. showed a total basicity of 0.813 mmol g^{-1}, with weak basic sites contributing 0.111 mmol g^{-1} and strong basic sites 0.702 mmol g^{-1}, explaining its high affinity for CO_2 capture [107].

Weak basic adsorption sites are associated with −OH and $-NH_2$ functional groups, while medium basic sites are attributed to defects created by dopant elements [81]. UV irradiation has been shown to excite negative charges within BCN materials, further enhancing their basicity and thus increasing their CO_2 adsorption capacity [132].

3. Application of Borocarbonitrides in Decarbonization Technologies

3.1. Gas Adsorption

Using porous materials for gas adsorption has attracted significant attention due to their efficiency and selectivity in capturing and storing gases. These materials must possess key properties, including a high adsorption capacity, a large specific surface area, adjustable pore sizes, a high density of adsorption sites, chemical stability, and recyclability. BCNs exhibit these characteristics, making them promising candidates for applications like CO_2 capture and H_2 storage—both critical for advancing renewable energy solutions.

Table 1 summarizes the few BCN materials developed for H_2 storage at 1 bar of pressure and −196 °C. Like most porous materials considered for storing H_2, BCNs physically adsorb H_2 under such cryogenic conditions [133–135], allowing a storage capacity of 1 to about 3 wt%. Based on the data provided, it seems that there is not a clear relationship between the SSA and the amount of H_2 stored at 1 bar, whereas, in general, the H_2 uptake is proportional to the SSA [136]. This non-linear trend can be explained by different reasons, one important one being related to the discrepancies and errors in the methods and apparatuses used to measure the amount of adsorbed H_2 [137]. It thus appears to be irrelevant to further discuss the data listed in Table 1. Despite this, these few H_2 uptake

data confirm that porous BCN is able to store H_2 under cryogenic conditions. Improved textural properties and an excellent understanding of the surface properties of BCNs could open new prospects for BCNs in storing this light gas at temperatures higher than −196 °C.

Table 2 presents the BCN materials investigated for CO_2 adsorption under near-room conditions. Some of these materials demonstrate superior CO_2 adsorption capacities at higher pressures, which opens the possibility for high-pressure underground storage. At 1 bar CO_2 and 25 °C, BCN materials have demonstrated adsorption capacities ranging from 0.67 to 3.91 mmol g^{-1}. When reported, the isosteric heat of adsorption falls between 12 and 72 kJ mol^{-1}, indicating that CO_2 molecules undergo physisorption on the material. To date, there is no experimental evidence of chemisorption for BCN materials. Different features of BCN materials that enhance adsorption capacity have been experimentally identified.

A clear trend in the reviewed literature suggests that micropores predominantly control the adsorption capacity at low pressure (e.g., 1 bar). As microporosity increases, so does the CO_2 adsorption capacity [32,106,107,127,138]. At higher pressures (e.g., 30 bar), the SSA becomes more important, with larger pores being filled. Another feature that enhances the adsorption is the polar B−C and C−N bonds, along with functional groups like $-NH_2$ or –OH, which act as adsorption sites for CO_2 molecules [103,138]. These functional groups increase the basic character of the material, enhancing CO_2 binding. Additionally, C and O atoms within the BCN structure generate structural defects, which also serve as adsorption sites. For CO_2 adsorbents, good recyclability is essential. BCNs have demonstrated this property at the laboratory scale, showing a cyclability of between 96 and 100% after five to nine adsorption/desorption cycles [96,111,127].

Table 1. H_2 adsorption capacity (mol number adsorbed per gram, n_{ads}, and in wt%) at 1 bar H_2 and −196 °C and specific surface area, SSA, of different BCN materials.

Material	n_{ads} (mmol g^{-1})	wt%	SSA (m^2 g^{-1})	Ref.
Nanoporous coral-like BCN	16.3	3.26	988	[103]
Two-dimensional porous BCN	14.5	2.91	3310	[106]
Graphene-like BCN	13	2.60	2911	[139]
Nanoporous BCN	5.35	1.07	1560	[125]

Table 2. CO_2 adsorption capacity (mol number adsorbed per gram, n_{ads}, and in wt%) at 1 bar CO_2 and 25 °C, isosteric heat of adsorption, −ΔH (when available), and specific surface area, SSA, of different BCN materials.

Material	n_{ads} (mmol g^{-1})	wt%	−ΔH (kJ mol^{-1})	SSA (m^2 g^{-1})	Ref.
Porous BCN	3.74–3.91	16.5–17.2	33.5 ± 1.5	727	[127]
Microporous BCN	3.23	14.2	33 ± 2	511	[96]
Two-dimensional porous BCN	2.39	10.5	-	3310	[106]
BCN with oxygenated surface	2.38	10.4	23.7 ± 1.4	2991	[32]
C-doped BN–UV irradiation	2.38	10.4	-	-	[132]
Nanostructured BN/C spheres	1.97	8.6	27.5 ± 2.5	767	[111]
C/BN composite	1.94 [a]	8.5a	12 ± 4	56	[113]
Mesoporous BCN	1.64	7.2	14.1 ± 7.6	1166	[107]
Nanoporous coral-like BCN	1.36	6	-	988	[103]
Graphene-like BCN	1.16	5.1	-	1991	[140]
Carbon-doped BN	0.73	3.2	72	368 [b]	[138]
Graphene-like BCN	0.67	2.9	-	2911	[139]

[a] At 1.5 bar CO_2 and 30 °C; [b] SSA of micropores.

BCNs exhibit promising properties for CO_2 adsorption, with various structural features identified as potential adsorption sites. Different density functional theory (DFT)

studies have been conducted to further explore these features. Rao and colleagues identified different adsorption sites within BCN structures (Figure 8), including (i) boron atoms bonded to three nitrogen atoms, (ii) negatively charged nitrogen atoms bonded to at least one carbon atom, (iii) carbon atoms bonded to two nitrogen atoms, (iv) boron atoms bonded to both a carbon and a nitrogen atom, and (v) hexagonal rings consisting of four carbon atoms, one nitrogen atom, and one boron atom [139,140]. Mishra et al. compared the CO_2 adsorption energy of BCNs to that of graphene, showing a stronger interaction between CO_2 and BCN nanosheets (-18.91 kJ mol^{-1}) compared to graphene (-13.19 kJ mol^{-1}) [141]. The adsorption was particularly strong at boron atoms located near the carbon–boron nitride interface. They also observed a trend in the adsorption energy for different gas molecules, ranking $CO_2 > CH_4 > H_2$.

Further, Ibarra-Rodriguez and Sanchez showed that boron atoms in B-doped carbon nitride structures can form chemical bonds with various gas species [142], and they found adsorption energies in the following order: SO_2 (-103 kJ mol^{-1}) > NH_3 (-101.3 kJ mol^{-1}) > C_2H_4 (-67.3 kJ mol^{-1}) > CO_2 (-64.6 kJ mol^{-1}) > CH_4 (-11.6 kJ mol^{-1}). However, the calculated CO_2 adsorption energy is three times higher than that calculated by Mishra and collaborators. Sathish et al. determined that CO_2 adsorbs on different sites of BCN structures, with a preference in the order of B–C > C–C > B–N > C–N sites [107]. Furthermore, Moghaddam et al. suggested that BC_2N nanotubes could strongly capture CO_2, although recovering the gas under ambient conditions may be challenging due to the strength of the interaction [143].

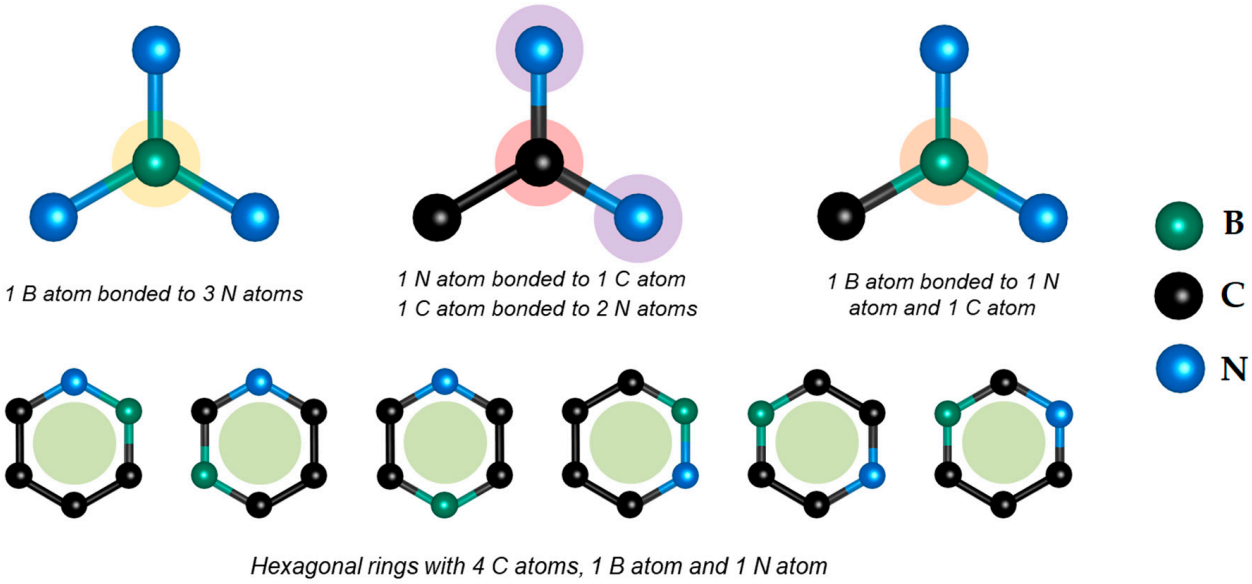

Figure 8. Adsorption sites on BCN structures based on the DFT calculations made by Rao and colleagues, adapted from [139,140]. The adsorption sites are indicated by the colored circles. The green, black, and blue spheres represent boron, carbon, and nitrogen atoms, respectively.

Some strategies have been proposed to enhance the gas adsorption capacities of BCNs. Portehault et al. suggested that to improve hydrogen uptake by BCNs, a higher SSA and a higher C:B ratio are required [125]. To increase CO_2 adsorption, creating structural defects and incorporating functional groups such as $–NH_2$ and –OH has been recommended. BCNs also exhibit excellent light adsorption in the UV range. Duan et al. irradiated BCN materials with UV light, improving the CO_2 adsorption by up to 28% at 1 bar CO_2 and 25 °C [132]. The improvement was attributed to two factors: (i) UV irradiation generates electrons in the BCN structure, increasing its Lewis basicity and thus enhancing attraction to CO_2 (a Lewis acid), and (ii) UV irradiation excites more negative charges within the

material, strengthening the interaction between CO_2 and BCN. Other approaches have been suggested based on theoretical calculations. One study demonstrated that doping BCN monolayers with O and Si atoms can increase their attraction to CO_2, potentially inducing chemisorption [144]. Khan et al. proposed a 2D pentagonal BCN structure, where B, C, and N atoms form five-membered rings instead of the hexagonal arrangement [145]. According to their calculations, this structure is mechanically, thermally, and dynamically stable, capable of chemisorbing CO_2 molecules. In this case, the C and O atoms of CO_2 would form chemical bonds with the N and B atoms of the BCN structure, respectively. However, such pentagonal structures have yet to be demonstrated experimentally.

BCNs have demonstrated a higher CO_2 adsorption capacity compared to similar materials. Pristine g-C_3N_4 (i.e., non-functionalized) is not an efficient CO_2 adsorbent [146], with reported adsorption capacities ranging from 0.18 to 0.25 mmol g^{-1} at 25 °C [147,148]. Pristine BN structures have shown higher adsorption capacities under ambient conditions (25 °C, 1 bar CO_2), with values ranging from 0.08 to 2.25 mmol g^{-1} [149–151]. As shown in Table 2, BCNs exhibit even more promising adsorption capacities. This advantage can be attributed to their higher density of active sites, resulting from the unique chemical environment created by the presence of boron, carbon, and nitrogen atoms. Therefore, tuning the BCN composition could potentially enhance its CO_2 adsorption capacity. Finally, there is still room for improving the SSA of BCN materials.

Compared to other materials used for CO_2 adsorption, such as MOFs, BCNs also present some advantages. Although MOFs generally exhibit higher CO_2 adsorption capacities (1.3 to 5.5 mmol g^{-1} at 1 bar and 25 °C) [152,153], BCNs offer superior thermal and chemical stability, as they are synthesized through pyrolysis at temperatures of between 800 and 1200 °C, making them promising candidates for applications requiring robust and durable materials. Moreover, functionalizing BCN structures offers a pathway to enhance their CO_2 adsorption capacity, yet this approach remains relatively unexplored, leaving room for further improvement.

3.2. Metal-Free Catalysis

3.2.1. CO_2 Cycloaddition

Utilizing CO_2 as a raw material helps to reduce greenhouse gas emissions and enables the production of valuable products. One promising route is the conversion of CO_2 into cyclic carbonates (Figure 9), which have a wide range of applications, including electrolytes or solvents [154]. The success of this process depends on developing effective catalysts that can activate both CO_2 and epoxides for cycloaddition.

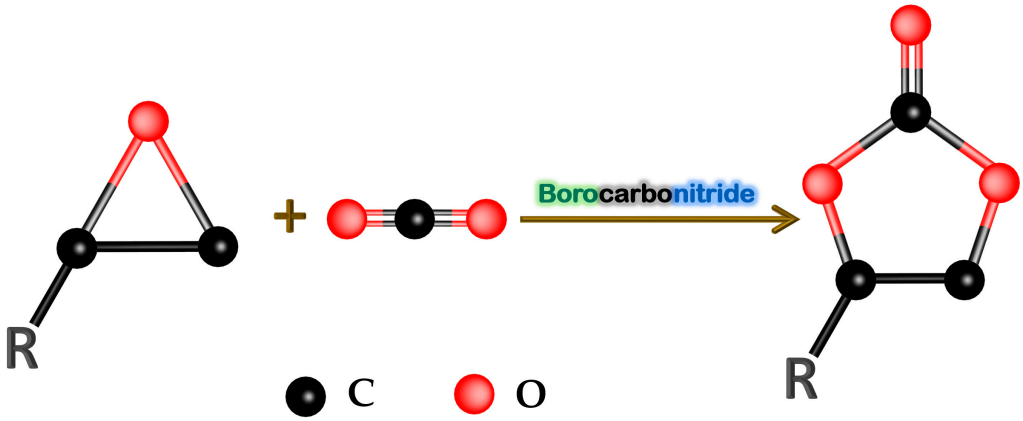

Figure 9. Schematic representation of the cycloaddition reaction of an epoxide and CO_2 to a cyclic carbonate. The black and red spheres represent carbon and oxygen atoms, respectively.

Although CO_2 is an ideal C1 source, its strong C=O bonds make it difficult to activate. Catalysts that donate electrons to the antibonding orbital of CO_2 are necessary for overcoming this challenge. Electron-rich catalysts, particularly those with Lewis acidic and basic properties, can enhance the reaction by facilitating the ring opening of epoxides. Moreover, hydrogen bond donors can polarize the C−O bonds of epoxides, forming hydrogen bonds with the O atom of the epoxide, facilitating the opening of the ring. Graphitic carbon nitride (g-C_3N_4) has been used as a catalyst for the CO_2 cycloaddition of epoxides, as it is rich in hydrogen bond donors such as -NH_2 and -NH groups [155]. By doping CN with boron, both acidic and basic Lewis sites are created in the structure, and thus, boron-doped g-C_3N_4 has been reported as a promising catalyst for the CO_2 cycloaddition of epoxides.

Su et al. synthesized B-doped g-C_3N_4 using melamine and the ionic liquid 1-butyl-3-methylimidazolium tetrafluoroborate ($BmimBF_4$) [102]. They found that adjusting the $BmimBF_4$ content allowed control over the polymerization degree, crystallinity, and pore size of B-doped g-C_3N_4. Lower polymerization and crystallinity resulted in more structural defects and increased the presence of functional groups like –NH and –NH_2, which enhanced the catalytic activity. A higher ratio of meso- and macropores also contributed to improved performance. Under reaction conditions of 28 bar CO_2, 130 °C, and 24 h of reaction time, they achieved a 31% yield of propylene carbonate from propylene oxide with 99.9% selectivity. For epichlorohydrin, the yield was even higher at 89% with 98% selectivity.

The catalyst remained completely active after five cycles. Zhang et al. prepared B-doped g-C_3N_4 by calcining urea and boric acid at 450 °C [130]. They identified boron in two positions within the structure: by replacing C atoms bonding to three N atoms or forming –$NB(OH)_2$ groups at the edges. This catalyst effectively converted a bisepoxide, the 1,4-butanediol diglycidyl ether, into its respective carbonate at 20 bar CO_2 and 130 °C over 20 h. Three key factors contributed to the catalytic efficiency of their B-doped g-C_3N_4: (i) a large SSA, introduced by boron doping, which provided more active sites and enhanced reactant adsorption; (ii) a lower crystallinity and polymerization degree, leading to more edge defects, which were due to the low calcination temperature; and (iii) the formation of Lewis acid with –$NB(OH)_2$ groups, resulting in an acid–basic catalyst.

Despite these findings, B-doped g-C_3N_4 alone requires harsh reaction conditions or additional modifications of the catalyst for optimal performance. Doping with other elements or using co-catalysts has been necessary to further enhance activity. For instance, Zhu et al. used silica (SBA-15) to support B-doped g-C_3N_4 and improve its catalytic activity [80]. They observed an increase in the conversion of styrene oxide to styrene carbonate, from less than 5% (without a catalyst) to 20% with CN, 74.2% with B-doped g-C_3N_4, and 97.8% with B-doped g-C_3N_4 supported on SBA-15, with 95% selectivity. Chand et al. used potassium iodide (KI) as a co-catalyst to improve the catalytic performance of B-doped g-C_3N_4 nanosheets synthesized from dicyandiamide and boric acid [129]. This increased the yield from 56% (without KI) to 73% (with KI). They also observed that epoxides containing heteroatoms yielded higher conversions, as these atoms exhibited strong binding affinity to surface groups like –NH_2 through hydrogen bonding. Other studies have shown additional dopants to be effective. Wang et al. enhanced the catalytic activity of g-C_3N_4 by doping it with boron and potassium and using tetrabutyl ammonium bromide as a co-catalyst [81]. The ring opening of the epoxides was facilitated by the nucleophilic attack of Br^-, while K^+ stabilized the intermediate oxyanion. Yang et al. doped g-C_3N_4 with phosphorus and boron, forming more active sites and achieving improved yields of propylene carbonate from propylene oxide [82].

A proposed mechanism has been suggested (Figure 10) [80]. The reaction mechanism starts with the BCN catalyst denoted (1). The epoxide is adsorbed onto acidic –$NB(OH)_2$

sites through hydrogen bonding, activating the epoxide for the subsequent reaction (2). Simultaneously, the adsorption of CO_2 onto basic NH sites of the catalyst occurs, where it is activated into a carbamate species through the formation of N–C bonds and the cleavage of N–H bonds in (2). The hydrogen atom then interacts with an oxygen atom from CO_2 and is stabilized via hydrogen bonding with a neighboring nitrogen atom, leading to (3). The activation of the ring facilitates a nucleophilic attack by the oxygen anion of the carbamate species, leading to the ring opening of the epoxide (3). The newly formed intermediate, with a negatively charged oxygen, then attacks the carbon atom of CO_2, resulting in the formation of the cyclic carbonate, as shown by (4). The final steps involve the cleavage of the N–C bond and the return of the hydrogen to its original nitrogen site, as in (5). Finally, the desorption of the cyclic carbonate takes place, and the catalyst (1) is regenerated. The cooperative actions of –NH, $–B(OH)_2$, and N-containing groups are crucial for this catalytic process.

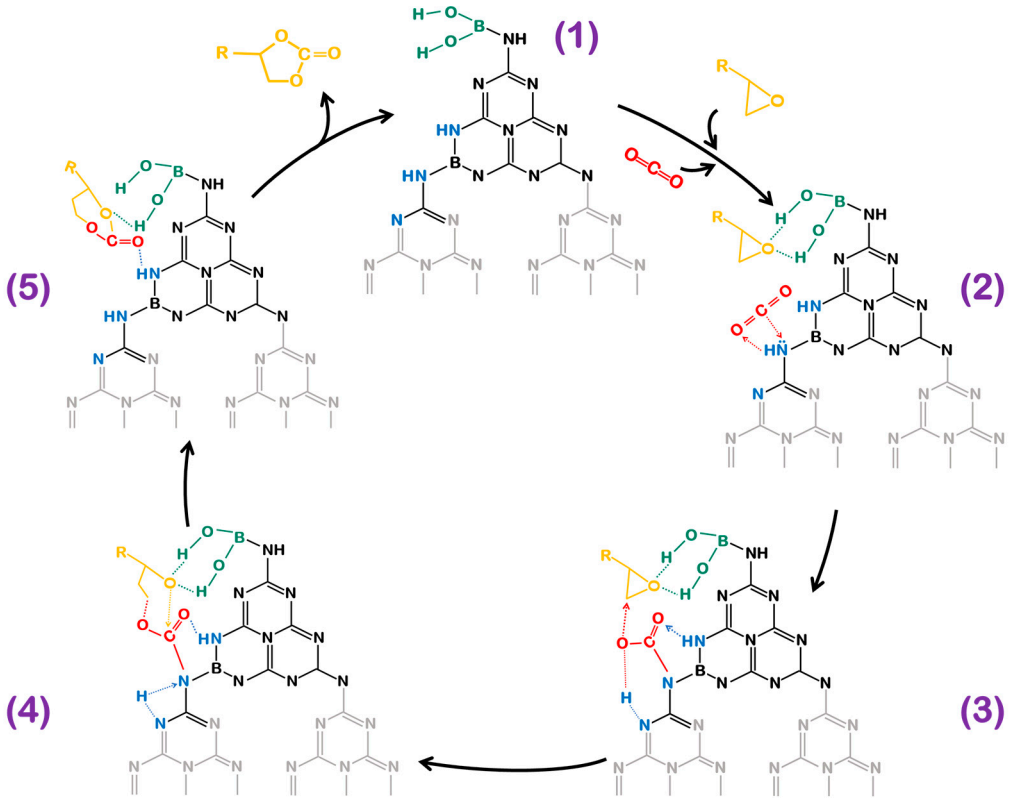

Figure 10. Proposed mechanism for the cycloaddition of CO_2 and an epoxide on a BCN catalyst. Adapted from [80].

3.2.2. Desulfurization of Fuels

Removing organic sulfides from crude oil is essential for producing high-quality fuels like diesel and preventing the emission of harmful sulfur oxides (SO_x). Oxidative desulfurization (ODS) is an effective technology for this purpose. This two-step process involves the catalytic oxidation of sulfides (in the presence of an oxidant), followed by their extraction in mild conditions. The primary challenge in ODS is developing an effective catalyst, and BCN has been proposed as a possible, efficient, metal-free catalyst [156]. With the development of liquid organic hydrogen carriers as possible hydrogen carriers in the field of hydrogen storage production [157], the extraction of such carriers from crude oil may require desulfurization, as for diesel, which may make ODS an important catalytic process in the field of sustainable fuels.

Lu et al. produced a series of BCN materials through a pyrolysis process involving boric acid, urea, and 1-hexadecyl-3-methylimidazolium chloride as a carbon source [43]. BCNs with SSAs ranging from 514 to 730 $m^2\ g^{-1}$ were obtained by adjusting the carbon content. They were evaluated as catalysts for the oxidative desulfurization (ODS) of dibenzothiophene in air at 100 °C. Under these conditions, 100% sulfur removal was achieved. Such catalytic activity has been attributed to the enhanced π-electron delocalization within the BCN framework, resulting from the incorporation of carbon into the BN lattice. This delocalization facilitates electron transfer to O_2 and promotes the formation of O_2^- radicals, which are essential for the efficient oxidation of sulfur compounds. Similar conclusions were drawn by Wei et al., as they also show how important π-electron delocalization within the BCN framework is for the activation of O_2, which has been reported to take place on the zig-N edges of BCN [158].

An alternative desulfurization method involves the adsorption of organic sulfides onto a sorbent, followed by the separation of the purified fuel from the spent sorbent. Luo et al. explored this approach using BCN aerogels synthesized from boric acid, melamine, and glucose [108]. A three-step process, including polymerization at 85 °C in water, freeze-drying, and pyrolysis at 1000 °C, yielded BCNs with SSAs as high as 1220 $m^2\ g^{-1}$. These BCNs possess abundant Lewis acid sites (although their exact nature remains unidentified) that can adsorb organic sulfides through the lone pair electrons on the sulfur atoms. The adsorption mechanism is driven by π–π interactions between the BCN surface and the sulfur-containing compounds.

It is worth noting that adsorption is the initial step in catalytic ODS [43]. Therefore, the metal-free BCN plays a dual role in catalytic ODS: it acts as both a sorbent for organic sulfides and an activator for O_2.

3.2.3. Oxidative Dehydrogenation

The oxidative dehydrogenation (ODH) reaction is commonly employed to convert light alkanes, like ethane and propane, into olefins (such as ethylene and propylene) by removing hydrogen atoms and incorporating oxygen. Unlike traditional dehydrogenation, ODH uses an oxidant as a reactant, such as O_2 or SO_2, to drive the reaction forward and minimize unwanted by-products [159]. BCNs have shown promising performance as catalysts for ODH reactions using this method [119,160–165].

A more environmentally friendly approach involves using CO_2 as a mild oxidant for ODH. CO_2 offers several advantages over stronger oxidants [166]: (i) increased selectivity, as it is less likely to over-oxidize hydrocarbons, which enhances product selectivity; (ii) improved safety, given that CO_2 is easier to handle than other oxidants; (iii) catalytic benefits, as it can interact with catalyst surfaces to potentially promote dehydrogenation and suppress coke formation; and (iv) decarbonization potential, as it utilizes a greenhouse gas as a reactant. Despite these advantages, to the best of our knowledge, only one study has investigated the ODH transformation of alkenes using BCNs as catalysts and CO_2 as an oxidant. Wang et al. used BCN nanosheets obtained from a mixture of $NaBH_4$, NaN_3, and an alcohol as a catalyst for the conversion of ethylbenzene to styrene using CO_2 as a soft oxidant [112]. Under comparable conditions without a catalyst, the reaction achieved less than 1% conversion. However, with BCN nanosheets, an 8% ethylbenzene conversion was observed, with a styrene selectivity exceeding 95%. The conversion rate, however, declined from 8% to 3% after one hour. Although the initial conversion rate is relatively low, this study demonstrates the potential of BCN catalysts to perform ODH reactions using CO_2 as an oxidant.

Beyond alkane-to-alkene transformations, ODH can also be applied to convert methanol into formaldehyde, which is considered a potential hydrogen carrier. Zhang

et al. developed BCN nanotubes from boric acid, urea, and polyethylene glycol as a catalyst for methanol-to-formaldehyde conversion, achieving a methanol conversion rate of approximately 29% with a selectivity of 54%, outperforming pure boron nitride and nanocarbon [167]. The side-products of this reaction included CO_2, dimethyl ether, and a minor quantity of dimethoxyethane. The study highlighted that specific functional groups facilitated different reactions: carboxylic acid groups promoted acid-catalyzed methanol dehydration to dimethyl ether. Ketonic carbonyl and B–OH groups facilitated redox catalysis for methanol ODH to formic acid. Although BCN nanotubes exhibited lower performance than conventional industrial catalysts, their activity was comparable to or better than other metal-based catalysts, underscoring the potential of BCNs as substitutes for metal-based catalysts in ODH reactions.

3.3. Photocatalysis

Photocatalysis employs semiconductor materials as catalysts to drive chemical reactions. When a semiconductor is exposed to light with a wavelength (λ) that exceeds the wavelength corresponding to its bandgap energy, electrons in the valence band become excited and transition to the conduction band, leaving positively charged holes behind in the valence band [168]. The photogenerated electron–hole pairs in the semiconductor facilitate different redox reactions.

Two metal-free materials that have garnered interest as photocatalysts due to their favorable electronic band structure, chemical stability, abundance, and ease of fabrication are g-C_3N_4 and h-BN. However, their practical application faces challenges due to limited solar light absorption, a low SSA, and rapid charge recombination [169,170]. A key aspect to improve these aspects is to engineer the electronic bands of pristine g-C_3N_4 and h-BN through the introduction of doping elements into their structure, such as C atoms in h-BN or B atoms in g-C_3N_4 [171]. This is why B-doped g-C_3N_4, as well as BCNs, has shown an improvement in photocatalytic performance compared to pristine g-C_3N_4.

BCNs have shown photocatalytic activity for different reactions such as the amination of arenes, decarboxylation reactions, the degradation of organic compounds, the hydroxylation of aromatic compounds, the dehydrogenation of heterocycles, and alcohol oxidation [121,162–183]. In this review, and hereafter, we will examine their performance in decarbonization approaches, focusing on photocatalytic hydrogen generation and CO_2 transformation.

3.3.1. CO_2 Photoreduction

By adjusting the content of carbon, boron, and nitrogen atoms in BCNs, it is possible to tune the properties of these compounds. This makes BCNs highly suitable for photocatalytic applications, particularly due to their potential for bandgap engineering, good charge transfer capacities, and oxidation stability [34]. Being metal-free and composed of lightweight, abundant elements, BCNs have advantages over other materials. Additionally, they contain dual Lewis acid–base sites that interact with both the bonding and antibonding orbitals of CO_2, facilitating its reduction.

Different research teams have investigated BCNs as photocatalysts for CO_2 transformation. Wang's group is one of them. In the first study reported using a BCN as a catalyst for CO_2 photochemical conversion, the group demonstrated CO_2 reduction under visible light, producing 9.3 μmol of CO and 2.9 μmol after 2 h of reaction, using a BCN material with a bandgap of 2.72 eV [122]. To enhance the photocatalytic activity, the group synthesized BCNs with novel structures, such as a 3D porous BCN aerogel tested in photoredox catalysis [184]. This structure enabled direct CO_2 conversion using $Co(bpy)_3Cl_2$ and triethanolamine (TEOA), yielding 6.8 μmol h^{-1} of CO, which was three

times higher than the bulk BCN. In another study, the team incorporated CdS to improve the photoreduction properties of BCN materials, producing a composite with a bandgap of 2.64 eV (Figure 11) [185].

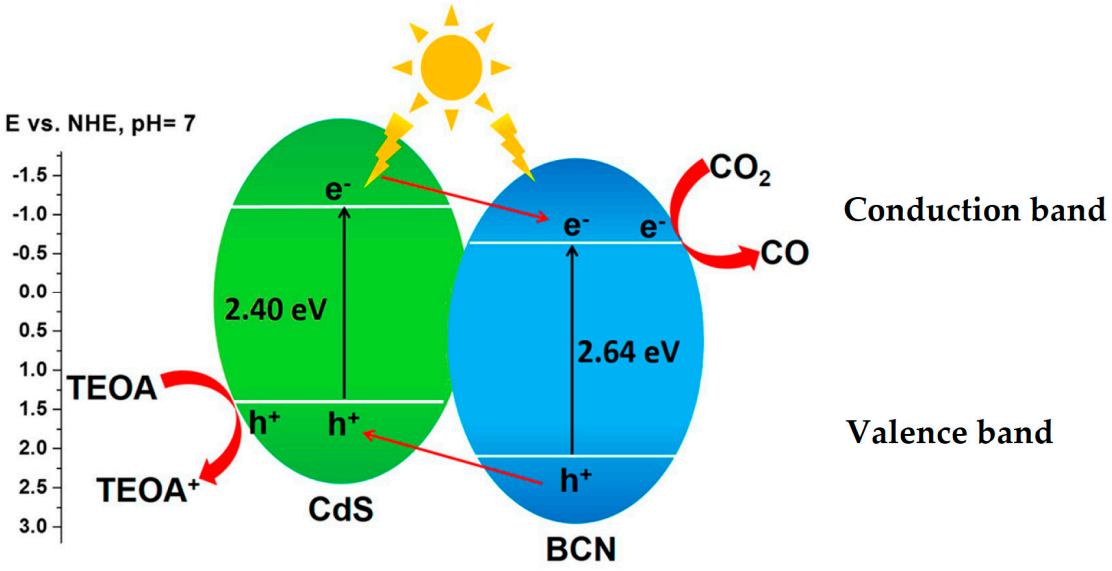

Figure 11. Proposed mechanism for CO_2 photoreduction by a BCN/CdS composite. Reprinted with permission from Ref. [185]. Copyright 2018, American Chemical Society.

Transient photocurrent spectroscopy revealed enhanced charge carrier mobility compared to the pristine BCN, with further improvements in charge transfer due to the formation of a heterojunction between the BCN and CdS, reducing the recombination of photoinduced electron–hole pairs. The BCN/CdS composite was tested for CO_2 reduction, using TEOA as an electron donor and $Co(bpy)_3Cl_2$ as a co-catalyst. While the pristine BCN produced 2 μmol h^{-1} of CO, the composite achieved a significantly improved 12.5 μmol h^{-1}. Although the catalyst lost 20% of its activity after cycling, this was mainly due to photocatalyst loss during recovery.

In a further study, the group introduced $ZnIn_2S_4$ layers into an ultrathin BCN structure to further enhance its photoreduction capabilities [72]. This material, with a bandgap of 2.82 eV and n-type semiconductor behavior, demonstrated a CO production rate of 38.6 μmol h^{-1} with a selectivity of 81.8%. After five cycles, the catalyst maintained its activity. The improvement in CO production was attributed to the close interfacial contact between the two semiconductors, which enhanced charge separation and the migration of photogenerated carriers. In a recent study, the group examined the photocatalytic activity of a defect-rich BCN for the hydrocarboxylation of alkenes using CO_2 [186]. The defect-rich BCN exhibited increased catalytic redox activity compared to the non-defective BCN. The hydrocarboxylation of styrene with CO_2 resulted in a 75% yield of the corresponding carboxylic acid after 20 h of light irradiation. When scaled up to gram quantities, a 69% conversion of styrene was achieved. A study from a different group tried to, similarly, enhance the photocatalytic properties of a BCN by constructing a composite of the BCN and α-Fe_2O_3 [187]. The composite successfully reduced CO_2 into CO, with a 55.1 μmol h^{-1} rate, without using co-catalysts or sacrificial reagents. This represented an enhancement to 3.9 times higher than pristine BCN.

The group of Chen has also investigated a BCN for CO_2 conversion. They synthesized a homogeneous BCN with low fluorescence (compared to boron nitride), which suggests that photogenerated electrons were effectively captured by active sites on reactant molecules, thereby enhancing the photocatalytic reaction [100]. In the presence of water and

without the use of sacrificial agents or co-catalysts, this BCN achieved a CO_2 conversion rate of 13.9 μmol g^{-1} h^{-1} and a CH_4 production rate of 1.1 μmol g^{-1} h^{-1}. However, the photocatalyst's activity decreased by 35% in the fourth and fifth cycles, likely due to the accumulation of intermediates, such as $COOH^-$, on the catalyst's surface, which hindered CO desorption from the pores of the material. In a subsequent study, they created a heterojunction between graphene and a homogeneous BCN [123]. The incorporation of graphene extended the light absorption range into the visible region, improved electron–hole pair separation, and reduced the transfer barrier for photo-carriers. This composite achieved a CO_2 reduction rate of 51.1 μmol g^{-1} h^{-1} for CO, with good stability over five cycles.

Other studies have investigated the doping of BCN materials to enhance their photocatalytic activity. Ri et al. prepared BCN nanosheets from urea, boric acid, and glucose [188]. The nanosheets incorporated various alkaline earth metal compounds to modify their photocatalytic activity. The BCN modified with Ca atoms was able to photoreduce CO_2 under visible light, producing 3 μmol h^{-1} of CO and 1 μmol h^{-1} of H_2. They suggested that different boron sites, such as –N=B– and B–O sites, acted as active centers for CO_2 reduction. In two separate studies, Zeng et al. synthesized a BCN modified with fluorine and with yttrium [189,190]. The fluorinated BCN (3.25 wt% F) exhibited photocatalytic CO_2 reduction activity, yielding 25.38 μmol g^{-1} h^{-1} of CO and 14.11 μmol g^{-1} h^{-1} of CH_4, while the Y-doped BCN (2.5 wt% Y) displayed a yield of 10.07 μmol g^{-1} h^{-1} of CO and 2.78 μmol g^{-1} h^{-1} of CH_4. The better performance of the fluorinated BCN was attributed to the induced local spatial polarized electric field on the surface generated by F atoms, which allowed enhanced charge separation and transfer.

3.3.2. Water Splitting

Water splitting refers to the decomposition of H_2O into H_2 and O_2. Various strategies have been developed to achieve this transformation, including photocatalysis. In photocatalytic water splitting, solar light generates the electron–hole pairs at the semiconductor surface that will drive the reaction: electrons reduce protons via the hydrogen evolution reaction (HER), while holes facilitate the oxygen evolution reaction (OER) by oxidizing water. The overall reaction can be represented as follows [191]:

$$\text{semiconductor} + h\nu \rightarrow e^- + h^+ \quad \text{light absorption} \tag{1}$$

$$2H_2O \rightarrow 2H_2 + O_2 \quad \text{overall water splitting} \tag{2}$$

$$2H_2O + 4h^+ \rightarrow O_2 + 4H^+ \quad \text{OER/water oxidation} \tag{3}$$

$$4H^+ + 4e^- \rightarrow 2H_2 \quad \text{HER/proton reduction} \tag{4}$$

In 2015, Huang et al. demonstrated the feasibility of producing hydrogen from water using a BCN as a metal-free photocatalyst. Their findings indicated that increasing the carbon content in the BCN reduced the size of ordered domains, thereby hindering some semiconductor properties of the material [122]. Thaweesak et al. investigated the photocatalytic properties of g-C_3N_4 by developing boron-doped g-C_3N_4 in both bulk and nanosheet forms using AB, NH_4Cl, and dicyandiamide as precursors [86]. The bandgap measurements showed that g-C_3N_4 has a bandgap of 2.68 eV, while bulk B-doped g-C_3N_4 exhibited a reduced bandgap of 2.42 eV, and the B-doped nanosheets had a bandgap of 2.55 eV. This reduction in the bandgap facilitated greater visible light absorption and more efficient charge separation. The photocatalytic activity for the HER was evaluated under visible light ($\lambda > 400$ nm), with g-C_3N_4 achieving an HER rate of 7.3 μmol h^{-1}, bulk B-doped g-C_3N_4 reaching 14.3 μmol h^{-1}, and B-doped nanosheets exhibiting a significantly higher rate of 94 μmol h^{-1}. Besides boron doping, this improvement in the nanosheet form was also attributed to its increased SSA. Doping g-C_3N_4 with other elements alongside

with boron has also shown improvements compared to the pristine carbon nitride: B- and S-doped g-C_3N_4 showed a high hydrogen evolution rate of about 53.2 μmol h^{-1}, which is 8 times higher than the parent g-C_3N_4 [192].

In a different study, Zhang et al. synthesized ultrathin BCN nanosheets from boric acid, melamine, and glucose, which yielded a hydrogen production rate of 3.9 μmol h^{-1} under visible light irradiation, using TEOA as a sacrificial agent and platinum (Pt) as a co-catalyst [105]. In some cases, the redox reaction is not highly efficient, and sacrificial agents, such as the aforementioned TEOA, are used to accelerate the reaction [193]. They noted that the thinnest samples demonstrated lower HER activity due to quantum confinement effects in the BCN, resulting from reduced vertical dimensionality. Additionally, the highly ordered layers in these thinner samples lacked structural defects, which limited the presence of catalytic active sites. Luo et al. explored various carbon sources to produce a BCN [194]. They found that using amylum as a carbon precursor, in combination with urea and boric acid, resulted in BCN nanosheets. Consistent with previous studies, they observed that the 2D structure promoted effective charge carrier separation and transfer. These amylum-derived BCN nanosheets achieved a hydrogen production rate of 110 μmol h^{-1} g^{-1} under visible light irradiation, utilizing Pt as a co-catalyst and TEOA as a sacrificial agent. Further studies have also proposed the involvement of specific functional groups, such as carboxyl and amino groups, as potential active sites to enhance photocatalytic activity [195].

Chen et al. investigated BCN tubes synthesized from a bio-based source, specifically Kapok fibers, with a measured bandgap of 2.74 eV [196]. Using TEOA as a sacrificial reagent and Pt as a co-catalyst, these BCN tubes achieved a hydrogen evolution rate of 2.8 μmol h^{-1} under visible light irradiation. They found that the sample with the highest SSA (151 m^2 g^{-1}) was not the most effective for the HER. Interestingly, this was attributed to the limitations in solid–liquid-phase photocatalysis, where the reaction rate is more constrained by charge separation efficiency than by mass transfer. However, in a subsequent study, a BCN derived from melamine phosphate borate was synthesized, achieving a reduced bandgap of 1.99 eV and an SSA of 160 m^2 g^{-1} [84]. This BCN sample showed enhanced surface reactivity for photocatalytic reactions compared to bulk BCN. Under similar conditions, it achieved a hydrogen production rate of 4.1 μmol h^{-1}. These findings indicate that while SSA is necessary for efficient photocatalytic water splitting, other factors are equally influential, such as the BCN structural characteristics, shortened charge migration pathways, effective electron transport capabilities, and efficient separation of photogenerated charge carriers.

In an initial study, Zhao et al. [197] synthesized B-doped and N-deficient g-C_3N_4 by calcining a mixture of $NaBH_4$ and g-C_3N_4, demonstrating significantly enhanced photocatalytic activity for water splitting. This B-doped g-C_3N_4 exhibited an oxygen generation rate that was six times higher than that of pristine g-C_3N_4, achieving 561.2 μmol h^{-1} g^{-1} compared to 98.6 μmol h^{-1} g^{-1}. This improvement was attributed to the synergistic effect of boron doping and nitrogen deficiencies, which introduced numerous unsaturated active sites, promoting efficient electron excitation and facilitating charge transfer. In a further study, the same group developed a Z-scheme photocatalytic system using electrostatic self-assembly to combine g-C_3N_4 nanosheets with B-doped/N-deficient g-C_3N_4 nanosheets [198]. A Z-scheme configuration involves two distinct photocatalysts working in tandem to split water in a two-step process. In this system, photogenerated electrons at the conduction band of B-doped g-C_3N_4 nanosheets and holes at the valence band of g-C_3N_4 nanosheets recombine at the heterostructure interface. Simultaneously, the remaining photogenerated electrons and holes at the conduction band of g-C_3N_4 nanosheets and the valence band of B-doped g-C_3N_4 nanosheets, respectively, drive water reduction and oxidation reactions, completing the water-splitting process. The photocatalytic experiments

were conducted in pure water using Pt and $Co(OH)_2$ as co-catalysts, with TEOA and $AgNO_3$ as sacrificial agents. This Z-scheme heterostructure achieved H_2 and O_2 production rates of 32.94 μmol h^{-1} and 16.42 μmol h^{-1}, respectively.

3.4. Electrocatalysis

Electrochemical reactions play an important role in energy conversion and storage technologies. However, certain reactions pose challenges that hinder the efficiency and commercial viability of these technologies. For instance, the oxygen reduction reaction (ORR) suffers from inherently slow kinetics, leading to significant energy losses and suboptimal device performance. Without suitable catalysts, this reaction exhibits low efficiency and poor performance. Consequently, there is a critical need for stable catalytic materials with high activity, which has driven interest in BCN materials [33].

BCNs provide excellent chemical stability in reactive and corrosive environments, as well as resilience under highly reactive or high-current conditions. Their hybrid structure creates active sites that enhance catalytic performance, lowering overpotentials and improving reaction efficiencies [199]. Unlike conventional catalysts such as platinum (Pt), BCN materials are composed of abundant and relatively inexpensive elements. Furthermore, their properties can be tailored through doping or morphological modifications, making them versatile and cost-effective candidates for electrochemical applications.

3.4.1. CO_2 Reduction

The electrochemical reduction of CO_2 has gained significant attention as a promising strategy for mitigating climate change and producing valuable chemicals and fuels, such as carbon monoxide, methanol, formic acid, or ethanol. However, complex pathways of CO_2 electroreduction limit the selectivity of the products. BCN materials have shown electrochemical activity for the transformation of CO_2 with good product selectivity, achieving promising Faraday efficiencies (FEs).

Liu et al. prepared boron- and nitrogen-codoped nanodiamond electrodes via a CVD method using a $CH_4/B_2H_6/N_2/H_2$ gas mixture for the electroreduction of CO_2 [200]. For comparison, they also synthesized nitrogen-doped and boron-doped diamond electrodes. The boron-doped diamond electrodes primarily produced formaldehyde and formic acid, with FEs of 53.9% and 26.1%, respectively. The nitrogen-doped diamond electrodes yielded acetic acid and formic acid with FEs of 62.4% and 24.7%, respectively. Notably, the boron- and nitrogen-codoped nanodiamond electrodes achieved an FE of 93.2% for ethanol production. This superior performance was attributed to the synergistic effect of B and N doping, the high nitrogen content, and a reduction in the overpotential for hydrogen evolution. A similar conclusion was made by Cheng et al., where nitrogen- and boron-codoped carbon spheres demonstrated a high FE of 95.1% for CO due to the unique graphitized structure, large specific surface area, and high density of N and B active sites [201].

Jia et al. synthesized a 3D porous carbon material doped with boron and nitrogen by freeze-drying and pyrolyzing a mixture of sodium chloride, ammonium chloride, boric acid, and glucose [202]. The resulting material contained 10.2 at. % nitrogen and 8.86 at. % boron. Electrochemical measurements in a 0.5 M $KHCO_3$ solution saturated with CO_2 revealed that the material produced CO with an FE of 83% at −0.4 V vs. the RHE. The 3D porous structure facilitated the formation of active sites, enhanced ion transfer, and increased electrochemical double-layer capacitance. They also observed that nitrogen doping promoted H* transfer and COOH* generation, while boron doping enhanced the formation of CO_2* and CO* intermediates (Figure 12).

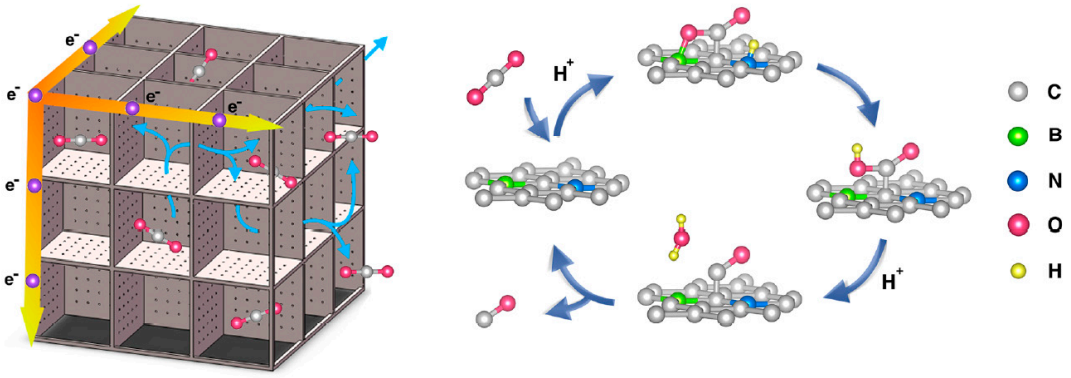

Figure 12. Schema of the electroreduction of CO_2 on a BCN catalyst. Reprinted with permission from Ref. [202]. Copyright 2020, American Chemical Society.

A high nitrogen content was further emphasized as a critical factor for enhancing the electrocatalytic activity of BCNs [203]. Ayyub et al. identified pyridinic nitrogen sites as the most active among all nitrogen species in a BCN for CO_2 electroreduction, facilitating H* transfer, while boron sites stabilized the COOH* intermediate [204]. The BCN prepared by this research group achieved an FE of 98% for CO production at −0.45 V vs. the RHE in a 0.25 M $NaHCO_3$ solution.

3.4.2. Oxygen Reduction Reaction

The oxygen reduction reaction (ORR) is an electrochemical process in which molecular oxygen is reduced by gaining electrons. It typically occurs at the cathode of fuel cells or metal–air batteries. The reaction pathway can proceed via either a direct four-electron reduction to water (Equation (5)) or a two-step process involving intermediate peroxide formation (Equations (6) and (7)) [205].

$$O_{2\,(g)} + 4H^{+}{}_{(aq)} + 4e^{-} \rightarrow 2H_2O \quad E^{\circ} = +1.23\ \text{V vs. RHE} \tag{5}$$

$$O_{2\,(g)} + 2H^{+}{}_{(aq)} + 2\,e^{-} \rightarrow H_2O_{2\,(g)} \quad E^{\circ} = +0.70\ \text{V vs. RHE} \tag{6}$$

$$H_2O_{2\,(g)} + 2H^{+}{}_{(aq)} + 2e^{-} \rightarrow 2H_2O_{(l)} \quad E^{\circ} = +1.76\ \text{V vs. RHE} \tag{7}$$

BCN catalysts have garnered significant research interest as they meet the requirements for efficient catalysts in the ORR. These compounds feature active sites that promote the adsorption and activation of oxygen species, enabling high electrocatalytic performance while enhancing efficiency and stability [206]. Another notable characteristic of BCN catalysts is their excellent electronic conductivity, facilitating charge transfer during the ORR process. Their unique combination of properties, including high selectivity and tunability through optimized synthesis methods, positions them as a promising and scalable alternative for energy storage devices.

Moses et al. reported the synthesis of BCN nanosheets with varying carbon content, derived from urea and boric acid, as metal-free electrocatalysts for the ORR in alkaline media [207]. These nanosheets followed the 4 e^- pathway (Equation (5)) and exhibited an E_{onset} of +0.198 V vs. the Normal Hydrogen Electrode (NHE). The catalyst performance strongly correlated with the carbon content, with higher carbon-containing samples showing superior activity. Compared to BN-doped graphene, the enhanced kinetics were attributed to the increased number of active sites and the nanosheets' high SSA (2000 $m^2\ g^{-1}$). Marbaniang et al. synthesized a BCN with a rice-grain morphology using boric acid and hexamethylenetetramine ($C_6H_{12}N_4$) as precursors [110]. This BCN demonstrated catalytic activity for the ORR in alkaline conditions with an E_{onset} of +0.83 V vs. the RHE and a current density of 4.6 mA cm^{-2}. The catalysts maintained high stability, enduring up to

10,000 cycles. In a follow-up study, the same group synthesized BCN materials, which presented homopolar B–B bonds within the structure, using the same precursors [13]. These bonds, detected by Raman spectroscopy and XPS, represent an electron-deficient bonding type, which likely lowers the activation overpotential for the ORR. The resulting BCN exhibited an E_{onset} of +1.01 V vs. the RHE and a current density of 5 mA cm^{-2}, following the mechanism outlined in Equation (5). To our knowledge, this is the only study reporting such type of bond in BCNs.

Liu et al. explored BCN materials as supports for metallic nanoparticles due to their high corrosion resistance, which prevents support degradation and nanoparticle aggregation [208]. Pt nanoparticles supported on BCN showed superior half-wave potential (0.927 V) compared to Pt/XC-72R (0.857 V) and retained better durability after 10,000 cycles, with mass activity decreasing by 67% versus 75%, respectively. After 50,000 cycles, the decrease in mass activity was 54%. These experimental results suggested a strong interaction between the Pt nanoparticles and the BNC support that were confirmed by DFT calculations, which showed high binding energies between them. Wang et al. synthesized BCN nanosheets from a mixture of polyvinyl alcohol, guanidine carbonate, and boric acid with an SSA of 817 m^2 g^{-1} and compared them to Pt/C catalysts [206]. The BCN nanosheets exhibited promising ORR performance in acidic and alkaline media, with an E_{onset} of 0.94 V (BCN) versus 0.95 V (Pt/C) and a half-wave potential of 0.82 V versus 0.84 V, respectively. It followed the four-electron pathway (Equations (6) and (7)) and minimal H_2O_2 generation (6%), attributed to the high concentration of pyridinic N sites in the BCN structure that enhance O_2 adsorption and catalytic activity.

Some heterostructures made from carbon–boron nitride have been reported, displaying promising electrochemical performances for the ORR. Patil et al. obtained a carbon nanotube/h-BN composite tested as an electrocatalyst for this reaction [209]. The material showed an improved ORR activity and better stability compared to Pt/C catalysts. This enhancement in the properties was attributed to a higher density of active sites for O_2 adsorption (at the interface between carbon nanotubes and h-BN) This composite exhibited an E_{onset} of +0.86 V vs. the RHE and a current density of 5.78 mA cm^{-2} in alkaline conditions. Weber et al. improved carbon paper by incorporating BN and supporting Pd nanoparticles (CP-BN-Pd) via atomic layer deposition [210]. The catalyst exhibited excellent stability, with only 1% electrochemical surface area degradation after 1000 cycles, compared to 44% for Pd/C. It also achieved an E_{onset} of near 1 V vs. the RHE, a current density of 3 mA cm^{-2}, and an electrochemical surface area of 90 m^2 g^{-1}, four times higher than that of Pd/C. In addition, CP-BN-Pd also demonstrated favorable activity for ethanol and ethylene oxidation. Gu et al. synthesized glycine-functionalized h-BN nanosheets via ball milling [211].

The functionalization was successful, as the sample presented B–C bonds, confirmed by XPS. The electrochemical characterization revealed hydrogen adsorption/desorption on the surface of the material and that the sample followed the four-electron ORR mechanism, displaying high catalytic activity. After 200 cycles, the catalyst retained 95.8% activity, demonstrating excellent durability. Theoretical modeling confirmed that glycine functionalization increases the active site density and adsorption capabilities of h-BN, enhancing ORR efficiency. Xu et al. developed a porous heterostructure combining carbon and h-BN as an electrocatalyst for the ORR [212]. The material exhibited a high selectivity of 90–97% in a potential range of 0.3–0.6 V vs. the RHE. Nazer et al. observed that B- and N-doped reduced graphene oxide followed the 4 e^- mechanism (Equation (5)), while single B-doped or N-doped reduced graphene oxide followed the 2 e^- mechanism [213]. This was explained by the binding of O_2 molecules on the active sites induced by the incorporation of B and N atoms in the reduced graphene oxide structure. Wu et al. created 3D graphene

coupled with boron nitride quantum dots (BNQDs), achieving an E_{onset} of +0.96 V and outperforming traditional graphene–BN composites [214].

The synergistic effect of BNQDs and graphene improved the charge transfer and stability, with the catalyst maintaining stable current density under stress tests. Yu et al. developed Ag-BN/C, a hybrid of carbon nanotubes, h-BN sheets, and Ag nanoparticles, which achieved an ORR activity comparable to Pt/C and demonstrated high methanol tolerance and stability in alkaline media [215]. The catalyst exhibited an E_{onset} of +0.94 V vs. the RHE, with low overpotential and a durability exceeding 20,000 cycles, comparable to commercial RuO_2.

3.4.3. Hydrogen Evolution Reaction

The HER is an electrochemical process where H_2 is produced through the reduction of protons or water molecules, depending on the medium. It occurs at the cathode of an electrochemical cell and is a fundamental half-reaction in water splitting, as well as in various energy conversion and storage technologies like fuel cells and electrolyzers. The HER typically occurs through a series of steps [216,217]. The initial step (Volmer step) is then followed by another step that can proceed via two distinct pathways: the Heyrovsky step or the Tafel step. The specific pathway depends on the catalyst and reaction conditions.

In acidic media:

$$H^+ + e^- \rightarrow H_{ads} \quad \text{(Volmer step)} \tag{8}$$

$$H_{ads} + H^+ + e^- \rightarrow H_2 \quad \text{(Heyrovsky step)} \tag{9}$$

$$2H_{ads} \rightarrow H_2 \quad \text{(Tafel step)} \tag{10}$$

In alkaline media:

$$H_2O + e^- \rightarrow H_{ads} + OH^- \quad \text{(Volmer step)} \tag{11}$$

$$H_{ads} + H_2O + e^- \rightarrow H_2 + OH^- \quad \text{(Heyrovsky step)} \tag{12}$$

$$2H_{ads} \rightarrow H_2 \quad \text{(Tafel step)} \tag{13}$$

In acidic media, H^+ from the solution adsorbs onto the catalyst surface, combining with an electron from the electrode (Volmer step (Equation (8))), followed by H_2 generation either through the reaction of an adsorbed H atom with a proton from the solution (Equation (9)) or by the combination of two adsorbed hydrogen atoms (Tafel step (Equation (10))). In alkaline media, the Volmer step (Equation (11)) initiates the process by splitting a water molecule and adsorbing hydrogen onto the electrode/catalyst surface. Subsequent hydrogen production occurs through either an electrochemical (Heyrovsky step (Equation (12))) or chemical (Tafel step (Equation (3))) pathway. The electron density distribution in BCN catalysts, arising from the synergy of the B, C, and N atoms within the network, facilitates electron exchange and, thus, achieves HER efficiencies comparable to those of Pt- or other noble metal-based systems.

Chhetri et al. reported the synthesis of a BCN from boric acid, urea, and activated charcoal that exhibited a good catalytic performance for the HER [218]. The BCN catalyst showed an E_{onset} of –0.28 V, similar to that of Pt (–0.23 V), and an overpotential of –0.32 V, producing a current density of 20 mA cm^{-2}. The good catalytic performance was attributed to the high proportion of pyridinic nitrogen, the high content of B–C bonds, and the low presence of B–N bonds in the sample. Kaur et al. identified B–C bonds, N–C bonds, and graphene-like behavior as the factors that enhanced the electrocatalytic properties of a BCN material obtained from ammonia, acetone, and boric acid precursors [219]. Liu et al. used

a pyridine borane complex as a precursor of a BCN that was used to decorate graphene capsules to be used as an electrocatalyst for the HER [220].

The BCN catalyst achieved an overpotential of 333 mV at 10 mA cm^{-2}, and it presented a Tafel slope of 39 mV dec^{-1}, outperforming the non-supported BCN (42 mV dec^{-1}) and pristine graphene capsules (142 mV dec^{-1}). Kumar et al. synthesized a composite made of g-C_3N_4, BN, and chitosan that displayed a good stability over 20 h, with an HER overpotential of −0.52 V and a Tafel slope of 150 mV dec^{-1} [221]. This improvement was attributed to the formation of new C–N–B bonds within the composite. Yang et al. designed a hybrid porous material made of single-layer g-C_3N_4 supported on boron-doped graphene [222]. This structure presented defect sites that are ideal for proton adsorption and desorption. The system showed an overpotential of 260 mV at 10 mA cm^{-2}, suggesting that the Volmer–Heyrosky pathway governs its catalytic mechanism, optimizing both efficiency and stability. Similarly, Qu et al. synthesized boron-doped g-C_3N_4 nanosheets with a high boron and nitrogen content [223].

The coexistence of B and N atoms in the structure improved electronic conductivity and helped to maintain the aromaticity of the conjugated planes. The BCN nanosheets followed the Volmer–Heyrovsky mechanism in alkaline media; they presented an E_{onset} of −0.43 V vs. the RHE, an overpotential of 590 mV, and a cathodic current density of 10 mA cm^{-2}.

Metal doping has been investigated as a way to improve the electrocatalytic performance of BCNs. Zhu et al. synthesized a cobalt phosphide-doped BCN catalyst for the HER in alkaline and seawater media [224]. The catalyst achieved an overpotential of 154 mV and 545 mV at 10 mA cm^{-2}, in alkaline and seawater media, respectively, demonstrating good stability and performance under harsh conditions. Salah et al. reported a graphene oxide-modified h-BN catalyst with ruthenium nanoparticles, exhibiting good HER performance with overpotential values of 32 mV in alkaline conditions, without a decline in activity after 50 h [225]. The Ru nanoparticles enhanced active sites for H adsorption, enabling efficient water dissociation and outperforming commercial Pt/C catalysts. Chandrashekharan et al. used a BCN catalyst with palladium nanoparticles (7.72 wt%) for the HER [226]. The material showed an improved overpotential of 481 mV at 10 mA cm^{-2} compared to the pristine BCN. The HER mechanism follows the Volmer–Heyrovsky pathway, with a Tafel slope of 144 mV dec^{-1}. These results were associated with the synergistic effects of the BCN, the high density of active sites, and enhanced electron transfer by the palladium nanoparticles. Other studies have also investigated the coupling of BCNs with MoS_2 to improve their electrocatalytic activity [227–231].

DFT calculations have predicted efficient BCN catalysts for the HER. For instance, a boron-doped C_2N–C_3N structure showed a reduction in the Tafel mechanism barrier from 2.35 to 0.86 V, when compared with pristine C_2N C_3N [232]. The B doping favored the occurrence of the Volmer–Heyrovsky and Volmer–Tafel mechanisms at room temperature. Another example is B-doped C_3N_5, where the introduction of B atoms into the structure decreased the energy barrier for the Volmer–Tafel and Volmer–Heyrovsky mechanisms, and it enhanced the reaction kinetics of the HER in alkaline media [233].

3.4.4. Electrochemical Ammonia Production

NH_3 is a crucial industrial chemical with diverse applications, primarily in agriculture as a key component of fertilizers. Its potential as a hydrogen carrier is gaining significant attention due to its high hydrogen density and ease of storage [4]. Traditionally produced via the energy-intensive Haber–Bosch process [234], emerging electrochemical methods like the nitrogen reduction reaction (NRR; Equation (14)) and the reduction of nitrate

(Equation (15)) in water offer more sustainable production routes, aligning with the global shift towards clean energy solutions [235].

$$N_{2\,(g)} + 6H^{+}{}_{(aq)} + 6e^{-} \rightarrow 2NH_{3\,(aq)} \quad (14)$$

$$NO_3{}^{-}{}_{(aq)} + 6H_2O_{\,(l)} + 8e^{-} \rightarrow NH_{3\,(aq)} + 9OH^{-}{}_{(aq)} \quad (15)$$

BCNs have recently emerged as a promising metal-free electrocatalyst for NH_3 production via the NRR (Equation (14)). BCN nanomeshes on carbon paper, synthesized by Chang et al., demonstrated significant activity in 0.05 M Na_2SO_4 solution using an H-type electrochemical cell [236]. Notably, B-enriched BCNs exhibited superior performance, achieving the highest ammonia formation rate (8.39 μg h^{-1} $cm_{cat}{}^{-2}$; −41.9 μg h^{-1} $mg^{-1}{}_{cat.}$) at −0.6 V and FE (9.87%) at −0.3 V, comparable to state-of-the-art Pt-free HER electrocatalysts. However, the performance declined at potentials beyond −0.6 V and for N-rich BCNs. DFT calculations attributed the positive impact of boron to its ability to promote spontaneous nitrogen adsorption, enhancing the electrocatalytic activity of the BCN. Carbon-doped BN was synthesized by Ma et al. from boric acid and urea, achieving an NH_3 yield of 44.6 μg h^{-1} $mg_{cat}{}^{-1}$, with an FE of 13.27% [237].

DFT calculations revealed that the enhanced performance of the BCN compared to h-BN is attributed to its reduced bandgap, calculated at 1.40 eV, in contrast to 2.08 eV for h-BN. Consistent observations and similar conclusions were reported by Lin et al. and Shi et al. for BCNs produced from other B, N, and C sources [114,238]. For example, Lin et al. used a mixture of $NaBH_4$, $NaNH_2$, and mesoporous carbon to produce a defective BCN by annealing at 580 °C under N_2 [238]. The optimized BCN material achieved an FE of 18.9% and a high NH_3 yield rate of 20.9 μg h^{-1} $mg_{cat}{}^{-1}$ at −0.105 and −0.405 V vs. the RHE, respectively, without producing hydrazine (N_2H_4). Through DFT calculations and XPS, TPD (CO_2 and NH_3), and $^{14}N_2/^{15}N_2$ exchange experiments, the authors proposed a mechanism involving a synergistic effect between electron-deficient B and electron-rich N sites, transitioning from a single "Lewis acid catalysis" to a more efficient "Frustrated Lewis Pairs catalysis" model (Figure 13).

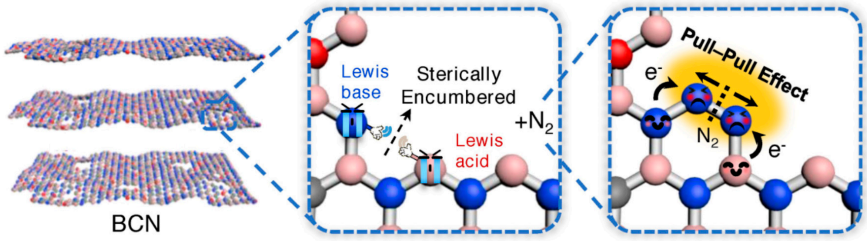

Figure 13. BCN-catalyzed electrochemical nitrogen-to-ammonia conversion: Frustrated Lewis Pairs catalysis enables the adsorption of N_2 molecules into a six-membered ring intermediate; this configuration facilitates the heterolytic cleavage of the N≡N triple bond through a cooperative pull–pull effect. Reprinted with permission from Ref. [238]. Copyright 2022, Wiley. Frustrated Lewis Pairs catalysis enables the adsorption of N_2 molecules into a six-membered ring intermediate; this configuration facilitates the heterolytic cleavage of the N≡N triple bond through a cooperative pull–pull effect [238,239]. Yang et al. further highlighted the crucial role of unsaturated boron sites [240]. By annealing a mixture of g-C_3N_4 and $NaBH_4$, they synthesized a BCN material with up to approximately 25% unsaturated boron sites located at void defects. This material exhibited an impressive NH_3 yield of 29.3 μg h^{-1} $mg_{cat}{}^{-1}$ and an FE of 39% for NH_3 production. Zhang et al. identified the B–C active sites as highly active centers for N_2 reduction to NH_3 [241]. The BCN material was synthesized by mixing melamine and boric acid, followed by freeze-drying and pyrolysis. This BCN achieved an NH_3 yield of 63.02 μg h^{-1} $mg_{cat}{}^{-1}$ and an FE of 32.28% at −0.5 V (RHE) in 0.1 M KOH. The superior catalytic activity was attributed to the higher concentration of B–C bonds in this BCN, compared to other BCN samples with a greater proportion of B–N bonds.

As an alternate electrochemical path, NH_3 can be produced from nitrates, NO_3^-, in water (Equation (15)). This is an elegant approach for removing nitrates from wastewater while regenerating, i.e., producing, NH_3 [242]. The as-produced NH_3 can be used either as a reactant for fertilizers or as a hydrogen/energy carrier, which in both cases allows for the closing of the nitrogen cycle. As for the NRR, BCNs have a role to play in the electrochemical reduction of NO_3^- in the presence of water at an alkaline pH. For example, Hu and co-workers showed that dispersing copper as the electrocatalytically active phase, in a BCN matrix as a support, resulted in high ammonia yields (e.g., 576 μmol h^{-1} mg_{cat}^{-2} at a potential of −0.5 V, with an FE of 88.9%) [243]. The BCN was found to play a dual role: it assists the dispersion of Cu nanoparticles, which has a highly positive effect in terms of the electroactive surface area, and the boron in the BCN contributes to increasing the charge/electron transfer rate of the electrocatalyst. In subsequent works, Hu and co-workers further confirmed the promotional effect of the BCN in support of the electroactive phase such as copper, palladium, and nickel [244–247]. Similar observations were reported by Zhang and co-workers for bimetallic copper–cobalt and the noble metals Pd, Pt, and Ru, as well as by Lu et al. for an Fe electrocatalyst [248–250]. In this last cited work, the Fe-BCN electrocatalyst showed an NH_3 Faradic efficiency of 97.48% and a production rate of NH_3 of 2.17 mg cm^{-2} h^{-1} at a potential of −0.3 V. All of these studies agree on the essential role of boron in the BCN in improving the electrocatalytic performance of the metal dispersed in the BCN matrix.

4. Concluding Remarks and Perspectives

The development of borocarbonitrides, as emerging materials, remains in its early stages. Although numerous studies have been published, there is still a significant gap in the fundamental understanding of BCN properties. A necessary initial step is to establish a clear and consistent definition of what constitutes a BCN. As discussed earlier, the term "borocarbonitride" has been used inconsistently, referring to materials such as boron- and nitrogen-doped carbon, carbon-doped hexagonal boron nitride (h-BN), and boron-doped carbon nitride. In alignment with the proposition of Wan et al. [35], we believe that a standardized classification system is essential. Such a system could rely on elemental analysis to define a minimum ratio of B, C, and N atoms required to classify a material as a "true" BCN rather than a doped structure.

In terms of composition, it is also important to distinguish between the two main types of BCNs reported to date: homogeneous BCNs, where B, C, and N atoms are uniformly mixed, and phase-separated BCNs, which exhibit segregated graphite-like and h-BN domains. A critical question arises: how do these structural differences affect their performance in specific applications? For instance, in electrocatalysis, would a phase-separated structure, leveraging carbon's excellent conductivity, outperform a homogeneous structure? Alternatively, could a well-mixed BCN demonstrate superior catalytic behavior? What is the correlation between the structure and composition of BCNs with their performance in a specific application?

While theoretical studies have predicted various BCN crystal structures under ambient conditions, no pure crystalline phase of a BCN has yet been experimentally synthesized. Addressing this challenge could open new avenues for BCN research.

At this stage of BCN development and technology readiness, estimating fabrication costs remains challenging. However, economic feasibility is a key consideration. The overall cost of BCN production will depend on factors such as the choice of precursors, synthesis method, and energy consumption. Different questions remain unanswered: Is large-scale production economically viable? To enhance affordability, should cost-effective precur-

sors be prioritized for scalable synthesis? These considerations will become increasingly important as the technology readiness level of BCNs advances.

Several key questions also emerge regarding BCN synthesis. In most studies, BCNs are obtained by mixing three precursors, each for one of the elements of the BCN, followed by pyrolysis. However, are these BCNs consistently reproducible? Do different batches of BCNs exhibit uniform properties? Could using a single precursor improve reproducibility? Moreover, what role does residual oxygen play in the structure? Is oxygen incorporation always advantageous, or does it hinder specific properties? Identifying methods to minimize oxygen content where necessary would be valuable. Additionally, specific precursors, such as MOFs or ionic liquids, have been observed to yield unique morphologies. This raises another intriguing question: can tailoring morphology enhance the properties of BCNs for targeted applications? Further improvements will also involve the provision of a toolbox, elaborated through systematic and finer characterizations, which allows the designing of the expected BCN, with, for example, a controlled number of well-identified defects (electron-deficient and/or electron-excess atoms) or a controlled distribution of B–N bonds with the surface.

BCNs have demonstrated promising potential in CO_2 adsorption. Further exploration, including a good understanding of the thermodynamics and mechanisms of surface processes, is needed to fully capitalize on this capability. For example, advanced structures such as membranes could be designed for dynamic operational conditions. This could open prospects for the separation of other gases like hydrogen. Similarly, while theoretical studies have predicted BCNs' capacity for NH_3 adsorption, experimental validation is lacking, representing another area ripe for investigation.

Regarding photocatalytic applications, what is the effect of changing the BCNs' bandgap? Is there an "ideal" bandgap for these materials? As electrocatalysts, BCNs exhibit several desirable properties, including high electrical conductivity, selectivity, a large SSA, and a high density of active sites. These characteristics enhance reaction efficiency by improving charge transport and facilitating the adsorption of oxygen and hydrogen species. BCNs are emerging as viable alternatives to precious metal-based catalysts for reactions such as the ORR and HER. For instance, BCNs synthesized from urea and boric acid have demonstrated performance comparable to platinum, with higher stability, activity, and selectivity and lower cost [207]. Furthermore, BCNs have shown exceptional results as supports for metal nanoparticles, enhancing stability and catalytic performance through strong support–nanoparticle interactions. Despite these advances, the electrochemical mechanisms underlying key reactions, such as the ORR, the HER, CO_2 reduction, and N_2 reduction, remain poorly understood. Future research should prioritize optimizing synthesis methods, elucidating these mechanisms, and addressing scalability challenges. Beyond electrocatalysis, other potential applications of BCNs remain largely unexplored, including their use as selective solar absorbers or high-temperature catalysts (for instance, the reverse water–gas shift reaction). These under-researched areas present exciting opportunities for future studies.

Author Contributions: Conceptualization, C.A.C.-M.; investigation, C.A.C.-M., P.C.M.-G. and U.B.D.; writing—original draft preparation, C.A.C.-M., P.C.M.-G. and U.B.D.; writing—review and editing, C.A.C.-M., P.C.M.-G. and U.B.D.; supervision, C.A.C.-M. All authors have read and agreed to the published version of this manuscript.

Funding: This research received no external funding.

Data Availability Statement: No new data were created or analyzed in this study. Data sharing is not applicable to this article.

Conflicts of Interest: The authors declare no conflicts of interest.

Nomenclature

Ammonia	NH_3
Ammonia borane	AB
Boric acid	$B(OH)_3$
Borocarbonitride(s)	BCN(s)
Boron nitride	BN
Carbon dioxide	CO_2
Chemical vapor deposition	CVD
Density functional theory	DFT
Electron Energy Loss Spectroscopy	EELS
Energy-Dispersive X-ray	EDX
Faraday efficiency(ies)	FE(s)
Graphitic carbon nitride	g-C_3N_4
Hexagonal boron nitride	h-BN
High Resolution	HR
Hydrogen evolution reaction	HER
Hydrogen peroxide	H_2O_2
Hydrogen	H_2
Inductively Coupled Plasma	ICP
Infrared	IR
Isosteric heat of adsorption	$-\Delta H$
Magic-Angle Spinning Nuclear Magnetic Resonance	MAS NMR
Mass Spectrometry	MS
Melamine	$C_3H_6N_6$
Metal-organic framework(s)	MOF(s)
Methane	CH_4
Nitrogen	N_2
Nitrogen reduction reaction	NRR
Normal Hydrogen Electrode	NHE
Optical Emission Spectroscopy	OES
Oxidative dehydrogenation	ODH
Oxidative desulfurization	ODS
Oxygen evolution reaction	OER
Oxygen reduction reaction	ORR
Physical vapor deposition	PVD
Reversible Hydrogen Electrode	RHE
Scanning Electron Microscopy	SEM
Selected-Area Electron Diffraction	SAED
Specific surface area	SSA
Temperature-Programmed Desorption	TPD
Thermogravimetric Analysis	TGA
Transmission Electron Microscopy	TEM
Triethanolamine	TEOA
Two-dimensional	2D
Ultraviolet–Visible	UV-Vis
Urea	$(NH_2)_2CO$
Water	H_2O
Wavelength	λ
X-ray Absorption Near-Edge Structure	XANES
X-ray Diffraction	XRD
X-ray Photoelectron Spectroscopy	XPS

References

1. EPA.gov Sources of Greenhouse Gas Emissions. Available online: https://www.epa.gov/ghgemissions/sources-greenhouse-gas-emissions (accessed on 4 November 2024).
2. Holmes, K.J.; Zeitler, E.; Kerxhalli-Kleinfield, M.; DeBoer, R. Scaling Deep Decarbonization Technologies. *Earth's Future* **2021**, *9*, e2021EF002399. [CrossRef]
3. Borup, R.; Krause, T.; Brouwer, J. Hydrogen Is Essential for Industry and Transportation Decarbonization. *Electrochem. Soc. Interface* **2021**, *30*, 79–84. [CrossRef]
4. Kojima, Y.; Yamaguchi, M. Ammonia as a Hydrogen Energy Carrier. *Int. J. Hydrogen Energy* **2022**, *47*, 22832–22839. [CrossRef]
5. Le, T.-H.; Tran, N.; Lee, H.-J. Development of Liquid Organic Hydrogen Carriers for Hydrogen Storage and Transport. *Int. J. Mol. Sci.* **2024**, *25*, 1359. [CrossRef] [PubMed]
6. Zainal, B.S.; Ker, P.J.; Mohamed, H.; Ong, H.C.; Fattah, I.M.R.; Rahman, S.M.A.; Nghiem, L.D.; Mahlia, T.M.I. Recent Advancement and Assessment of Green Hydrogen Production Technologies. *Renew. Sustain. Energy Rev.* **2024**, *189*, 113941. [CrossRef]
7. Alamiery, A. Advancements in Materials for Hydrogen Production: A Review of Cutting-Edge Technologies. *ChemPhysMater* **2023**, *3*, 64–79. [CrossRef]
8. Singh, G.; Lee, J.; Karakoti, A.; Bahadur, R.; Yi, J.; Zhao, D.; AlBahily, K.; Vinu, A. Emerging Trends in Porous Materials for CO_2 Capture and Conversion. *Chem. Soc. Rev.* **2020**, *49*, 4360–4404. [CrossRef] [PubMed]
9. Pan, W.J.; Sun, J.; Ling, H.; Xu, N.; Ying, Z.F.; Wu, J.D. Preparation of Thin Films of Carbon-Based Compounds. *Appl. Surf. Sci.* **2003**, *218*, 298–305. [CrossRef]
10. Eremets, M.I.; Gavriliuk, A.G.; Trojan, I.A.; Dzivenko, D.A.; Boehler, R. Single-Bonded Cubic Form of Nitrogen. *Nat. Mater.* **2004**, *3*, 558–563. [CrossRef]
11. Novoselov, K.S.; Geim, A.K.; Morozov, S.V.; Jiang, D.; Zhang, Y.; Dubonos, S.V.; Grigorieva, I.V.; Firsov, A.A. Electric Field Effect in Atomically Thin Carbon Films. *Science* **2004**, *306*, 666–669. [CrossRef]
12. Roy, S.; Zhang, X.; Puthirath, A.B.; Meiyazhagan, A.; Bhattacharyya, S.; Rahman, M.M.; Babu, G.; Susarla, S.; Saju, S.K.; Tran, M.K.; et al. Structure, Properties and Applications of Two-dimensional Hexagonal Boron Nitride. *Adv. Mater.* **2021**, *33*, 2101589. [CrossRef] [PubMed]
13. Marbaniang, P.; Ingavale, S.; Catherin, D.; Ramgir, N.; Swami, A.; Kakade, B. Forming a B–B Bond in Boron Carbon Nitride Composite: A Way for Metal Free Electrocatalyst for Oxygen Reduction Reaction in Alkaline Medium. *J. Catal.* **2019**, *378*, 104–112. [CrossRef]
14. Wang, J.; Ma, F.; Liang, W.; Wang, R.; Sun, M. Optical, Photonic and Optoelectronic Properties of Graphene, h-BN and Their Hybrid Materials. *Nanophotonics* **2017**, *6*, 943–976. [CrossRef]
15. Lu, Y.; Yu, Y.; Zhu, X.; Wang, M. Two Predicted Two-Dimensional BCN Structures: A First-Principles Study. *Phys. E Low-Dimens. Syst. Nanostruct.* **2021**, *125*, 114413. [CrossRef]
16. Yuge, K. Prediction of Superhard Cubic Boron–Carbon Nitride through First Principles. *J. Phys. Condens. Matter* **2009**, *21*, 415403. [CrossRef]
17. Qu, N.-R.; Wang, H.-C.; Li, Q.; Li, Y.-D.; Li, Z.-P.; Gou, H.-Y.; Gao, F.-M. Surperhard Monoclinic BC_6N Allotropes: First-Principles Investigations*. *Chin. Phys. B* **2019**, *28*, 096201. [CrossRef]
18. Wang, H.; Li, Z.; Gou, H.; Gao, F. Superhard Orthorhombic BCN Allotropes: O*I*M12-BCN and o*P*M12-BCN. *Diam. Relat. Mater.* **2023**, *132*, 109689. [CrossRef]
19. Zhang, X.; Wang, Y.; Lv, J.; Zhu, C.; Li, Q.; Zhang, M.; Li, Q.; Ma, Y. First-Principles Structural Design of Superhard Materials. *J. Chem. Phys.* **2013**, *138*, 114101. [CrossRef]
20. Wang, H.; Qu, N.; Li, Q.; Li, Y.; Li, Z.; Gou, H.; Gao, F. First-Principles Calculations on Two Superhard BCN Allotropes: *P*3m1-BCN and $I4_1$Md-BCN. *Comput. Mater. Sci.* **2020**, *184*, 109869. [CrossRef]
21. Nakano, S.; Akaishi, M.; Sasaki, T.; Yamaoka, S. Segregative Crystallization of Several Diamond-like Phases from the Graphitic BC_2N without an Additive at 7.7 Gpa. *Chem. Mater.* **1994**, *6*, 2246–2251. [CrossRef]
22. Liu, F.; Zhao, X.; Shi, P.; Li, L.; Dong, Q.; Tian, M.; Wu, Y.; Sun, X. A Review on Recent Progress Achieved in Boron Carbon Nitride Nanomaterials for Supercapacitor Applications. *Batteries* **2023**, *9*, 396. [CrossRef]
23. Radhakrishnan, S.; Patra, A.; Manasa, G.; Belgami, M.A.; Mun Jeong, S.; Rout, C.S. Borocarbonitride-based Emerging Materials for Supercapacitor Applications: Recent Advances, Challenges, and Future Perspectives. *Adv. Sci.* **2024**, *11*, 2305325. [CrossRef]
24. Thomas, S.A.; Cherusseri, J.; Pallavolu, M.R.; Rajendran, D.N.; Kumar, D. Boron Carbon Nitride (BCN): An Emerging Two-Dimensional Material for Rechargeable Batteries. *Energy Fuels* **2024**, *38*, 13704–13721. [CrossRef]
25. Sohrabi, H.; Arbabzadeh, O.; Falaki, M.; Vatanpour, V.; Majidi, M.R.; Kudaibergenov, N.; Joo, S.W.; Khataee, A. Advances in Fabrication, Physio-Chemical Properties, and Sensing Applications of Non-Metal Boron Nitride and Boron Carbon Nitride-Based Nanomaterials. *Surf. Interfaces* **2023**, *41*, 103152. [CrossRef]
26. Aghaei, S.M.; Aasi, A.; Farhangdoust, S.; Panchapakesan, B. Graphene-like BC_6N Nanosheets Are Potential Candidates for Detection of Volatile Organic Compounds (VOCs) in Human Breath: A DFT Study. *Appl. Surf. Sci.* **2021**, *536*, 147756. [CrossRef]

27. Ahmed, M.T.; Islam, S.; Ahmed, F. Density Functional Theory Study of Mobius Boron-Carbon-Nitride as Potential CH_4, H_2S, NH_3, $COCl_2$ and CH_3OH Gas Sensor. *R. Soc. Open Sci.* **2022**, *9*, 220778. [CrossRef]
28. Dindorkar, S.S.; Sinha, N.; Yadav, A. Comparative Study on Adsorption of Volatile Organic Compounds on Graphene, Boron Nitride and Boron Carbon Nitride Nanosheets. *Solid State Commun.* **2023**, *359*, 115021. [CrossRef]
29. Rocky, M.H.; Khatun, M.; Al Roman, A.; Roy, D.; Ahmed, M.T. A DFT Study on Boron Carbon Nitride and In-Plane Graphene-Boron Nitride Nanosheets for O_3 and F_2 Gas Sensing. *Comput. Theor. Chem.* **2024**, *1237*, 114639. [CrossRef]
30. Yadav, A.; Yadav, R.; Sinha, N. A Comparative Study of NH_3 and H_2S Sensing Performance on Monolayer Nanosheets through First-Principle Studies. *Colloids Surfaces A Physicochem. Eng. Asp.* **2024**, *693*, 133997. [CrossRef]
31. Chalase, P.; Deshpande, S.; Kumavat, S.; Deshpande, M. Adsorption Mechanism of Different Toxic Gases onto Pristine BNC_2 and Al-Doped BNC_2 Monolayers. *Phys. Chem. Chem. Phys.* **2023**, *25*, 17337–17351. [CrossRef] [PubMed]
32. Bahadur, R.; Singh, G.; Bando, Y.; Vinu, A. Advanced Porous Borocarbonitride Nanoarchitectonics: Their Structural Designs and Applications. *Carbon* **2022**, *190*, 142–169. [CrossRef]
33. Rao, C.N.R.; Chhetri, M. Borocarbonitrides as Metal-free Catalysts for the Hydrogen Evolution Reaction. *Adv. Mater.* **2019**, *31*, 1803668. [CrossRef] [PubMed]
34. Garg, H.; Patial, S.; Raizada, P.; Nguyen, V.-H.; Kim, S.Y.; Van Le, Q.; Ahamad, T.; Alshehri, S.M.; Hussain, C.M.; Nguyen, T.T.H.; et al. Hexagonal-Borocarbonitride (h-BCN) Based Heterostructure Photocatalyst for Energy and Environmental Applications: A Review. *Chemosphere* **2023**, *313*, 137610. [CrossRef]
35. Wan, Y.; Fang, C.; Yang, X.; Liu, J.; Lin, Y. Borocarbonitride Materials as Metal-Free Catalysts for Advanced Catalysis. *J. Mater. Chem. A* **2024**, *12*, 33392–33426. [CrossRef]
36. Thomas, S.; Asle Zaeem, M. A New Planar BCN Lateral Heterostructure with Outstanding Strength and Defect-Mediated Superior Semiconducting to Metallic Properties. *Phys. Chem. Chem. Phys.* **2020**, *22*, 22066–22077. [CrossRef]
37. Tazekritt, S.; Gallouze, M.; Kellou, A. DFT Study of Energetics and Optoelectronics Properties of B, C, and N Binary and Ternary Honeycomb Structures. *J. Appl. Phys.* **2024**, *135*, 094302. [CrossRef]
38. Wan, J.; Wang, H.; Shu, H. Electro-Optical Properties of a Strain-Induced Borocarbonitride Monolayer from Many-Body Perturbation Theory. *J. Mater. Chem. C* **2024**, *12*, 14642–14649. [CrossRef]
39. Kumawat, M.K.; Yadav, V.; Tiwari, S.; Mahanta, T.; Mohanty, T. Temperature Controlled Synthesis of Boron Carbon Nitride Nanosheets and Study of Their Bandgap Modulation and Nonlinear Optical Properties. *Carbon* **2023**, *214*, 118363. [CrossRef]
40. Zhang, T.; Wang, Y.; Li, X.; Zhuang, Q.; Zhang, Z.; Zhou, H.; Ding, Q.; Wang, Y.; Dang, Y.; Duan, L.; et al. Charge State Modulation on Boron Site by Carbon and Nitrogen Localized Bonding Microenvironment for Two-Electron Electrocatalytic H_2O_2 Production. *Chinese Chem. Lett.* **2023**, *34*, 107596. [CrossRef]
41. Chen, F.; Lv, X.; Wang, H.; Wen, F.; Qu, L.; Zheng, G.; Han, Q. Weak-Field Electro-Flash Induced Asymmetric Catalytic Sites toward Efficient Solar Hydrogen Peroxide Production. *JACS Au* **2024**, *4*, 1219–1228. [CrossRef]
42. Yang, D.; Li, Y.; Chen, R.; Wang, X.; Li, Z.; Xing, T.; Wei, L.; Xu, S.; Dai, P.; Wu, M. Flower-like Superstructure of Boron Carbon Nitride Nanosheets with Adjustable Band Gaps for Photocatalytic Hydrogen Peroxide Production. *J. Mater. Sci. Technol.* **2024**, *183*, 23–31. [CrossRef]
43. Lu, L.; He, J.; Wu, P.; Wu, Y.; Chao, Y.; Li, H.H.; Tao, D.; Fan, L.; Li, H.H.; Zhu, W. Taming Electronic Properties of Boron Nitride Nanosheets as Metal-Free Catalysts for Aerobic Oxidative Desulfurization of Fuels. *Green Chem.* **2018**, *20*, 4453–4460. [CrossRef]
44. Li, X.; Lin, B.; Li, H.; Yu, Q.; Ge, Y.; Jin, X.; Liu, X.; Zhou, Y.; Xiao, J. Carbon Doped Hexagonal BN as a Highly Efficient Metal-Free Base Catalyst for Knoevenagel Condensation Reaction. *Appl. Catal. B Environ.* **2018**, *239*, 254–259. [CrossRef]
45. Horimoto, T.; Kannari, N.; Sato, K. Boron-Carbon-Nitrogen-Containing Heterogeneous Catalysts for Base-Catalyzed Reaction. *Appl. Surf. Sci.* **2021**, *558*, 149841. [CrossRef]
46. Xu, G.; Zheng, H.; Zhang, X.; Li, W.; Zhou, L.; Qin, L. BCN Materials with Adjustable Active Sites as Heterogeneous Acid–Base Catalysts for Knoevenagel Condensation Reaction. *Mol. Catal.* **2023**, *549*, 113447. [CrossRef]
47. Leng, J.; Ali, M.S.; Al-Lohedan, H.A.; Rout, C.S.; Pramoda, K.; Sharath Kumar, K.S. Frustrated Lewis Pairs in Two-Dimensional Borocarbonitride for the Facile Synthesis of 3-Aminoimidazo[1,2-α]Pyridines Using TMSCN as an Isonitrile Substitute. *New J. Chem.* **2024**, *48*, 5971–5980. [CrossRef]
48. Wang, J.; Hao, J.; Liu, D.; Qin, S.; Chen, C.; Yang, C.; Liu, Y.; Yang, T.; Fan, Y.; Chen, Y.; et al. Flower Stamen-like Porous Boron Carbon Nitride Nanoscrolls for Water Cleaning. *Nanoscale* **2017**, *9*, 9787–9791. [CrossRef]
49. Wang, H.; Tian, L.; Huang, Z.; Liang, F.; Guan, K.; Jia, Q.; Zhang, H.; Zhang, S. Molten Salt Synthesis of Carbon-Doped Boron Nitride Nanosheets with Enhanced Adsorption Performance. *Nanotechnology* **2020**, *31*, 505606. [CrossRef]
50. Wang, Y.; Chen, G.; Weng, H.; Wang, L.; Chen, J.; Cheng, S.; Zhang, P.; Wang, M.; Ge, X.; Chen, H.; et al. Carbon-Doped Boron Nitride Nanosheets with Adjustable Band Structure for Efficient Photocatalytic U(VI) Reduction under Visible Light. *Chem. Eng. J.* **2021**, *410*, 128280. [CrossRef]
51. Yang, C.; Bu, D.; Huang, S. Solvent-Free Synthesis of Highly Porous Boron Carbon Nitride for Effective Water Cleaning. *Ceram. Int.* **2022**, *48*, 27658–27663. [CrossRef]

52. Yadav, A.; Dindorkar, S.S.; Ramisetti, S.B.; Sinha, N. Simultaneous Adsorption of Methylene Blue and Arsenic on Graphene, Boron Nitride and Boron Carbon Nitride Nanosheets: Insights from Molecular Simulations. *J. Water Process Eng.* **2022**, *46*, 102653. [CrossRef]
53. Jokar, Z.; Khademiyan, A.; Fallah, M.-A.; Smida, K.; Sajadi, S.M.; Inc, M. Molecular Dynamics Simulation of Urea Adsorption on Various Nanoparticles in a Spiral Microfluidic System. *Eng. Anal. Bound. Elem.* **2022**, *145*, 271–285. [CrossRef]
54. Recepoglu, Y.K.; Goren, A.Y.; Vatanpour, V.; Yoon, Y.; Khataee, A. Boron Carbon Nitride Nanosheets in Water and Wastewater Treatment: A Critical Review. *Desalination* **2022**, *533*, 115782. [CrossRef]
55. Hao, Q.; Song, Y.; Mo, Z.; Mishra, S.; Pang, J.; Liu, Y.; Lian, J.; Wu, J.; Yuan, S.; Xu, H.; et al. Highly Efficient Adsorption of Oils and Pollutants by Porous Ultrathin Oxygen-Modified BCN Nanosheets. *ACS Sustain. Chem. Eng.* **2019**, *7*, 3234–3242. [CrossRef]
56. Peng, D.; Jiang, W.; Li, F.-F.; Zhang, L.; Liang, R.-P.; Qiu, J.-D. One-Pot Synthesis of Boron Carbon Nitride Nanosheets for Facile and Efficient Heavy Metal Ions Removal. *ACS Sustain. Chem. Eng.* **2018**, *6*, 11685–11694. [CrossRef]
57. Patel, M.R.; Park, T.J.; Kailasa, S.K. Synthesis of Fluorescent Boron Carbon Nitride Nanosheets for the Detection of Cu^{2+} Ions and Epinephrine. *New J. Chem.* **2023**, *47*, 9279–9287. [CrossRef]
58. Chen, T.; Liu, T.; Zhou, L.; Li, M.; Meng, Q.; Yu, K.; Lian, J.; Zhu, W. Ternary Boron Carbon Nitrides Hollow Nanotubes with Tunable P-n Homojunction for Photo-Assisted Uranium Extraction: A Combined Batch, EXAFS and DFT Calculations. *Appl. Catal. B Environ.* **2022**, *318*, 121815. [CrossRef]
59. Hirata, Y.; Takeuchi, R.; Taniguchi, H.; Kawagoe, M.; Iwamoto, Y.; Yoshizato, M.; Akasaka, H.; Ohtake, N. Structural and Mechanical Properties of A-BCN Films Prepared by an Arc-Sputtering Hybrid Process. *Materials* **2021**, *14*, 719. [CrossRef]
60. Chakraborty, H.; Mogurampelly, S.; Yadav, V.K.; Waghmare, U.V.; Klein, M.L. Phonons and Thermal Conducting Properties of Borocarbonitride (BCN) Nanosheets. *Nanoscale* **2018**, *10*, 22148–22154. [CrossRef] [PubMed]
61. Yadav, V.K.; Chakraborty, H.; Klein, M.L.; Waghmare, U.V.; Rao, C.N.R. Defect-Enriched Tunability of Electronic and Charge-Carrier Transport Characteristics of 2D Borocarbonitride (BCN) Monolayers from Ab Initio Calculations. *Nanoscale* **2019**, *11*, 19398–19407. [CrossRef]
62. Bafekry, A.; Stampfl, C. Band-Gap Control of Graphenelike Borocarbonitride $g-BC_6N$ Bilayers by Electrical Gating. *Phys. Rev. B* **2020**, *102*, 195411. [CrossRef]
63. Li, S.; Shi, L.; Zhu, H.; Xia, W. Elastic and Bandgap Modulations of Hexagonal BC_2N from First-principles Calculations. *Phys. Status Solidi* **2019**, *256*, 1900281. [CrossRef]
64. Hussain, K.; Younis, U.; Muhammad, I.; Qie, Y.; Guo, Y.; Li, T.; Xie, H.; Sun, Q. Three-Dimensional Porous Borocarbonitride BC_2N with Negative Poisson's Ratio. *J. Mater. Chem. C* **2020**, *8*, 15771–15777. [CrossRef]
65. Jongwannasiri, C.; Yoshida, S.; Watanabe, S. Tribological Behavior under High Temperature of BCN Films Deposited by Sputtering-PBII Hybrid System. *Surf. Interfaces* **2020**, *18*, 100434. [CrossRef]
66. Yadav, A.; Dindorkar, S.S. Vacancy Defects in Monolayer Boron Carbon Nitride for Enhanced Adsorption of Paraben Compounds from Aqueous Stream: A Quantum Chemical Study. *Surf. Sci.* **2022**, *723*, 122131. [CrossRef]
67. Zhou, Z.; Bello, I.; Lei, M..; Li, K..; Lee, C..; Lee, S. Synthesis and Characterization of Boron Carbon Nitride Films by Radio Frequency Magnetron Sputtering. *Surf. Coatings Technol.* **2000**, *128–129*, 334–340. [CrossRef]
68. Prakash, A.; Sundaram, K.B. Optical and XPS Studies of BCN Thin Films by Co-Sputtering of B_4C and BN Targets. *Appl. Surf. Sci.* **2017**, *396*, 484–491. [CrossRef]
69. Attri, R.; Roychowdhury, S.; Biswas, K.; Rao, C.N.R. Low Thermal Conductivity of 2D Borocarbonitride Nanosheets. *J. Solid State Chem.* **2020**, *282*, 121105. [CrossRef]
70. Bhattacharyya, P.; Sahoo, S.; Seikh, A.H.; Mohammed, S.M.A.K.; Sarkar, A.; Alharthi, N. Synthesis, Characterization and Optical Property Study of BCNO and BCN Related Nanopowder. *Diam. Relat. Mater.* **2019**, *92*, 235–241. [CrossRef]
71. Mirzaee, M.; Rashidi, A.; Zolriasatein, A.; Rezaei Abadchi, M. Solid-State Synthesis and Characterization of Two-Dimensional Hexagonal BCN Nanosheet Using a Free Template Method. *Diam. Relat. Mater.* **2021**, *115*, 108350. [CrossRef]
72. Zhou, M.; Li, S.; Wang, S.; Jiang, Z.; Yang, C.; Guo, F.; Wang, X.; Ho, W.-k. Anchoring $ZnIn_2S_4$ Nanosheets on Ultrathin Boron Carbon Nitride Layers for Improved Photo-Redox Catalysis. *Appl. Surf. Sci.* **2022**, *599*, 153985. [CrossRef]
73. Mou, P.; Zhao, J.; Wang, G.; Shi, S.; Wan, G.; Zhou, M.; Deng, Z.; Teng, S.; Wang, G. BCN Nanosheets Derived from Coconut Shells with Outstanding Microwave Absorption and Thermal Conductive Properties. *Chem. Eng. J.* **2022**, *437*, 135285. [CrossRef]
74. Raghu, M.S.; Parashuram, L.; Kumar, K.Y.; Prasanna, B.P.; Rao, S.; Krishnaiah, P.; Prashanth, K.N.; Kumar, C.B.P.; Alrobei, H. Facile Green Synthesis of Boroncarbonitride Using Orange Peel; Its Application in High-Performance Supercapacitors and Detection of Levodopa in Real Samples. *Mater. Today Commun.* **2020**, *24*, 101033. [CrossRef]
75. Ma, F.; Wang, M.; Shao, Y.; Wang, L.; Wu, Y.; Wang, Z.; Hao, X. 'Thermal Substitution' for Preparing Ternary BCN Nanosheets with Enhanced and Controllable Nonlinear Optical Performance. *J. Mater. Chem. C* **2017**, *5*, 2559–2565. [CrossRef]
76. Barua, M.; Sreedhara, M.B.; Pramoda, K.; Rao, C.N.R. Quantification of Surface Functionalities on Graphene, Boron Nitride and Borocarbonitrides by Fluorescence Labeling. *Chem. Phys. Lett.* **2017**, *683*, 459–466. [CrossRef]

77. Attri, R.; Sreedhara, M.B.; Rao, C.N.R. Compositional Tuning of Electrical and Optical Properties of PLD-Generated Thin Films of 2D Borocarbonitrides $(BN)_{1-x}(C)_x$. *ACS Appl. Electron. Mater.* **2019**, *1*, 569–576. [CrossRef]
78. Guo, F.; Li, S.; Yang, C.; Zhang, J.; Hou, Y.; Wang, X. A Highly Crystallized Hexagonal BCN Photocatalyst with Superior Anticorrosion Properties. *Adv. Opt. Mater.* **2022**, *10*, 2200282. [CrossRef]
79. Giusto, P.; Arazoe, H.; Cruz, D.; Lova, P.; Heil, T.; Aida, T.; Antonietti, M. Boron Carbon Nitride Thin Films: From Disordered to Ordered Conjugated Ternary Materials. *J. Am. Chem. Soc.* **2020**, *142*, 20883–20891. [CrossRef]
80. Zhu, J.; Diao, T.; Wang, W.; Xu, X.; Sun, X.; Carabineiro, S.A.C.; Zhao, Z. Boron Doped Graphitic Carbon Nitride with Acid-Base Duality for Cycloaddition of Carbon Dioxide to Epoxide under Solvent-Free Condition. *Appl. Catal. B Environ.* **2017**, *219*, 92–100. [CrossRef]
81. Wang, X.; Yang, L.; Fu, G.; Chen, Y.; Yang, C.; Sun, J. Experimental and Theoretical Investigation for the Cycloaddition of Carbon Dioxide to Epoxides Catalyzed by Potassium and Boron Co-Doped Carbon Nitride. *J. Colloid Interface Sci.* **2022**, *609*, 523–534. [CrossRef]
82. Yang, C.; Zhao, X.; Yang, T. Boron and Phosphorus Co-Doped Graphitic Carbon Nitride Cooperate with Bu_4NBr as Binary Heterogeneous Catalysts for the Cycloaddition of CO_2 to Epoxides. *Catalysts* **2022**, *12*, 1196. [CrossRef]
83. Giusto, P.; Cruz, D.; Heil, T.; Tarakina, N.; Patrini, M.; Antonietti, M. Chemical Vapor Deposition of Highly Conjugated, Transparent Boron Carbon Nitride Thin Films. *Adv. Sci.* **2021**, *8*, 2101602. [CrossRef] [PubMed]
84. Chen, L.; Zhou, M.; Luo, Z.; Wakeel, M.; Asiri, A.M.; Wang, X. Template-Free Synthesis of Carbon-Doped Boron Nitride Nanosheets for Enhanced Photocatalytic Hydrogen Evolution. *Appl. Catal. B Environ.* **2019**, *241*, 246–255. [CrossRef]
85. Chithaiah, P.; Pramoda, K.; Kulkarni, G.U.; Rao, C.N.R. A Simple Chemical Route to Borocarbonitride Nanotubes. *Eur. J. Inorg. Chem.* **2020**, *2020*, 1230–1232. [CrossRef]
86. Thaweesak, S.; Wang, S.; Lyu, M.; Xiao, M.; Peerakiatkhajohn, P.; Wang, L. Boron-Doped Graphitic Carbon Nitride Nanosheets for Enhanced Visible Light Photocatalytic Water Splitting. *Dalt. Trans.* **2017**, *46*, 10714–10720. [CrossRef]
87. Bahadur, R.; Singh, G.; Li, M.; Chu, D.; Yi, J.; Karakoti, A.; Vinu, A. BCN Nanostructures Conjugated Nanoporous Carbon with Oxygenated Surface and High Specific Surface Area for Enhanced CO_2 Capture and Supercapacitance. *Chem. Eng. J.* **2023**, *460*, 141793. [CrossRef]
88. Kosaka, M.; Urakami, N.; Hashimoto, Y. Formation of Graphitic Carbon Nitride and Boron Carbon Nitride Film on Sapphire Substrate. *Jpn. J. Appl. Phys.* **2018**, *57*, 02CB09. [CrossRef]
89. Alrebh, A.; Meunier, J.-L. Boron Carbon Nitride Nanosheets via Induction Plasma: Insights on Synthesis, Characterization, and Control of Band Gap. *Carbon* **2023**, *215*, 118472. [CrossRef]
90. Sutorius, A.; Weißing, R.; Rindtorff Pèrez, C.; Fischer, T.; Hartl, F.; Basu, N.; Shin, H.S.; Mathur, S. Understanding Vapor Phase Growth of Hexagonal Boron Nitride. *Nanoscale* **2024**, *16*, 15782–15792. [CrossRef]
91. Alrebh, A.; Ruth, D.; Plunkett, M.; Gaburici, L.; Couillard, M.; Lacelle, T.; Kingston, C.T.; Kim, K.S. Boron Nitride Nanotubes Synthesis from Ammonia Borane by an Inductively Coupled Plasma. *Chem. Eng. J.* **2023**, *472*, 144891. [CrossRef]
92. Leardini, F.; Flores, E.; Galvis E, A.R.; Ferrer, I.J.; Ares, J.R.; Sánchez, C.; Molina, P.; van der Meulen, H.P.; Navarro, C.G.; Polin, G.L.; et al. Chemical Vapor Deposition Growth of Boron–Carbon–Nitrogen Layers from Methylamine Borane Thermolysis Products. *Nanotechnology* **2018**, *29*, 025603. [CrossRef] [PubMed]
93. Leardini, F.; Jiménez-Arévalo, N.; Ferrer, I.J.; Ares, J.R.; Molina, P.; Navarro, C.G.; Manzanares, Y.; Granados, D.; Urbanos, F.J.; García-García, F.J.; et al. A Fast Synthesis Route of Boron–Carbon–Nitrogen Ultrathin Layers towards Highly Mixed Ternary B–C–N Phases. *2D Mater.* **2019**, *6*, 035015. [CrossRef]
94. Leardini, F.; Massimi, L.; Flores-Cuevas, E.; Fernández, J.; Ares, J.; Betti, M.; Mariani, C. Synthesis of Ternary Borocarbonitrides by High Temperature Pyrolysis of Ethane 1,2-Diamineborane. *Materials* **2015**, *8*, 5974–5985. [CrossRef] [PubMed]
95. Massimi, L.; Betti, M.G.; Caramazza, S.; Postorino, P.; Mariani, C.; Latini, A.; Leardini, F. In-Vacuum Thermolysis of Ethane 1,2-Diamineborane for the Synthesis of Ternary Borocarbonitrides. *Nanotechnology* **2016**, *27*, 435601. [CrossRef]
96. Mighri, R.; Demirci, U.B.; Alauzun, J.G. Microporous Borocarbonitrides $B_xC_yN_z$: Synthesis, Characterization, and Promises for CO_2 Capture. *Nanomaterials* **2023**, *13*, 734. [CrossRef]
97. Tay, R.Y.; Li, H.; Tsang, S.H.; Zhu, M.; Loeblein, M.; Jing, L.; Leong, F.N.; Teo, E.H.T. Trimethylamine Borane: A New Single-Source Precursor for Monolayer h-BN Single Crystals and h-BCN Thin Films. *Chem. Mater.* **2016**, *28*, 2180–2190. [CrossRef]
98. Galligan, P.R.; Xu, Y.; Tang, T.W.; Liu, H.; Tamtaji, M.; Zhou, Y.; Luo, Z. Aligned Carbon-Doping to Modulate Thermal and Electrical Conductivity of Boron Carbon Nitride Grown from Chemical Vapor Deposition. *Carbon* **2023**, *215*, 118397. [CrossRef]
99. Beniwal, S.; Hooper, J.; Miller, D.P.; Costa, P.S.; Chen, G.; Liu, S.-Y.; Dowben, P.A.; Sykes, E.C.H.; Zurek, E.; Enders, A. Graphene-like Boron–Carbon–Nitrogen Monolayers. *ACS Nano* **2017**, *11*, 2486–2493. [CrossRef]
100. Zeng, X.; Chen, H.; He, X.; Zhang, H.; Fang, W.; Du, X.; Li, W.; Huang, Z.; Zhao, L. In-Situ Synthesis of Non-Phase-Separated Boron Carbon Nitride for Photocatalytic Reduction of CO_2. *Environ. Res.* **2022**, *207*, 112178. [CrossRef]

101. Fellinger, T.P.; Su, D.S.; Engenhorst, M.; Gautam, D.; Schlögl, R.; Antonietti, M. Thermolytic Synthesis of Graphitic Boron Carbon Nitride from an Ionic Liquid Precursor: Mechanism, Structure Analysis and Electronic Properties. *J. Mater. Chem.* **2012**, *22*, 23996–24005. [CrossRef]
102. Su, Q.; Yao, X.; Cheng, W.; Zhang, S. Boron-Doped Melamine-Derived Carbon Nitrides Tailored by Ionic Liquids for Catalytic Conversion of CO_2 into Cyclic Carbonates. *Green Chem.* **2017**, *19*, 2957–2965. [CrossRef]
103. Jayaramulu, K.; Kumar, N.; Hazra, A.; Maji, T.K.; Rao, C.N.R. A Nanoporous Borocarbonitride (BC_4N) with Novel Properties Derived from a Boron-Imidazolate-Based Metal-Organic Framework. *Chem.-A Eur. J.* **2013**, *19*, 6966–6970. [CrossRef] [PubMed]
104. Bhaduri, B. High Temperature Synthesis, Surface Characterization, and Photoluminescence Property of Boron Carbon Nitride. *Mater. Lett.* **2024**, *362*, 136231. [CrossRef]
105. Zhang, M.; Zhou, M.; Luo, Z.; Zhang, J.; Wang, S.; Wang, X. Molten Salt Assisted Assembly Growth of Atomically Thin Boron Carbon Nitride Nanosheets for Photocatalytic H_2 Evolution. *Chem. Commun.* **2020**, *56*, 2558–2561. [CrossRef] [PubMed]
106. Panda, P.; Samanta, R.; Barman, S. Facile Synthesis of Two-Dimensional (2D) Boron Carbonitride and 2D Porous Boron Carbonitride for Excellent Energy Storage and Gas Adsorption Applications. *Energy Fuels* **2023**, *37*, 5540–5555. [CrossRef]
107. Sathish, C.; Kothandam, G.; Selvarajan, P.; Lei, Z.; Lee, J.; Qu, J.; Al-Muhtaseb, A.H.; Yu, X.; Breese, M.B.H.; Zheng, R.; et al. Ordered Mesoporous Boron Carbon Nitrides with Tunable Mesopore Nanoarchitectonics for Energy Storage and CO_2 Adsorption Properties. *Adv. Sci.* **2022**, *9*, 2105603. [CrossRef]
108. Luo, J.; Wang, C.; Liu, J.; Wei, Y.; Chao, Y.; Zou, Y.; Mu, L.; Huang, Y.; Li, H.; Zhu, W. High-performance Adsorptive Desulfurization by Ternary Hybrid Boron Carbon Nitride Aerogel. *AIChE J.* **2021**, *67*, e17280. [CrossRef]
109. Ryan Galligan, P.; Liu, H.; Wang, G.; Tamtaji, M.; Li, Y.; Wing Tang, T.; Zhou, Y.; Luo, Z. Lightweight, Freestanding Hybrids of Graphene and Hexagonal Boron Nitride Foams. *Compos. Part A Appl. Sci. Manuf.* **2024**, *182*, 108176. [CrossRef]
110. Marbaniang, P.; Patil, I.; Lokanathan, M.; Parse, H.; Catherin Sesu, D.; Ingavale, S.; Kakade, B. Nanorice-like Structure of Carbon-Doped Hexagonal Boron Nitride as an Efficient Metal-Free Catalyst for Oxygen Electroreduction. *ACS Sustain. Chem. Eng.* **2018**, *6*, 11115–11122. [CrossRef]
111. Mighri, R.; Turani-I-Belloto, K.; Demirci, U.B.; Alauzun, J.G. Nanostructured Carbon-Doped BN for CO_2 Capture Applications. *Nanomaterials* **2023**, *13*, 2389. [CrossRef]
112. Wang, L.; Wang, C.; Zhang, Z.; Wu, J.; Ding, R.; Lv, B. Thermal Induced BCN Nanosheets Evolution and Its Usage as Metal-Free Catalyst in Ethylbenzene Dehydrogenation. *Appl. Surf. Sci.* **2017**, *422*, 574–581. [CrossRef]
113. Castilla-Martinez, C.A.; Charmette, C.; Cartier, J.; Demirci, U.B. A Boron Nitride-Carbon Composite Derived from Ammonia Borane and ZIF-8 with Promises for the Adsorption of Carbon Dioxide. *New J. Chem.* **2024**, *48*, 8534–8544. [CrossRef]
114. Shi, L.; Bi, S.; Qi, Y.; Ning, G.; Ye, J. Highly Efficient Metal-Free Borocarbonitride Catalysts for Electrochemical Reduction of N_2 to NH_3. *J. Colloid Interface Sci.* **2023**, *641*, 577–584. [CrossRef]
115. Chen, X.; Ma, N.; Liu, X.; Wei, C.; Cui, C.; Cao, B.; Guo, Y.; Wang, L.; Gu, Q.; Chen, X. Facile Synthesis of Unsolvated Alkali Metal Octahydrotriborate Salts MB_3H_8 (M = K, Rb, and Cs), Mechanisms of Formation, and the Crystal Structure of KB_3H_8. *Angew. Chem.* **2019**, *131*, 2746–2750. [CrossRef]
116. Barnakov, C.N.; Khokhlova, G.P.; Malysheva, V.Y.; Popova, A.N.; Ismagilov, Z.R. X-Ray Diffraction Analysis of the Crystal Structures of Different Graphites. *Solid Fuel Chem.* **2015**, *49*, 25–29. [CrossRef]
117. Qiu, T.; Yang, J.-G.; Bai, X.-J.; Wang, Y.-L. The Preparation of Synthetic Graphite Materials with Hierarchical Pores from Lignite by One-Step Impregnation and Their Characterization as Dye Absorbents. *RSC Adv.* **2019**, *9*, 12737–12746. [CrossRef] [PubMed]
118. Zhang, X.; Dai, X.; Xie, Z.; Qi, W. Borocarbonitride Catalyzed Ethylbenzene Oxidative Dehydrogenation: Activity Enhancement via Encapsulation of Mn Clusters inside the Tube. *Small* **2024**, *20*, 2401532. [CrossRef]
119. Wang, G.; Zhang, X.; Yan, Y.; Huang, X.; Xie, Z. New Insight into Structural Transformations of Borocarbonitride in Oxidative Dehydrogenation of Propane. *Appl. Catal. A Gen.* **2021**, *628*, 118402. [CrossRef]
120. Shi, Y.; Hamsen, C.; Jia, X.; Kim, K.K.; Reina, A.; Hofmann, M.; Hsu, A.L.; Zhang, K.; Li, H.; Juang, Z.-Y.; et al. Synthesis of Few-Layer Hexagonal Boron Nitride Thin Film by Chemical Vapor Deposition. *Nano Lett.* **2010**, *10*, 4134–4139. [CrossRef]
121. Wu, J.-B.; Lin, M.-L.; Cong, X.; Liu, H.-N.; Tan, P.-H. Raman Spectroscopy of Graphene-Based Materials and Its Applications in Related Devices. *Chem. Soc. Rev.* **2018**, *47*, 1822–1873. [CrossRef]
122. Huang, C.; Chen, C.; Zhang, M.; Lin, L.; Ye, X.; Lin, S.; Antonietti, M.; Wang, X. Carbon-Doped BN Nanosheets for Metal-Free Photoredox Catalysis. *Nat. Commun.* **2015**, *6*, 7698. [CrossRef] [PubMed]
123. Zhao, L.; Zeng, X.; Wang, D.; Zhang, H.; Du, X.; He, X.; Li, W.; Fang, W.; Huang, Z.; Chen, H. In-Plane Graphene Incorporated Borocarbonitride: Directional Utilization of Disorder Charge via Micro π-Conjugated Heterointerface for Photocatalytic CO_2 Reduction. *Carbon* **2023**, *203*, 847–855. [CrossRef]
124. Wang, H.; Zhao, C.; Liu, L.; Xu, Z.; Wei, J.; Wang, W.; Bai, X.; Wang, E. Towards the Controlled CVD Growth of Graphitic B–C–N Atomic Layer Films: The Key Role of B–C Delivery Molecular Precursor. *Nano Res.* **2016**, *9*, 1221–1235. [CrossRef]
125. Portehault, D.; Giordano, C.; Gervais, C.; Senkovska, I.; Kaskel, S.; Sanchez, C.; Antonietti, M. High-Surface-Area Nanoporous Boron Carbon Nitrides for Hydrogen Storage. *Adv. Funct. Mater.* **2010**, *20*, 1827–1833. [CrossRef]

126. Bai, X.; Zhang, X.; Sun, Y.; Huang, M.; Fan, J.; Xu, S.; Li, H. Low Ruthenium Content Confined on Boron Carbon Nitride as an Efficient and Stable Electrocatalyst for Acidic Oxygen Evolution Reaction. *Angew. Chemie-Int. Ed.* **2023**, *62*, e202308704. [CrossRef]
127. Chen, S.; Li, P.; Xu, S.; Pan, X.; Fu, Q.; Bao, X. Carbon Doping of Hexagonal Boron Nitride Porous Materials toward CO_2 Capture. *J. Mater. Chem. A* **2018**, *6*, 1832–1839. [CrossRef]
128. Lim, W.H.; Hamzah, A.; Ahmadi, M.T.; Ismail, R. Band Gap Engineering of BC_2N for Nanoelectronic Applications. *Superlattices Microstruct.* **2017**, *112*, 328–338. [CrossRef]
129. Chand, H.; Choudhary, P.; Kumar, A.; Kumar, A.; Krishnan, V. Atmospheric Pressure Conversion of Carbon Dioxide to Cyclic Carbonates Using a Metal-Free Lewis Acid-Base Bifunctional Heterogeneous Catalyst. *J. CO2 Util.* **2021**, *51*, 101646. [CrossRef]
130. Zhang, Y.; Wang, Q.; Chen, Q.; Li, X.; Li, Y.; Kang, M.; Li, Q.; Wang, J. A New Boron Modified Carbon Nitride Metal-Free Catalyst for the Cycloaddition of CO_2 and Bisepoxides. *Appl. Catal. A Gen.* **2024**, *675*, 119615. [CrossRef]
131. Lei, G.; Qi, S.; Li, H.; Xue, Y.; Shen, L.; Zheng, X.; Wang, S.; Cao, Y.; Zhan, Y. Carbon-Doped Boron Nitride Nanosheets as an Efficient Metal-Free Catalyst for the Selective Oxidation of H_2S. *Phys. Chem. Chem. Phys.* **2023**, *25*, 32317–32322. [CrossRef]
132. Duan, X.; Song, G.; Song, C.; Lu, G.; Wang, Y.; Sun, J.; Chen, A.; Xie, X. Photoinduced Enhanced CO_2 Capture Performance on Carbon-Doped Boron Nitride Adsorbent. *Sep. Purif. Technol.* **2024**, *339*, 126685. [CrossRef]
133. Mondal, K.; Malode, S.J.; Shetti, N.P.; Alqarni, S.A.; Pandiaraj, S.; Alodhayb, A. Porous Nanostructures for Hydrogen Generation and Storage. *J. Energy Storage* **2024**, *76*, 109719. [CrossRef]
134. Hirscher, M.; Zhang, L.; Oh, H. Nanoporous Adsorbents for Hydrogen Storage. *Appl. Phys. A* **2023**, *129*, 112. [CrossRef]
135. Chen, Z.; Kirlikovali, K.O.; Idrees, K.B.; Wasson, M.C.; Farha, O.K. Porous Materials for Hydrogen Storage. *Chem* **2022**, *8*, 693–716. [CrossRef]
136. Villajos, J.A.; Balderas-Xicohténcatl, R.; Al Shakhs, A.N.; Berenguer-Murcia, Á.; Buckley, C.E.; Cazorla-Amorós, D.; Charalambopoulou, G.; Couturas, F.; Cuevas, F.; Fairen-Jimenez, D.; et al. Establishing ZIF-8 as a Reference Material for Hydrogen Cryoadsorption: An Interlaboratory Study. *ChemPhysChem* **2024**, *25*, e202300794. [CrossRef] [PubMed]
137. Broom, D.P.; Hirscher, M. Irreproducibility in Hydrogen Storage Material Research. *Energy Environ. Sci.* **2016**, *9*, 3368–3380. [CrossRef]
138. Li, Y.; Liu, L.; Yu, H.; Zhao, Y.; Dai, J.; Zhong, Y.; Pan, Z.; Yu, H. Synergy of Developed Micropores and Electronic Structure Defects in Carbon-Doped Boron Nitride for CO_2 Capture. *Sci. Total Environ.* **2022**, *811*, 151384. [CrossRef]
139. Raidongia, K.; Nag, A.; Hembram, K.P.S.S.P.S.S.; Waghmare, U.V.; Datta, R.; Rao, C.N.R.N.R. BCN: A Graphene Analogue with Remarkable Adsorptive Properties. *Chem.-A Eur. J.* **2010**, *16*, 149–157. [CrossRef] [PubMed]
140. Kumar, N.; Subrahmanyam, K.S.; Chaturbedy, P.; Raidongia, K.; Govindaraj, A.; Hembram, K.P.S.S.; Mishra, A.K.; Waghmare, U.V.; Rao, C.N.R. Remarkable Uptake of CO_2 and CH_4 by Graphene-like Borocarbonitrides, $B_xC_yN_Z$. *ChemSusChem* **2011**, *4*, 1662–1670. [CrossRef]
141. Mishra, A.K.; Mishra, S. Tuning of Adsorption Energies of CO_2 and CH_4 in Borocarbonitrides $B_xC_yN_z$: A First-Principles Study. *J. Mol. Graph. Model.* **2019**, *93*, 107446. [CrossRef]
142. Ibarra-Rodríguez, M.; Sánchez, M. Graphitic Carbon Nitride Functionalized with Four Boron Atoms for Adsorption and Separation of CO_2/CH_4: DFT Calculations. *Adsorption* **2020**, *26*, 597–605. [CrossRef]
143. Moghaddam, F.E.; Shayeganfar, F.; Ramazani, A. Boron-Rich Enhanced Ambient CO_2 Capture and Storage of Boron-Carbon-Nitride Hybrid Nanotubes. *J. Mater. Chem. A* **2023**, *11*, 17594–17608. [CrossRef]
144. Wang, J.; Luo, X. Theoretical Investigation of the BCN Monolayer and Their Derivatives for Metal-Free CO_2 Photocatalysis, Capture, and Utilization. *ACS Omega* **2024**, *9*, 3772–3780. [CrossRef]
145. Ali Khan, A.; Ahmad, A.; Al-Swaidan, H.M.; Haider, S.; Saeed Akhtar, M. CO_2 Capture and Separation from $H_2/CH_4/N_2$ Gas Mixtures by a Novel Ternary Pentagonal Monolayer "Penta-BCN": First Principles Investigation. *J. Mol. Liq.* **2022**, *348*, 118474. [CrossRef]
146. Talapaneni, S.N.; Singh, G.; Kim, I.Y.; AlBahily, K.; Al-Muhtaseb, A.H.; Karakoti, A.S.; Tavakkoli, E.; Vinu, A. Nanostructured Carbon Nitrides for CO_2 Capture and Conversion. *Adv. Mater.* **2020**, *32*, 1904635. [CrossRef] [PubMed]
147. Xu, G.; Zhang, H.; Wei, J.; Zhang, H.-X.; Wu, X.; Li, Y.; Li, C.; Zhang, J.; Ye, J. Integrating the G-C_3N_4 Nanosheet with B–H Bonding Decorated Metal–Organic Framework for CO_2 Activation and Photoreduction. *ACS Nano* **2018**, *12*, 5333–5340. [CrossRef]
148. Peng, H.-L.; Zhong, F.-Y.; Zhang, J.-B.; Zhang, J.-Y.; Wu, P.-K.; Huang, K.; Fan, J.-P.; Jiang, L.-L. Graphitic Carbon Nitride Functionalized with Polyethylenimine for Highly Effective Capture of Carbon Dioxide. *Ind. Eng. Chem. Res.* **2018**, *57*, 11031–11038. [CrossRef]
149. Castilla-Martinez, C.A.; Mighri, R.; Charmette, C.; Cartier, J.; Demirci, U.B. Boron Nitride from Ammonia Borane and Alkali Amidoboranes and Its Features for Carbon Dioxide Capture. *Energy Technol.* **2023**, *11*, 2201521. [CrossRef]
150. Yang, C.; Wang, J.; Chen, Y.; Liu, D.; Huang, S.; Lei, W. One-Step Template-Free Synthesis of 3D Functionalized Flower-like Boron Nitride Nanosheets for NH_3 and CO_2 Adsorption. *Nanoscale* **2018**, *10*, 10979–10985. [CrossRef]
151. Gou, J.; Liu, C.; Lin, J.; Yu, C.; Fang, Y.; Liu, Z.; Guo, Z.; Tang, C.; Huang, Y. Densification and Pelletization of Porous Boron Nitride Fibers for Effective CO_2 Adsorption. *Ceram. Int.* **2022**, *48*, 11636–11643. [CrossRef]

152. Ghanbari, T.; Abnisa, F.; Wan Daud, W.M.A. A Review on Production of Metal Organic Frameworks (MOF) for CO_2 Adsorption. *Sci. Total Environ.* **2020**, *707*, 135090. [CrossRef] [PubMed]
153. Mahajan, S.; Lahtinen, M. Recent Progress in Metal-Organic Frameworks (MOFs) for CO_2 Capture at Different Pressures. *J. Environ. Chem. Eng.* **2022**, *10*, 108930. [CrossRef]
154. Pescarmona, P.P. Cyclic Carbonates Synthesised from CO_2: Applications, Challenges and Recent Research Trends. *Curr. Opin. Green Sustain. Chem.* **2021**, *29*, 100457. [CrossRef]
155. Huang, Z.; Li, F.; Chen, B.; Yuan, G. Cycloaddition of CO_2 and Epoxide Catalyzed by Amino- and Hydroxyl-Rich Graphitic Carbon Nitride. *Catal. Sci. Technol.* **2016**, *6*, 2942–2948. [CrossRef]
156. Rajendran, A.; Cui, T.; Fan, H.; Yang, Z.; Feng, J.; Li, W. A Comprehensive Review on Oxidative Desulfurization Catalysts Targeting Clean Energy and Environment. *J. Mater. Chem. A* **2020**, *8*, 2246–2285. [CrossRef]
157. Lin, A.; Bagnato, G. Revolutionising Energy Storage: The Latest Breakthrough in Liquid Organic Hydrogen Carriers. *Int. J. Hydrogen Energy* **2024**, *63*, 315–329. [CrossRef]
158. Wei, Y.; Wu, P.; Luo, J.; Dai, L.; Li, H.H.; Zhang, M.; Chen, L.; Wang, L.; Zhu, W.; Li, H.H. Synthesis of Hierarchical Porous BCN Using Ternary Deep Eutectic Solvent as Precursor and Template for Aerobic Oxidative Desulfurization. *Microporous Mesoporous Mater.* **2020**, *293*, 109788. [CrossRef]
159. Sheng, J.; Yan, B.; Lu, W.-D.; Qiu, B.; Gao, X.-Q.; Wang, D.; Lu, A.-H. Oxidative Dehydrogenation of Light Alkanes to Olefins on Metal-Free Catalysts. *Chem. Soc. Rev.* **2021**, *50*, 1438–1468. [CrossRef]
160. Guo, F.; Yang, P.; Pan, Z.; Cao, X.X.-N.; Xie, Z.; Wang, X. Carbon-doped BN Nanosheets for the Oxidative Dehydrogenation of Ethylbenzene. *Angew. Chem.* **2017**, *129*, 8343–8347. [CrossRef]
161. Zhang, X.; Dai, X.; Wu, K.-H.; Su, B.; Chen, J.; Qi, W.; Xie, Z. A Generalized Approach to Adjust the Catalytic Activity of Borocarbonitride for Alkane Oxidative Dehydrogenation Reactions. *J. Catal.* **2022**, *405*, 105–115. [CrossRef]
162. Wang, G.; Chen, S.; Duan, Q.; Wei, F.; Lin, S.; Xie, Z. Surface Chemistry and Catalytic Reactivity of Borocarbonitride in Oxidative Dehydrogenation of Propane. *Angew. Chemie Int. Ed.* **2023**, *62*, e202307470. [CrossRef]
163. Yang, D.; Liu, D.; Li, Y.; Gan, H.; Xu, P.; Tian, Y.; Li, Z.; Xing, T.; Gu, X.; Li, L.; et al. Photo-Thermal Synergistic Catalytic Oxidative Dehydrogenation of Propane over a Spherical Superstructure of Boron Carbon Nitride Nanosheets. *Appl. Surf. Sci.* **2023**, *639*, 158258. [CrossRef]
164. Zhang, X.; Lu, Y.; Han, Y.; Feng, R.; Xie, Z. Unravelling the Role of Boron Dopant in Borocarbonitirde Catalytic Dehydrogenation Reaction. *J. Energy Chem.* **2023**, *85*, 137–143. [CrossRef]
165. Wang, G.; Hu, A.; Duan, Q.; Cui, L.; Chen, Z.; Huang, Z.; Zhang, X.; Huang, S.; Xie, Z. Hierarchical Boroncarbonitride Nanosheets as Metal-Free Catalysts for Enhanced Oxidative Dehydrogenation of Propane. *Chem. Eng. Sci.* **2024**, *288*, 119848. [CrossRef]
166. Mukherjee, D.; Park, S.-E.; Reddy, B.M. CO_2 as a Soft Oxidant for Oxidative Dehydrogenation Reaction: An Eco Benign Process for Industry. *J. CO2 Util.* **2016**, *16*, 301–312. [CrossRef]
167. Zhang, X.; Yan, P.; Xu, J.; Li, F.; Herold, F.; Etzold, B.J.M.; Wang, P.; Su, D.S.; Lin, S.; Qi, W.; et al. Methanol Conversion on Borocarbonitride Catalysts: Identification and Quantification of Active Sites. *Sci. Adv.* **2020**, *6*, eaba5778. [CrossRef]
168. Villa, K.; Galán-Mascarós, J.R.; López, N.; Palomares, E. Photocatalytic Water Splitting: Advantages and Challenges. *Sustain. Energy Fuels* **2021**, *5*, 4560–4569. [CrossRef]
169. Nasir, M.S.; Yang, G.; Ayub, I.; Wang, S.; Wang, L.; Wang, X.; Yan, W.; Peng, S.; Ramakarishna, S. Recent Development in Graphitic Carbon Nitride Based Photocatalysis for Hydrogen Generation. *Appl. Catal. B Environ.* **2019**, *257*, 117855. [CrossRef]
170. Li, X.; Zhang, J.; Zhang, S.; Xu, S.; Wu, X.; Chang, J.; He, Z. Hexagonal Boron Nitride Composite Photocatalysts for Hydrogen Production. *J. Alloys Compd.* **2021**, *864*, 158153. [CrossRef]
171. Wan, Q.; Wei, F.; Ma, Z.; Anpo, M.; Lin, S. Novel Porous Boron Nitride Nanosheet with Carbon Doping: Potential Metal-free Photocatalyst for Visible-light-driven Overall Water Splitting. *Adv. Theory Simul.* **2019**, *2*, 1800174. [CrossRef]
172. Zheng, M.; Ghosh, I.; König, B.; Wang, X. Metal-free Semiconductor Photocatalysis for Sp^2 C−H Functionalization with Molecular Oxygen. *ChemCatChem* **2019**, *11*, 703–706. [CrossRef]
173. Shi, J.; Yuan, T.; Zheng, M.; Wang, X. Metal-Free Heterogeneous Semiconductor for Visible-Light Photocatalytic Decarboxylation of Carboxylic Acids. *ACS Catal.* **2021**, *11*, 3040–3047. [CrossRef]
174. Zhou, M.; Chen, Z.; Yang, P.; Wang, S.; Huang, C.; Wang, X. Hydrogen Reduction Treatment of Boron Carbon Nitrides for Photocatalytic Selective Oxidation of Alcohols. *Appl. Catal. B Environ.* **2020**, *276*, 118916. [CrossRef]
175. Zhou, M.; Yang, P.; Wang, S.; Luo, Z.; Huang, C.; Wang, X. Structure-mediated Charge Separation in Boron Carbon Nitride for Enhanced Photocatalytic Oxidation of Alcohol. *ChemSusChem* **2018**, *11*, 3949–3955. [CrossRef] [PubMed]
176. Shi, J.; Yuan, T.; Wang, R.; Zheng, M.; Wang, X. Boron Carbonitride Photocatalysts for Direct Decarboxylation: The Construction of $C(Sp^3)$–N or $C(Sp^3)$–$C(Sp^2)$ Bonds with Visible Light. *Green Chem.* **2021**, *23*, 3945–3949. [CrossRef]
177. Sivaprakash, K.; Induja, M.; Gomathi Priya, P. Facile Synthesis of Metal Free Non-Toxic Boron Carbon Nitride Nanosheets with Strong Photocatalytic Behavior for Degradation of Industrial Dyes. *Mater. Res. Bull.* **2018**, *100*, 313–321. [CrossRef]

178. Wei, B.; Sun, J.; Mei, Q.; An, Z.; Wang, X.; Cao, H.; Han, D.; He, M. Feasibility of Carbon-Doped BN Nanosheets as Photocatalyst for Degradation of 4-Chloroguaiacol and Ecotoxicity Fate during Indirect Photochemical Transformation. *J. Catal.* **2019**, *379*, 10–17. [CrossRef]
179. Ebadi, S.; Ghasemipanah, K.; Alaie, E.; Rashidi, A.; Khataee, A. Using BCN Nanostructure as Anode Electrode for Photoelectrocatalytic Degradation of Organics: A Statistical Approach. *J. Water Supply Res. Technol.* **2021**, *70*, 856–867. [CrossRef]
180. Sivaprakash, K.; Induja, M.; Gomathipriya, P.; Karthikeyan, S.; Umabharathi, S.T. Single-Step Synthesis of Efficient Nanometric Boron Carbon Nitride Semiconductor for Photocatalysis. *Mater. Res. Bull.* **2021**, *134*, 111106. [CrossRef]
181. Shakunthala, R.; Sivaa Vignesh, C.; Viswanathan, R.; Matheswaran, M. Solar Photocatalytic Process Using Biomass-Derived Boron Carbon Nitride (BM-BCN) for the Treatment of Synthetic Textile Effluent. *Catal. Today* **2024**, *432*, 114583. [CrossRef]
182. Wang, B.; Anpo, M.; Lin, J.; Yang, C.; Zhang, Y.; Wang, X. Direct Hydroxylation of Benzene to Phenol on H-BCN Nanosheets in the Presence of $FeCl_3$ and H_2O_2 under Visible Light. *Catal. Today* **2019**, *324*, 73–82. [CrossRef]
183. Jiang, H.; Zang, C.; Cheng, H.; Sun, B.; Gao, X. Photocatalytic Green Synthesis of Benzazoles from Alcohol Oxidation/Toluene Sp^3 C–H Activation over Metal-Free BCN: Effect of Crystallinity and N–B Pair Exposure. *Catal. Sci. Technol.* **2021**, *11*, 7955–7962. [CrossRef]
184. Luo, Z.; Fang, Y.; Zhou, M.; Wang, X. A Borocarbonitride Ceramic Aerogel for Photoredox Catalysis. *Angew. Chemie Int. Ed.* **2019**, *58*, 6033–6037. [CrossRef]
185. Zhou, M.; Wang, S.; Yang, P.; Huang, C.; Wang, X. Boron Carbon Nitride Semiconductors Decorated with CdS Nanoparticles for Photocatalytic Reduction of CO_2. *ACS Catal.* **2018**, *8*, 4928–4936. [CrossRef]
186. Yuan, T.; Wu, Z.; Zhai, S.; Wang, R.; Wu, S.; Cheng, J.; Zheng, M.; Wang, X. Photosynthetic Fixation of CO_2 in Alkenes by Heterogeneous Photoredox Catalysis with Visible Light. *Angew. Chemie-Int. Ed.* **2023**, *62*, e202304861. [CrossRef] [PubMed]
187. Wang, X.; Liang, F.; Gu, H.; Wu, S.; Cao, Y.; Lv, G.; Zhang, H.; Jia, Q.; Zhang, S. In Situ Synthesized α-Fe_2O_3/BCN Heterojunction for Promoting Photocatalytic CO_2 Reduction Performance. *J. Colloid Interface Sci.* **2022**, *621*, 311–320. [CrossRef] [PubMed]
188. Ri, M.; Choe, K.; Kim, K.; Gao, Y.; Tang, Z. C-Doping into h-BN at Low Annealing Temperature by Alkaline Earth Metal Borate for Photoredox Activity. *RSC Adv.* **2018**, *8*, 42109–42115. [CrossRef]
189. Zeng, X.; Bu, X.; Chen, H.; Huang, Z.; Fang, W.; Wang, D.; He, X.; Du, X.; Li, W.; Zhang, H.; et al. Regulation of Charge Transfer Direction and Key Steps via Y Modification of Redox-Active Sites on Borocarbonitride for Photocatalytic CO_2 Reduction. *Compos. Part B Eng.* **2024**, *287*, 111838. [CrossRef]
190. Zeng, X.; Chen, H.; Fang, W.; Huang, Z.; Wang, D.; He, X.; Du, X.; Li, W.; Zhang, H.; Zhao, L. Local Spatial Polarization Induced Efficient Electron Transfer in Fluorinated Borocarbonitride for Boosting CO_2 Photoreduction. *Chem. Eng. J.* **2024**, *488*, 151042. [CrossRef]
191. Ishaq, T.; Yousaf, M.; Bhatti, I.A.; Batool, A.; Asghar, M.A.; Mohsin, M.; Ahmad, M. A Perspective on Possible Amendments in Semiconductors for Enhanced Photocatalytic Hydrogen Generation by Water Splitting. *Int. J. Hydrogen Energy* **2021**, *46*, 39036–39057. [CrossRef]
192. Babu, P.; Mohanty, S.; Naik, B.; Parida, K. Synergistic Effects of Boron and Sulfur Co-Doping into Graphitic Carbon Nitride Framework for Enhanced Photocatalytic Activity in Visible Light Driven Hydrogen Generation. *ACS Appl. Energy Mater.* **2018**, *1*, 5936–5947. [CrossRef]
193. Lin, S.; Huang, H.; Ma, T.; Zhang, Y. Photocatalytic Oxygen Evolution from Water Splitting. *Adv. Sci.* **2021**, *8*, 2002458. [CrossRef]
194. Luo, Z.; Chen, J.; Fang, Y.; Xie, L.; Liu, Q.; Huang, J.; Liu, M. Synthesis of Borocarbonitride Nanosheets from Biomass for Enhanced Charge Separation and Hydrogen Production. *Sci. Rep.* **2024**, *14*, 14443. [CrossRef]
195. Chen, Q.; Gao, G.; Guo, H.; Wang, S.A.; Wang, Q.; Fang, Y.; Hu, X.; Duan, R. Boron-Doped Polymeric Carbon Nitride Co-Modified with Carbon-Ring and Carboxyl for Efficient Photocatalytic Overall Water-Splitting. *Chem. Eng. J.* **2023**, *470*, 144199. [CrossRef]
196. Chen, L.; Wang, X. Bio-Templated Fabrication of Metal-Free Boron Carbonitride Tubes for Visible Light Photocatalysis. *Chem. Commun.* **2017**, *53*, 11988–11991. [CrossRef] [PubMed]
197. Zhao, D.; Dong, C.L.; Wang, B.; Chen, C.; Huang, Y.C.; Diao, Z.; Li, S.; Guo, L.; Shen, S. Synergy of Dopants and Defects in Graphitic Carbon Nitride with Exceptionally Modulated Band Structures for Efficient Photocatalytic Oxygen Evolution. *Adv. Mater.* **2019**, *31*, 1903545. [CrossRef]
198. Zhao, D.; Wang, Y.; Dong, C.L.; Huang, Y.C.; Chen, J.; Xue, F.; Shen, S.; Guo, L. Boron-Doped Nitrogen-Deficient Carbon Nitride-Based Z-Scheme Heterostructures for Photocatalytic Overall Water Splitting. *Nat. Energy* **2021**, *6*, 388–397. [CrossRef]
199. Nehate, S.D.; Saikumar, A.K.; Prakash, A.; Sundaram, K.B. A Review of Boron Carbon Nitride Thin Films and Progress in Nanomaterials. *Mater. Today Adv.* **2020**, *8*, 100106. [CrossRef]
200. Liu, Y.; Zhang, Y.; Cheng, K.; Quan, X.; Fan, X.; Su, Y.; Chen, S.; Zhao, H.; Zhang, Y.; Yu, H.; et al. Selective Electrochemical Reduction of Carbon Dioxide to Ethanol on a Boron- and Nitrogen-Co-Doped Nanodiamond. *Angew. Chemie-Int. Ed.* **2017**, *56*, 15607–15611. [CrossRef]
201. Cheng, C.; Shao, J.; Wei, P.; Song, Y.; Li, H.; Gao, D.; Wang, G. Nitrogen and Boron Co-doped Carbon Spheres for Carbon Dioxide Electroreduction. *ChemNanoMat* **2021**, *7*, 635–640. [CrossRef]

202. Jia, C.; Ren, W.; Chen, X.; Yang, W.; Zhao, C. (N, B) Dual Heteroatom-Doped Hierarchical Porous Carbon Framework for Efficient Electroreduction of Carbon Dioxide. *ACS Sustain. Chem. Eng.* **2020**, *8*, 6003–6010. [CrossRef]
203. Ma, X.; Du, J.; Sun, H.; Ye, F.; Wang, X.; Xu, P.; Hu, C.; Zhang, L.; Liu, D. Boron, Nitrogen Co-Doped Carbon with Abundant Mesopores for Efficient CO_2 Electroreduction. *Appl. Catal. B Environ.* **2021**, *298*, 120543. [CrossRef]
204. Ayyub, M.M.; Rao, C.N.R. Borocarbonitrides as Metal-Free Electrocatalysts for the Electrochemical Reduction of CO_2. *Chem. Mater.* **2022**, *34*, 6626–6635. [CrossRef]
205. Khan, A.F.; Ferrari, A.G.-M.; Hughes, J.P.; Smith, G.C.; Banks, C.E.; Rowley-Neale, S.J. 2D-Hexagonal Boron Nitride Screen-Printed Bulk-Modified Electrochemical Platforms Explored towards Oxygen Reduction Reactions. *Sensors* **2022**, *22*, 3330. [CrossRef] [PubMed]
206. Wang, J.; Hao, J.; Liu, D.; Qin, S.; Portehault, D.; Li, Y.; Chen, Y.; Lei, W. Porous Boron Carbon Nitride Nanosheets as Efficient Metal-Free Catalysts for the Oxygen Reduction Reaction in Both Alkaline and Acidic Solutions. *ACS Energy Lett.* **2017**, *2*, 306–312. [CrossRef]
207. Moses, K.; Kiran, V.; Sampath, S.; Rao, C.N.R. Few-layer Borocarbonitride Nanosheets: Platinum-free Catalyst for the Oxygen Reduction Reaction. *Chem.–An Asian J.* **2014**, *9*, 838–843. [CrossRef]
208. Liu, F.; Gao, D.; Wang, F.; Shen, P.; Liu, Y.; Zhang, S.; Li, Y.; Zhang, J.; Xue, Y.; Tang, C. Boron Carbon Nitride as Efficient Oxygen Reduction Reaction Support. *J. Colloid Interface Sci.* **2024**, *673*, 901–908. [CrossRef]
209. Patil, I.M.; Lokanathan, M.; Ganesan, B.; Swami, A.; Kakade, B. Carbon Nanotube/Boron Nitride Nanocomposite as a Significant Bifunctional Electrocatalyst for Oxygen Reduction and Oxygen Evolution Reactions. *Chem.–A Eur. J.* **2017**, *23*, 676–683. [CrossRef]
210. Weber, M.; Tuleushova, N.; Zgheib, J.; Lamboux, C.; Iatsunskyi, I.; Coy, E.; Flaud, V.; Tingry, S.; Cornu, D.; Miele, P.; et al. Enhanced Electrocatalytic Performance Triggered by Atomically Bridged Boron Nitride between Palladium Nanoparticles and Carbon Fibers in Gas-Diffusion Electrodes. *Appl. Catal. B Environ.* **2019**, *257*, 117917. [CrossRef]
211. Gu, S.; Chandra Mallick, B.; Hsieh, C.-T.; Gandomi, Y.A.; Zhang, R.-S. Hexagonal Boron Nitride Nanosheets as Metal-Free Electrochemical Catalysts for Oxygen Reduction Reactions. *Ceram. Int.* **2022**, *48*, 9506–9517. [CrossRef]
212. Xu, X.; Zhao, Y.; Yuan, Q.; Wu, Y.; He, J.; Fan, M. Porous Heterostructure of H-BN/Carbon as an Efficient Electrocatalyst for Hydrogen Peroxide Generation. *Carbon Lett.* **2024**, *34*, 1629–1637. [CrossRef]
213. Nazer, E.A.A.; Muthukrishnan, A. Synergistic Effect on BCN Nanomaterials for the Oxygen Reduction Reaction—A Kinetic and Mechanistic Analysis to Explore the Active Sites. *Catal. Sci. Technol.* **2020**, *10*, 6659–6668. [CrossRef]
214. Wu, W.; He, Z.; Xiao, Y.; Zhang, X.; Chen, K.; Fan, J.; Li, X.; Zhao, Y.; Qu, L. A Versatile, Heat-Resisting, Electrocatalytic Active Graphene Framework by in-Situ Formation of Boron Nitride Quantum Dots. *Carbon* **2022**, *192*, 123–132. [CrossRef]
215. Yu, J.; Tang, C.; Zhang, W.; Jiang, Z.; Qi, L.; Mu, Y.; Huang, T.; Zhu, X. Embedded Ag Nanoparticles on Boron Nitride by Introduced Carbon Nanotubes to Optimize ORR and OER Performance. *Int. J. Hydrogen Energy* **2024**, *73*, 294–304. [CrossRef]
216. Ďurovič, M.; Hnát, J.; Bouzek, K. Electrocatalysts for the Hydrogen Evolution Reaction in Alkaline and Neutral Media. A Comparative Review. *J. Power Sources* **2021**, *493*, 229708. [CrossRef]
217. Zaman, N.; Noor, T.; Iqbal, N. Recent Advances in the Metal–Organic Framework-Based Electrocatalysts for the Hydrogen Evolution Reaction in Water Splitting: A Review. *RSC Adv.* **2021**, *11*, 21904–21925. [CrossRef]
218. Chhetri, M.; Maitra, S.; Chakraborty, H.; Waghmare, U.V.; Rao, C.N.R. Superior Performance of Borocarbonitrides, $B_xC_yN_z$, as Stable, Low-Cost Metal-Free Electrocatalysts for the Hydrogen Evolution Reaction. *Energy Environ. Sci.* **2016**, *9*, 95–101. [CrossRef]
219. Kaur, M.; Ahmad Mir, R.; Chauhan, I.; Singh, K.; Krishnan, U.; Kumar, M.; Devi, P.; Pandey, O.P.; Kumar, A. Defect States Induced Luminescence and Electrochemical Studies of Boron Carbon Nitride Nanosheets. *Appl. Surf. Sci.* **2021**, *559*, 149982. [CrossRef]
220. Liu, Y.; Ali, R.; Ma, J.; Jiao, W.; Yin, L.; Mu, C.; Jian, X. Graphene-Decorated Boron–Carbon–Nitride-Based Metal-Free Catalysts for an Enhanced Hydrogen Evolution Reaction. *ACS Appl. Energy Mater.* **2021**, *4*, 3861–3868. [CrossRef]
221. Kumar, P.S.; Prakash, P. Metal Free Nanocomposite of Graphitic Carbon Nitride, Boron Nitride and Chitosan for Efficient Evolution of Hydrogen: A Strategic Approach to Achieving Sustainable and Effective Electrocatalysis. *J. Environ. Chem. Eng.* **2023**, *11*, 109045. [CrossRef]
222. Yang, L.; Wang, X.; Wang, J.; Cui, G.; Liu, D. Graphite Carbon Nitride/Boron-Doped Graphene Hybrid for Efficient Hydrogen Generation Reaction. *Nanotechnology* **2018**, *29*, 345705. [CrossRef] [PubMed]
223. Qu, L.; Zhang, Z.; Zhang, H.; Zhang, H.; Dong, S. Transformation from Graphitic C_3N_4 to Nitrogen-Boron-Carbon Ternary Nanosheets as Efficient Metal-Free Bifunctional Electrocatalyst for Oxygen Reduction Reaction and Hydrogen Evolution Reaction. *Appl. Surf. Sci.* **2018**, *448*, 618–627. [CrossRef]
224. Zhu, L.; Zhang, Y.; Wang, B.; Zou, R.; Huang, Y.; Sun, W. Dynamic Analysis of Equivalent Circuit Model Value of CoP/Boron Nitride Doped Carbon for Hydrogen Evolution Reaction. *Electrochim. Acta* **2022**, *406*, 139846. [CrossRef]
225. Salah, A.; Ren, H.-D.; Al-Ansi, N.; Tan, H.; Yu, F.; Yanchun, L.; Thamer, B.M.; Al-Salihy, A.; Zhao, L.; Li, Y. Dispersing Small Ru Nanoparticles into Boron Nitride Remodified by Reduced Graphene Oxide for High-Efficient Electrocatalytic Hydrogen Evolution Reaction. *J. Colloid Interface Sci.* **2023**, *644*, 378–387. [CrossRef] [PubMed]

226. Chandrashekharan, B.; Sampatkumar, H.G.; George, D.; Antony, A.M.; Doddamani, S.V.; Sasidhar, B.S.; Balakrishna, R.G.; Patil, S.A. Palladium Nanoparticle Immobilized on Coconut Coir Extract Coated Boron Carbon Nitride: A Green and Sustainable Nanocatalyst for Cross-Coupling Reactions and HER Studies. *Diam. Relat. Mater.* **2024**, *147*, 111261. [CrossRef]
227. Pramoda, K.; Ayyub, M.M.; Singh, N.K.; Chhetri, M.; Gupta, U.; Soni, A.; Rao, C.N.R. Covalently Bonded MoS_2–Borocarbonitride Nanocomposites Generated by Using Surface Functionalities on the Nanosheets and Their Remarkable HER Activity. *J. Phys. Chem. C* **2018**, *122*, 13376–13384. [CrossRef]
228. Pramoda, K.; Binwal, D.C.; Rao, C.N.R. Nanocomposites of MoS_2 Nanoparticles with Carboxyl-Functionalized Carbon Nanotubes and Borocarbonitrides Nanosheets, and Their Electrocatalytic Hydrogen Evolution Reaction Activity. *Mater. Res. Bull.* **2022**, *149*, 111697. [CrossRef]
229. Pramoda, K.; Servottam, S.; Kaur, M.; Rao, C.N.R. Layered Nanocomposites of Polymer-Functionalized Reduced Graphene Oxide and Borocarbonitride with MoS_2 and $MoSe_2$ and Their Hydrogen Evolution Reaction Activity. *ACS Appl. Nano Mater.* **2020**, *3*, 1792–1799. [CrossRef]
230. Beere, H.K.; Shantharaja; Yatish, K.V.; Aravind, K.; Ghosh, D.; Balakrishna, R.G.; Pramoda, K. Unveiling Favorable Synergy of Tubules-like $NiMoSe_2$ with Defect-Rich Borocarbonitride over Graphene or MXene for Efficient Hydrogen Evolution Reaction Electrocatalysis. *Int. J. Hydrogen Energy* **2024**, *54*, 1582–1592. [CrossRef]
231. Binwal, D.C.; Pramoda, K.; Zak, A.; Kaur, M.; Chithaiah, P.; Rao, C.N.R. Nanocomposites of 1D MoS_2 with Polymer-Functionalized Nanotubes of Carbon and Borocarbonitride, and Their HER Activity. *ACS Appl. Energy Mater.* **2021**, *4*, 2339–2347. [CrossRef]
232. Xu, W.; Chen, C.; Tang, C.; Li, Y.; Xu, L. Design of Boron Doped C_2N-C_3N Coplanar Conjugated Heterostructure for Efficient HER Electrocatalysis. *Sci. Rep.* **2018**, *8*, 5661. [CrossRef]
233. Ng, S.-F.; Chen, X.; Foo, J.J.; Xiong, M.; Ong, W.-J. 2D Carbon Nitrides: Regulating Non-Metal Boron-Doped C_3N_5 for Elucidating the Mechanism of Wide PH Range Photocatalytic Hydrogen Evolution Reaction. *Chin. J. Catal.* **2023**, *47*, 150–160. [CrossRef]
234. Erfani, N.; Baharudin, L.; Watson, M. Recent Advances and Intensifications in Haber-Bosch Ammonia Synthesis Process. *Chem. Eng. Process.-Process Intensif.* **2024**, *204*, 109962. [CrossRef]
235. Soloveichik, G. Electrochemical Synthesis of Ammonia as a Potential Alternative to the Haber–Bosch Process. *Nat. Catal.* **2019**, *2*, 377–380. [CrossRef]
236. Chang, B.; Li, L.; Shi, D.; Jiang, H.; Ai, Z.; Wang, S.; Shao, Y.; Shen, J.; Wu, Y.; Li, Y.; et al. Metal-Free Boron Carbonitride with Tunable Boron Lewis Acid Sites for Enhanced Nitrogen Electroreduction to Ammonia. *Appl. Catal. B Environ.* **2021**, *283*, 119622. [CrossRef]
237. Ma, C.; Zhang, Y.; Yan, S.; Liu, B. Carbon-Doped Boron Nitride Nanosheets: A High-Efficient Electrocatalyst for Ambient Nitrogen Reduction. *Appl. Catal. B Environ.* **2022**, *315*, 121574. [CrossRef]
238. Lin, W.; Chen, H.; Lin, G.; Yao, S.; Zhang, Z.; Qi, J.; Jing, M.; Song, W.; Li, J.; Liu, X.; et al. Creating Frustrated Lewis Pairs in Defective Boron Carbon Nitride for Electrocatalytic Nitrogen Reduction to Ammonia. *Angew. Chemie Int. Ed.* **2022**, *61*, e202207807. [CrossRef] [PubMed]
239. Sun, Y.; Lin, W.; Guo, T.; Wang, J.; Li, B.; Fu, J. Highly Defective Boron Carbon Nitride Nanosheets: A Robust Electro-Catalyst for Efficient Nitrogen Fixation. *Ind. Eng. Chem. Res.* **2023**, *62*, 10391–10398. [CrossRef]
240. Yang, Y.; Wang, Y.; Wang, X.; Chen, S.; Duan, L.; Zhang, W.; Li, W.; Liu, J. Tailoring Electron-Riched Boron Sites in BCN for Nitrogen Fixation via Alternate Mechanism. *Adv. Mater. Interfaces* **2022**, *9*, 2101842. [CrossRef]
241. Zhang, K.; Zhang, R.; Cui, Y.; Shang, J.; Wei, X.; Wang, S.; Jia, S.; Qin, K.; Zhang, H.; Wang, H.; et al. Tuning Electronic Environment of B Sites in Boron Carbonitride Nanoribbon Boosts Catalytic Activity of Reducing N_2 to NH_3. *Fuel* **2024**, *369*, 131750. [CrossRef]
242. Zhang, Z.; Zhang, N.; Zhang, J.; Deng, B.; Cao, Z.; Wang, Z.; Wei, G.; Zhang, Q.; Jia, R.; Xiang, P.; et al. Critical Review in Electrocatalytic Nitrate Reduction to Ammonia towards a Sustainable Nitrogen Utilization. *Chem. Eng. J.* **2024**, *483*, 148952. [CrossRef]
243. Zhao, X.; Hu, G.; Tan, F.; Zhang, S.; Wang, X.; Hu, X.; Kuklin, A.V.; Baryshnikov, G.V.; Ågren, H.; Zhou, X.; et al. Copper Confined in Vesicle-like BCN Cavities Promotes Electrochemical Reduction of Nitrate to Ammonia in Water. *J. Mater. Chem. A* **2021**, *9*, 23675–23686. [CrossRef]
244. Zhao, X.; Jia, X.; He, Y.; Zhang, H.; Zhou, X.; Zhang, H.; Zhang, S.; Dong, Y.; Hu, X.; Kuklin, A.V.; et al. Two-Dimensional BCN Matrix Inlaid with Single-Atom-Cu Driven Electrochemical Nitrate Reduction Reaction to Achieve Sustainable Industrial-Grade Production of Ammonia. *Appl. Mater. Today* **2021**, *25*, 101206. [CrossRef]
245. Zhao, X.; Li, X.; Zhang, H.; Chen, X.; Xu, J.; Yang, J.; Zhang, H.; Hu, G. Atomic-Dispersed Copper Simultaneously Achieve High-Efficiency Removal and High-Value-Added Conversion to Ammonia of Nitrate in Sewage. *J. Hazard. Mater.* **2022**, *424*, 127319. [CrossRef]
246. Li, X.; Zhao, X.; Zhou, Y.; Hu, J.; Zhang, H.; Hu, X.; Hu, G. Pd Nanocrystals Embedded in BC_2N for Efficient Electrochemical Conversion of Nitrate to Ammonia. *Appl. Surf. Sci.* **2022**, *584*, 152556. [CrossRef]

247. Zhao, X.; Zhu, Z.; He, Y.; Zhang, H.; Zhou, X.; Hu, W.; Li, M.; Zhang, S.; Dong, Y.; Hu, X.; et al. Simultaneous Anchoring of Ni Nanoparticles and Single-Atom Ni on BCN Matrix Promotes Efficient Conversion of Nitrate in Water into High-Value-Added Ammonia. *Chem. Eng. J.* **2022**, *433*, 133190. [CrossRef]
248. Wang, J.; Fan, Z.; Zhao, H.; Liu, X.; Zheng, M.; Zhang, L.; Zhou, Y.; Sun, L.; Liu, J.; Zhang, H. High Faraday Efficiency of Cu_1Co_1-BCN Based on a Dodecahydro-*Closo*-Dodecaborate Hybrid for Electrocatalytic Reduction of Nitrate to Ammonia. *J. Mater. Chem. A* **2023**, *11*, 20234–20241. [CrossRef]
249. Wang, Z.; Xia, S.; Deng, X.; Baryshnikov, G.; Kuklin, A.; Ågren, H.; Zhang, H. Platinum Group Nanoparticles Doped BCN Matrix: Efficient Catalysts for the Electrocatalytic Reduction of Nitrate to Ammonia. *J. Colloid Interface Sci.* **2024**, *664*, 84–95. [CrossRef]
250. Lu, X.; Wei, J.; Lin, H.; Li, Y.; Li, Y.Y. Boron Regulated Fe Single-Atom Structures for Electrocatalytic Nitrate Reduction to Ammonia. *ACS Appl. Nano Mater.* **2024**, *7*, 14654–14664. [CrossRef]